CENTRAL RESEARCH LIBRARY
DOCUMENT COLLECTION

OAK RIDGE NATIONAL LABORATORY LIBRARY
3 4456 0024742 7

ORNL-1620
Progress
4

# PHYSICS DIVISION

## SEMIANNUAL PROGRESS REPORT

FOR PERIOD ENDING SEPTEMBER 10, 1953

CENTRAL RESEARCH LIBRARY
DOCUMENT COLLECTION

LIBRARY LOAN COPY

DO NOT TRANSFER TO ANOTHER PERSON

If you wish someone else to see this document, send in name with document and the library will arrange a loan.

OAK RIDGE NATIONAL LABORATORY
OPERATED BY
CARBIDE AND CARBON CHEMICALS COMPANY
A DIVISION OF UNION CARBIDE AND CARBON CORPORATION
UCC
POST OFFICE BOX P
OAK RIDGE, TENNESSEE

ORNL-1620
Copy No. 4

Contract No. W-7405-eng-26

# PHYSICS DIVISION

# SEMIANNUAL PROGRESS REPORT

for Period Ending September 10, 1953

A. H. Snell
E. O. Wollan, Associate Director

DATE ISSUED

DEC 3 1953

OAK RIDGE NATIONAL LABORATORY
Operated by
CARBIDE AND CARBON CHEMICALS COMPANY
A Division of Union Carbide and Carbon Corporation
Post Office Box P
Oak Ridge, Tennessee

OAK RIDGE NATIONAL LABORATORY LIBRARY
3 4456 0024742 7

## INTERNAL DISTRIBUTION

1. C. E. Center
2. Biology Library
3. Health Physics Library
4-5. Central Research Library
6. Reactor Experimental Engineering Library
7-11. Laboratory Records Department
12. Laboratory Records, ORNL R.C.
13. C. E. Larson
14. W. B. Humes (K-25)
15. L. B. Emlet (Y-12)
16. A. M. Weinberg
17. E. H. Taylor
18. E. D. Shipley
19. E. J. Murphy
20. F. C. VonderLage
21. A. H. Snell
22. A. Hollaender
23. J. A. Swartout
24. K. Z. Morgan
25. F. L. Culler
26. M. T. Kelley
27. E. M. King
28. E. O. Wollan
29. D. W. Cardwell
30. A. S. Householder
31. L. D. Roberts
32. R. B. Briggs
33. R. N. Lyon
34. W. C. Koehler
35. W. K. Ergen
36. E. P. Blizard
37. M. E. Rose
38. G. E. Boyd
39. Lewis Nelson
40. R. W. Stoughton
41. C. E. Winters
42. W. H. Jordan
43. E. C. Campbell
44. D. S. Billington
45. M. A. Bredig
46. R. S. Livingston
47. C. P. Keim
48. J. L. Meem
49. C. E. Clifford
50. G. H. Clewett
51. C. D. Susano
52. C. J. Borkowski
53. M. J. Skinner
54. L. A. Rayburn
55. S. Bernstein
56. P. M. Reyling
57. D. D. Cowen
58. W. M. Good
59. G. C. Williams
60. J. L. Fowler
61. R. W. Johnson
62. J. R. McNally, Jr.
63. R. G. Cochran
64. C. L. Storrs
65. P. M. Steir
66. J. H. Neiler
67. E. P. Wigner (consultant)
68. H. A. Bethe (consultant)
69. K. Lark-Horovitz (consultant)
70. Eugene Guth (consultant)
71. J. G. Daunt (consultant)
72. W. M. Breazeale (consultant)
73. E. C. Smith

## EXTERNAL DISTRIBUTION

74. W. G. Pollard, ORINS
75. W. K. H. Panofsky, Stanford University
76. D. B. Benedict, C&CCC, South Charleston
77. L. C. Biedenharn, Sloans Physics Laboratory
78. R. F. Bacher, California Institute of Technology
79-80. Ohio State University, Attn: Professor of Naval Science
81. John Dunning, Columbia University
82. Phillips Petroleum Co., Attn: Librarian
83. R. L. Heath, American Cyanamid Co.
84. S. DeBenedetti, Carnegie Institute of Technology
85. Massachusetts Institute of Technology, Department of Electrical Engineering
86. A. von Hippel, Laboratory for Insulation Research, MIT
87. M. Goodrich, Louisiana State University
88. Truman S. Grey, Massachusetts Institute of Technology
89-346. Given distribution as shown in TID 4500 under Physics Category

Physics Division quarterly progress reports previously issued in this series are as follows:

| | |
|---|---|
| ORNL-325 Supplement | December, January, and February, 1948-1949 |
| ORNL-366 | Period Ending June 15, 1949 |
| ORNL-481 | Period Ending September 25, 1949 |
| ORNL-577 | Period Ending December 15, 1949 |
| ORNL-694 | Period Ending March 15, 1950 |
| ORNL-782 | Period Ending June 15, 1950 |
| ORNL-865 | Period Ending September 20, 1950 |
| ORNL-940 | Period Ending December 20, 1950 |
| ORNL-1005 | Period Ending March 20, 1951 |
| ORNL-1092 | Period Ending June 20, 1951 |
| ORNL-1164 | Period Ending September 20, 1951 |
| ORNL-1278 | Period Ending December 20, 1951 |
| ORNL-1289 | Period Ending March 20, 1952 |
| ORNL-1365 | Period Ending June 20, 1952 |
| ORNL-1415 | Period Ending September 20, 1952 |
| ORNL-1496 | Period Ending December 20, 1952 |

## CONTENTS


PUBLICATIONS . . . . . vii

ANNOUNCEMENTS . . . . . viii

SUMMARY . . . . . 1

1. HIGH-VOLTAGE PHYSICS . . . . . 3
Thresholds and Neutron Yields for $(p,n)$ Reactions in Intermediate Nuclei . . . . . 3
Elastic Scattering Angular Distributions of Fast Neutrons on Light Nuclei . . . . . 5
$Li^7(d,t)Li^6$ Reaction . . . . . 5
Angular Distributions of Alpha Particles from the $Na^{23}(p,\alpha)Ne^{20}$ Reaction . . . . . 7

2. RADIOACTIVITY AND NUCLEAR ISOMERISM . . . . . 10
Angular Correlation of Gamma Rays . . . . . 10
Angular Correlations of Gamma Rays in $Ta^{181}$ . . . . . 10
Internal Conversion Electron-Gamma Directional Angular Correlation of $Bi^{207}$ . . . . . 13
Internal Conversion and Directional Angular Correlation of the $Bi^{207}$ Gamma Rays . . . . . 14
Measurement of the Half Life and Gamma Spectrum of $Pb^{207m}$ by Liquid-Flow Technique . . . . . 14
Fission Gamma-Ray Spectrum . . . . . 15
Broad-Beam Gamma-Ray Attenuations . . . . . 16
Po-Be and Po-B Gamma-Ray Spectra . . . . . 17

3. NEUTRON DIFFRACTION . . . . . 27
Magnetic Scattering Studies of Erbium Metal in the Temperature Range of 300 to 4.2°K . . . . . 27
Magnetic Structure of $Mn_2Sb$ . . . . . 30
Magnetic Disorder Scattering in Iron-Chromium and Cobalt-Chromium Alloys . . . . . 30

4. LOW TEMPERATURES AND NUCLEAR POLARIZATION . . . . . 32
Capture of Polarized Neutrons by Polarized Manganese Nuclei . . . . . 32
Interaction of Polarized Neutrons with Polarized $Sm^{149}$ Nuclei . . . . . 32
Polarization of samarium nuclei . . . . . 32
Detection of polarization . . . . . 32
Measurement and the Calculation of Liquid-Helium Vapor Pressure-Temperature Scale from 1 to 4.2°K . . . . . 33
Susceptibility Studies of the Antiferromagnetism in $MnCl_2$ and $UI_3$ . . . . . 33
Heat Capacity Measurements . . . . . 35
Mutual Inductance Bridge and Cryostat for Low Temperature Magnetic Measurements . . . . . 35
Some Thermodynamic Properties of $Mn(ND_4)_2(SO_4)_2 \cdot 6D_2O$ below 1°K . . . . . 35
Measurement of Operating Temperature in the Collins Helium Liquefier . . . . . 36

5. HEAVY-ION PHYSICS . . . . . 37
Measurement of Electron Capture and Loss Cross Sections . . . . . 37
Electron Multiplier Studies . . . . . 39

6. NEUTRON CROSS SECTIONS . . . . . 42
Stable Isotope Neutron Cross Sections . . . . . 42
Neutron Time-of-Flight Spectrometer . . . . . 42

7. INSTRUMENTATION . . . . . 46
Double-Line Linear Amplifier . . . . . 46
Multichannel Analyzers . . . . . 50
Pulse-handling equipment for the 120-channel analyzer . . . . . 50

Pulse lengthener and window amplifier . . . . . 52
Test-pulse generator . . . . . 52
Double scale of 16 for multichannel analyzer . . . . . 54
Improved scale of 256 . . . . . 54
Subminiature Scaling Units . . . . . 57
Basic unit . . . . . 57
Automatic preset-count scale of 4096 . . . . . 58
Neutron Phosphors . . . . . 62
Total-Absorption Spectrometer . . . . . 62
Operation of Proton Recoil Telescope . . . . . 64

8. PHYSICS OF REACTORS . . . . . 67
Visible Light from Nuclear Radiation . . . . . 67
Measurement of the Energy Released per Fission . . . . . 67

9. THEORETICAL PHYSICS . . . . . 69
Pseudoscalar Interaction in Beta Decay . . . . . 69
Magnetic Scattering of Neutrons . . . . . 69
Theory of Polarized Particles and Gamma Rays in Nuclear Reactions . . . . . 70
Tabulation of Angular Momentum Functions . . . . . 70
Relations Between the Generalized Hypergeometric Series and the Angular Momentum Functions of Physics . . . . . 70
Scattering Matrix Formalism for Nuclear Reactions Involving Gamma Rays . . . . . 71
Calculation of Level Shift in Hydrogen . . . . . 72

## PUBLICATIONS

The following papers from the Physics Division have appeared in open publications this year:

C. G. Shull and M. K. Wilkinson, "Neutron Diffraction Studies of Various Transition Elements," *Revs. Mod. Phys.* **25**, 100 (1953).

W. C. Koehler and E. O. Wollan, "Paramagnetic Scattering of Neutrons by Trivalent Ions of Nd and Er," *Revs. Mod. Phys.* **25**, 128 (1953).

L. D. Roberts, C. C. Sartain and B. Borie "Measurement of the Nuclear and Electronic Contributions to the Specific Heat of Neodymium Ethyl Sulfate Near 1°K," *Revs. Mod. Phys.* **25**, 170 (1953).

J. D. Kington, J. K. Bair, R. R. Carlson, and H. B. Willard, "The Mass Difference $Si^{27}$-$Al^{27}$," *Phys. Rev.* **89**, 530 L (1953).

A. Simon and T. A. Welton, "Production of Polarized Particles in Nuclear Reactions," *Phys. Rev.* **89**, 886 L (1953).

Albert Simon, "Higher Spin Polarizations in Nuclear Reactions," *Phys. Rev.* **90**, 326 L (1953).

M. E. Rose and C. L. Perry, "The Effect of the Finite deBroglie Wave Length in the Theory of Beta-Decay," *Phys. Rev.* **90**, 479 (1953).

C. F. Barnett, P. M. Stier, and G. E. Evans, "Pig Iron Source," *Rev. Sci. Instr.* **24**, 394 L (1953).

J. K. Bair, J. D. Kington, and H. B. Willard, "$N^{14}$ Level Structure from the $C^{13}(p,n)N^{13}$ Reaction," *Phys. Rev.* **90**, 575 (1953).

R. A. Erickson, "Neutron Diffraction Studies of Antiferromagnetism in Manganous Fluoride and and Some Isomorphous Compounds," *Phys. Rev.* **90**, 779 (1953).

G. E. Evans, P. M. Stier, and C. F. Barnett, "The Stopping of Heavy Ions in Gases," *Phys. Rev.* **90**, 825 (1953).

H. B. Willard, J. K. Bair, and J. D. Kington, "The Reactions $T(p,n)He^3$ and $T(p,\gamma)He^4$," *Phys. Rev.* **90**, 865 (1953).

George E. Evans, "Materials for Reactors," *Nucleonics* **11**, No. 6, 18 (1953).

Albert Simon, "Theory of Polarized Particles in Nuclear Reactions," *Phys. Rev.* **90**, 991 L (1953).

A. Simon and T. A. Welton, "Production of Polarized Particles in Nuclear Reactions," *Phys. Rev.* **90**, 1036 (1953).

M. E. Rose, "$O^{14}$ $\beta$-Decay and the Fermi Interaction," *Phys. Rev.* **90**, 1123 L (1953).

M. E. Rose, "Angular Correlation in Allowed $\beta$-Transitions," *Phys. Rev.* **91**, 197 L (1953).

L. C. Biedenharn and M. E. Rose, "Theory of Angular Correlation of Nuclear Reactions," *Revs. Mod. Phys.* **25**, 729 (1953).

W. C. Koehler and E. O. Wollan, "Slow Neutron Scattering Cross Sections for Rare Earth Nuclides," *Phys. Rev.* **91**, 597 (1953).

M. E. Rose, "Analysis of Angular Correlation and Angular Distribution Data," *Phys. Rev.* **91**, 610 (1953).

E. D. Klema and F. K. McGowan, "Gamma-Gamma Angular Correlation in $Ni^{60}$," *Phys. Rev.* **91**, 616 (1953).

R. W. Lamphere, "Fission Cross Section of Uranium-234," *Phys. Rev.* **91**, 655 (1953).

W. E. Kunz, C. D. Moak, and W. M. Good, "Energy Levels in $Be^8$ from the Reaction $Li^6(He^3,p)Be^8$," *Phys. Rev.* **91**, 676 (1953).

## ANNOUNCEMENTS

The following persons have been added to the staff of the Physics Division during this period: V. G. Harness and J. T. Thomas (Critical Experiments); J. E. Faulkner, H. Weaver, and L. S. Abbott (Shielding); N. H. Lazar and J. H. Neiler (Instrumentation); and R. B. Murray (ORINS fellow) and J. E. Sherwood (Slow Neutron Physics).

G. E. Evans (Reactor School and Heavy Ion Physics) is on leave and is working with National Carbon Division of Union Carbide and Carbon Chemicals Corporation.

R. Stephenson (Engineering Division) is on loan to the Instrumentation Group.

Transfers during this period were as follows: W. H. Jordan (Instrumentation) transferred to Research Director's Division; J. L. Meem and J. K. Leslie (Shielding) transferred to the ANP Division; H. L. Reynolds (Neutron Decay) transferred to Electro-Nuclear Research Division; and Francis Green (High Voltage) transferred to Instrumentation and Controls Division.

Terminations: J. F. Ellis, R. C. Keen, and R. A. Francis (Critical Experiments); H. L. F. Enlund and R. K. Honeycutt (Shielding); J. B. Dial (Reactor School).

Summer personnel included the following Research Participants and University students: R. A. Erickson (Assistant Professor of Physics, University of Tennessee), Low Temperature Group; N. S. Gingrich (Professor of Physics, University of Missouri), Neutron Diffraction; V. E. Parker (Chairman, Dept. of Physics, Louisiana State University), High Voltage Physics; R. W. Rusk (Instructor of Physics, Virginia Polytechnic Institute), Heavy Ion Physics; D. S. Falk (student, Cornell University), Neutron Decay; R. Knight (student, University of Tennessee), High Voltage; A. J. Lazarus (student, Massachusetts Institute of Technology), Instrumentation; A. B. Reynolds (student, Massachusetts Institute of Technology), Heavy Ion Physics; and J. E. Russell (student, Yale University), High Voltage Physics.

# 1. HIGH-VOLTAGE PHYSICS

## THRESHOLDS AND NEUTRON YIELDS FOR $(p,n)$ REACTIONS IN INTERMEDIATE NUCLEI

C. H. Johnson C. C. Trail

The thresholds and the relative yields above threshold for the $(p,n)$ reaction have been observed for several intermediate nuclei. Intense (100-$\mu$a) proton currents from the 2.5-Mev Van de Graaff generator were used to bombard the water-cooled targets, which consisted of the target material evaporated on gold or platinum backing. Proton energies were analyzed by a 90-deg bending magnet that was calibrated against the $F^{19}(p,\alpha\gamma)O^{16}$ resonances and the $Li^7(p,n)Be^7$ threshold. Calibrations were made with a deuterium magnetic-moment fluxmeter. Neutrons were detected with three $BF_3$ counters that were encased in paraffin and were placed so as to nearly surround the target.

Figure 1.1 shows the observed thresholds, plotted as neutron counts per millicoulomb of protons vs. proton energy, for the $(p,n)$ reaction on seven nuclei. The background below the threshold on each target was found to be the same as that of a clean gold or platinum blank. Table 1.1 summarizes the results of Fig. 1.1. The data tabulated in the columns from left to right in Fig. 1.1 are (1) the observed $(p,n)$ reaction, (2) the target material, (3) the observed threshold and uncertainty, and (4) the mass difference between the initial and the final nuclei when computed under the assumption that the reaction leads to the ground state. The $Ga^{71}$, $Ge^{73}$, $Ti^{49}$, $Zn^{67}$, and $Zn^{70}$ targets were separated isotopes obtained from the Stable Isotope Research and Production Division. A spectroscopic analysis was made on most of the targets, and, in particular, the observed $Ga^{71}$ threshold cannot be ascribed to a manganese impurity. The observed $Mn^{55}$ threshold is in fair agreement with the value of 1.02 ± 0.01 Mev that was found by McCue and Preston.[1]

An attempt was made to find the thresholds of $Ca^{46}$, $Ca^{48}$, $Ge^{76}$, and $Se^{82}$. Neutrons were detected from $Ca^{48}$ and $Se^{82}$, but no well-defined threshold was found. The upper limits for the thresholds are 0.65 Mev for $Ca^{48}$ and 1.0 Mev for $Se^{82}$. The $Ca^{46}$ and $Ge^{76}$ thresholds were obscured by contaminations of $Ca^{48}$ and $Ge^{73}$, respectively.

In addition to these threshold observations, the relative yield in the region up to 100 kev above threshold has been observed for ten different nuclei. In the interpretation of the yield curves, the tentative assumption was made that the counting efficiency is independent of neutron energy between 1 and 100 kev. A very rough measurement of the counting efficiency, made by using a long counter

[1] J. J. G. McCue and W. M. Preston, *Phys. Rev.* **84**, 1150 (1951).

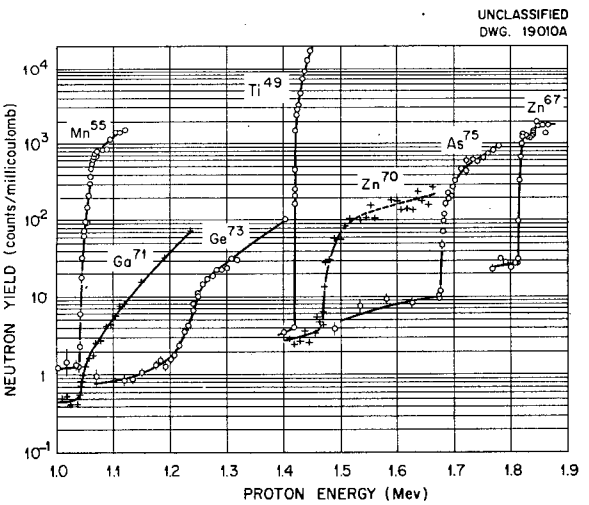


**Fig. 1.1. $(p,n)$ Thresholds for Seven Intermediate Nuclei.**

**TABLE 1.1. $(p,n)$ THRESHOLDS FOR SEVEN INTERMEDIATE NUCLEI**

| REACTION | TARGET | THRESHOLD (kev) | MASS DIFFERENCE (kev) |
|---|---|---|---|
| $Ti^{49}(p,n)V^{49}$ | $TiO_2$ | 1420 ± 5 | 610 |
| $Mn^{55}(p,n)Fe^{55}$ | Mn | 1039 ± 5 | 238 |
| $Zn^{67}(p,n)Ga^{67}$ | ZnO | 1812 ± 5 | 1003 |
| $Zn^{70}(p,n)Ga^{70}$ | ZnO | 1470 ± 5 | 667 |
| $Ga^{71}(p,n)Ge^{71}$ | $Ga_2O_3$ | 1040 ± 10 | 244 |
| $Ge^{73}(p,n)As^{73}$ | $GeO_2$ | 1170 ± 30 | 370 |
| $As^{75}(p,n)Se^{75}$ | As | 1674 ± 5 | 870 |

calibrated with a polonium-beryllium source, gave efficiencies that range from 0.75 to 1.3%. In the following discussion, it is assumed that the counter had a constant efficiency of 1.0%. It is further assumed that, since the counters subtend a large angle at the target, the number of counts is independent of the angular distribution of the neutrons from the source.

Under these assumptions, the experimental yield curves (minus background) were converted to $\int\sigma(E)\,dE$ by use of the known weights and compositions of the various targets. The integral is the energy-dependent reaction cross section integrated from the threshold to the full proton bombarding energy or integrated over the target thickness up to the proton bombarding energy. The targets had a stopping power of 25 kev or more. The resulting yield curves are shown as data points (crosses or circles) in Fig. 1.2.

The solid curves of Fig. 1.2 are determined theoretically from a statistical model of the compound nucleus.[2] It is assumed that, at the excitation energy of the compound nucleus, there are many energy levels of all types. Thus, for a given proton-orbital angular momentum and compound-nucleus total angular momentum, the cross section is the product of the cross section for forming the compound nucleus times the relative probability for the emission of a neutron. The cross section for compound-nucleus formation is proportional to the proton penetration factor,[3] and the relative neutron emission probability depends on the ratio of the neutron and proton barrier factor and also on the gamma-ray emission probability. This latter quantity was estimated from neutron-capture cross section curves by using the same continuum theory as is discussed here.[4] Penetration factors were computed by using a nuclear radius of $1.4 \times 10^{-13}\,A^{1/3}$ cm.

Neutron emission is considered only if allowed by conservation of parity and total angular momentum, and the total reaction cross section is a summation over all the possible transitions that obey these conservation laws. For this description, the parity and total angular momenta of the initial and final ground state nuclei were assigned according to the nuclear-shell model. This assignment is fairly certain for all the odd nuclei of Fig. 1.2, except for the product nucleus in the $As^{75}(p,n)Se^{75}$ reaction. $Se^{75}$ may be either $p_{1/2}$ or $g_{9/2}$. The solid $As^{75}$ curve results for the $p_{1/2}$ assignment, and the lower dotted curve is calculated for the $g_{9/2}$ assumption. The only odd-odd nucleus in the group

[2] W. Hauser and H. Feshbach, *Phys. Rev.* 87, 366 (1952).

[3] J. M. Blatt and V. F. Weisskopf, *Theoretical Nuclear Physics*, p. 360, Wiley, New York, 1952.

[4] B. Margolis, *Phys. Rev.* 88, 327 (1952).

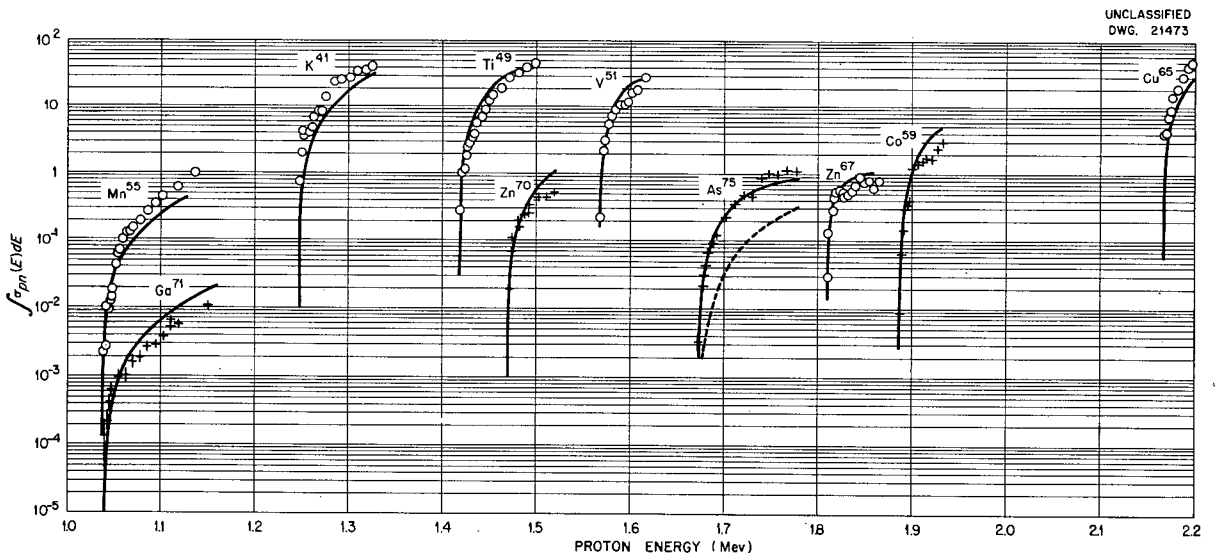


**Fig. 1.2. Comparison of (p,n) Yields with the Continuum Theory.**

is the product of the $Zn^{70}(p,n)Ga^{70}$ reaction, and it is assigned one unit of angular momentum in accordance with the Nordheim rule. The $Ge^{73}$ curve is omitted because consistent data have not been obtained on various targets.

The resulting theoretical curves agree within a factor of 2 with the experimental curves. The shapes of the curves are also in qualitative agreement, but this is not of great significance since this is a semilog plot of thick-target yields. The dotted curve for arsenic is somewhat below the experimental results, which is evidence that the ground state of $Se^{75}$ is $p_{1/2}$.

It should be explicitly stated that there is a somewhat arbitrary constant in this plot, namely, the exact value assumed for the nuclear radius. In the present work, this value was taken to be $1.4 \times 10^{-13} A^{1/3}$ so that experiment and theory would agree (on the average). An accurate measure of the counter efficiency may show that there is an error in these measurements that amounts to as much as a factor of 2, in which case the radius would have to be assigned some other arbitrary value between 1.3 and $1.5 \times 10^{-13} A^{1/3}$ cm in order to force average agreement between theory and experiment.

## ELASTIC SCATTERING ANGULAR DISTRIBUTIONS OF FAST NEUTRONS ON LIGHT NUCLEI

H. B. Willard J. K. Bair
J. D. Kington

In principle, angular distributions of elastically scattered neutrons can be measured by striking a small scattering volume of the element to be investigated with a well-defined plane wave of neutrons and by detecting the scattered wave with a point-source detector. In practice, severe limitations are imposed by source strength, background, and detector efficiency. However, Walt and Barschall[5] have recently succeeded in measuring distributions of 1-Mev neutrons scattered by 11 elements that ranged from iron through bismuth. It was therefore decided, in connection with the present work on the polarization of nuclear reactions, first to undertake a study of the differential cross section for elastic scattering of neutrons below 1.5 Mev in energy by lithium, beryllium, boron, and carbon at and between all resonances.

The $Li^7(p,n)Be^7$ reaction served as a convenient source of neutrons, even though a second lower energy group interferes somewhat with measurements above the 0.6-Mev neutron energy. The target thicknesses were varied between 5 and 75 kev, depending upon the resonance of interest. Cylindrical scatterers that were 3 in. in height and with diameters such as to give a minimum transmission of about 70% were located 18 to 24 in. from the rotating lithium target. Scattered neutrons were detected with a hydrogen (propane gas) recoil counter of 1 × 4 in. sensitive volume that was shielded from the direct beam by a paraffin wedge and was located 4 to 5 in. from the sample, as shown in Fig. 1.3. Since, in the laboratory system, the energy of the scattered neutron varies rapidly with angle, the counter bias was so chosen as to give a flat response between 60 and 100% of the incident neutron energy. A typical curve, as measured by the long counter as a reference, is shown in Fig. 1.4. Under these conditions, backgrounds averaged 50% and counting times were 15 to 30 min per angle. The data thus far obtained are shown in Fig. 1.3, and are uncorrected for multiple scattering in the sample, the finite size of the scatterer, and the finite solid angle subtended by the counter.

These distributions are being analyzed so that the spins and parities of the excited states observed can be determined.

## $Li^7(d,t)Li^6$ REACTION

R. L. Macklin H. E. Banta

The cross section for the reaction $Li^7(d,t)Li^6$ has been measured by collecting and measuring the tritium produced. The targets are enriched $Li^7F$ evaporated onto aluminum disks. The tritium produced is driven out by heating the targets in a hydrogen-argon atmosphere and is collected in a proportional counter; the beta disintegrations of the tritium are then counted. When this method is used, approximately $10^9$ atoms of tritium equals the counter background counting rate. The indicated reproducibility of these measurements is within 10%.

The procedure has been calibrated by the tritium produced by the $Li^6(n,\alpha)t$ reaction in a known neutron flux, and by the tritium ions from a Cockcroft-Walton accelerator. While further work

[5] M. Walt and H. H. Barschall, *Phys. Rev.* 90, 714L (1953).

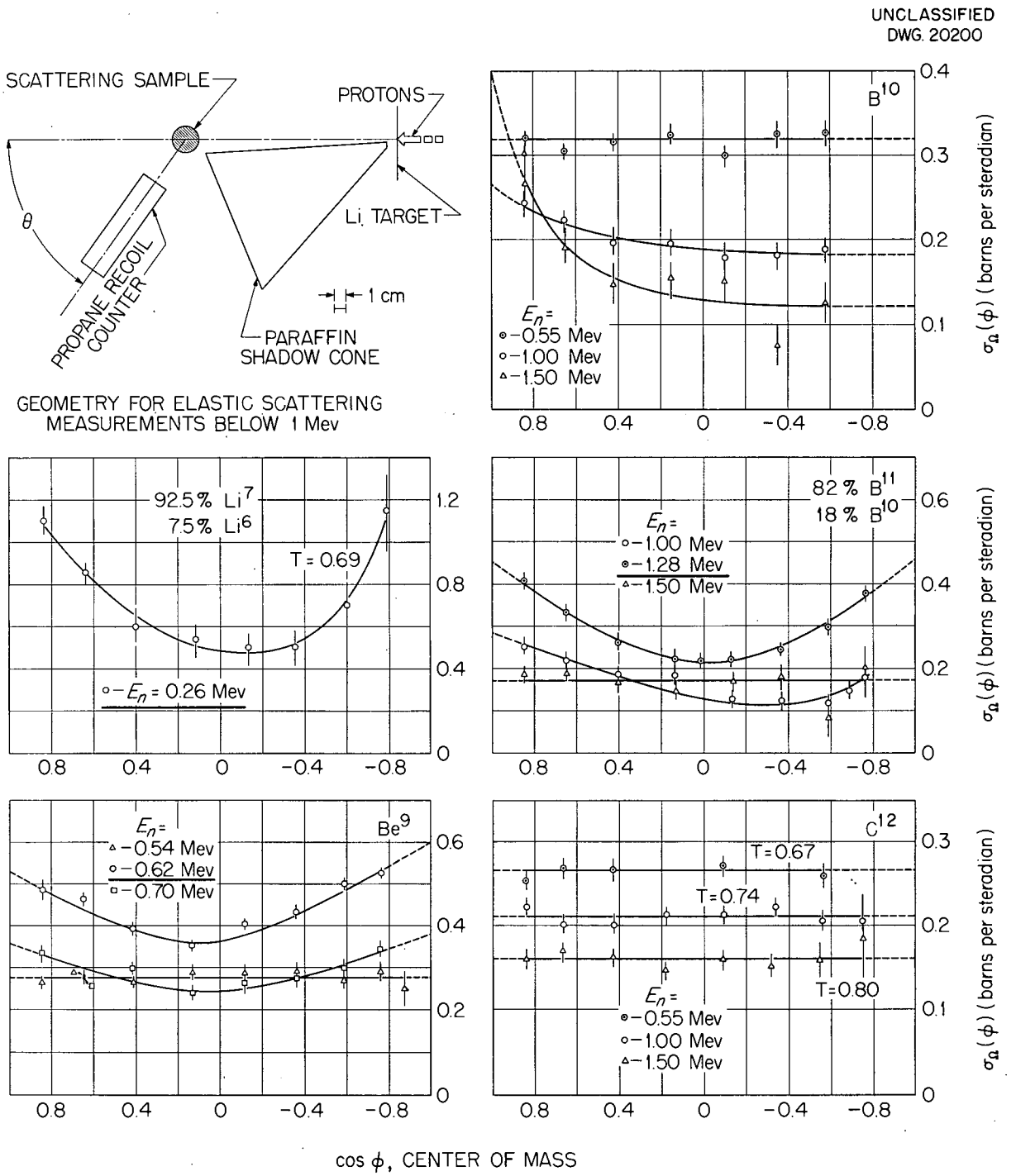


**Fig. 1.3. Elastic Scattering Angular Distributions for Fast Neutrons.** Preliminary-Data Resonance Energies Underlined.

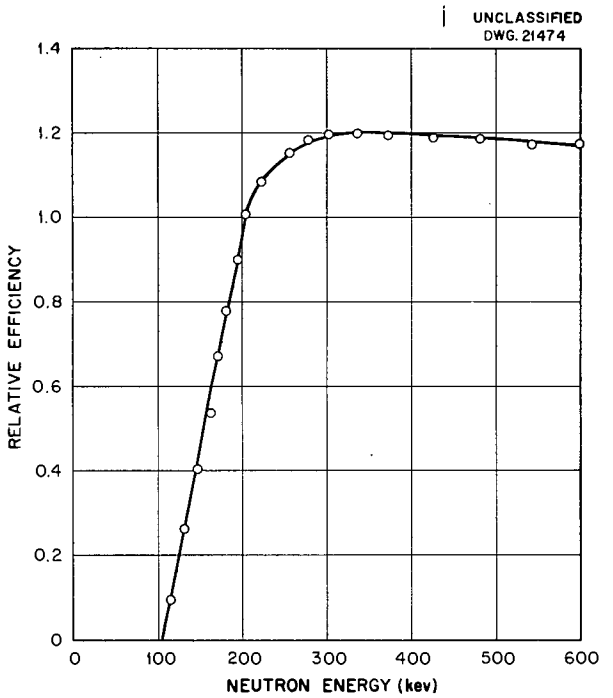


**Fig. 1.4. Relative Response of Neutron Recoil Counter.**

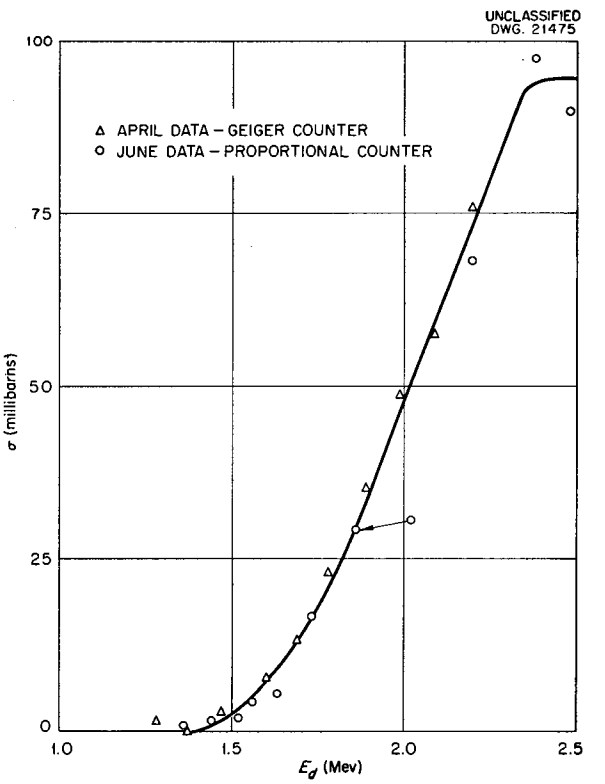


**Fig. 1.5. $Li^7(d,t)Li^6$ Reaction.**

is necessary, on the second method in particular, a final accuracy of ±10% for the cross sections does not seem to be unreasonable. The cross section increases from threshold (1.3 Mev) to the maximum energy obtainable with the 2-Mev Van de Graaff generator (2.5 Mev), and is approximately 100 millibarns at this maximum energy (Fig. 1.5).

## ANGULAR DISTRIBUTIONS OF ALPHA PARTICLES FROM THE $Na^{23}(p,\alpha)Ne^{20}$ REACTION

P. H. Stelson

A scattering chamber has been built to be used with the Van de Graaff generator for measurements of angular distributions of charged particles and for angular correlations of charged particles and gamma rays. Figure 1.6 is a schematic diagram of the apparatus. The beam from the Van de Graaff enters from the left. The following parts appear in the drawing: four adjustable slits for trimming the beam, sylphons to allow movement of the chamber for alignment, glass sections containing rotating quartz viewers on which cross hairs are marked, a tantalum diaphragm to intercept particles scattered by the slits, double rotating seal and detector supports, a target assembly, and an insulated, retractable beam collector cup for current measurements. A degree scale is mounted on top of the chamber for angle measurements. By means of the valve arrangement shown, a target can be admitted without disturbing the vacuum in the chamber. The angle between the plane of the target and the plane perpendicular to the beam is variable.

The scattering chamber has been used for measuring the angular distribution of alpha particles, which are produced by the $Na^{23}(p,\alpha)Ne^{20}$ reaction and lead to the ground state of the residual $Ne^{20}$ nucleus, at six resonances that occur in the region $E_p$ = 1 to 2 Mev. The particles were detected with a gas-filled counter that was fitted with a thin (0.5 air-cm thickness) nickel foil window. A schematic diagram of the counter is shown in Fig. 1.6. A second identical counter was used as a monitor. By means of pulse-height selection, the alpha particles that leave $Ne^{20}$ in the ground state could be clearly distinguished from those that lead to the first excited state. The targets were prepared

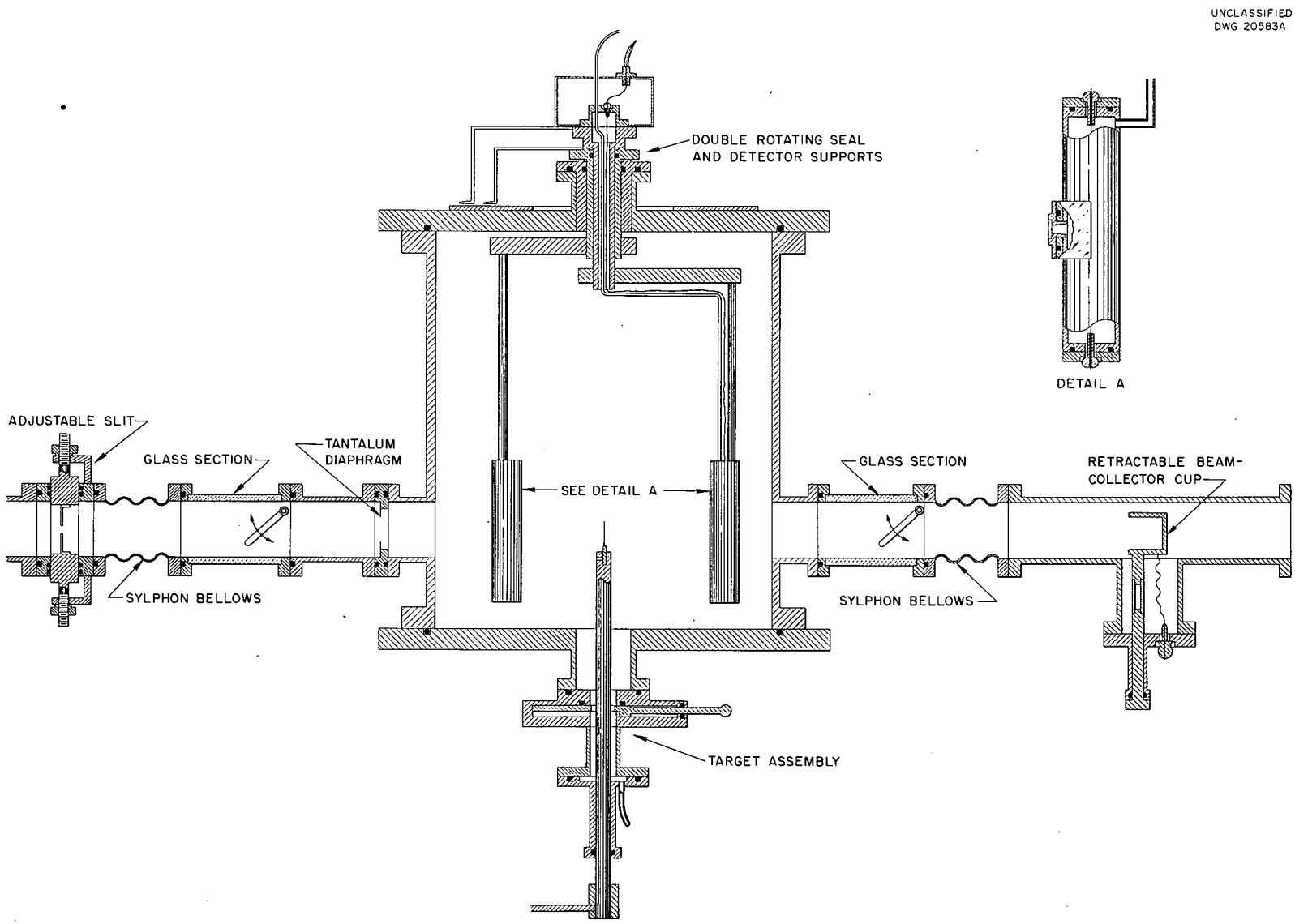


**Fig. 1.6. Scattering Chamber.**

by vacuum evaporation of sodium iodide onto thin (25 $\mu g/cm^2$) Formvar backings.

The ground state of $Ne^{20}$ is a $0^+$ state, and consequently certain types of resonant states are strictly forbidden to decay by this channel. If the ground state of sodium is assigned an even parity, as is indicated by the shell model, the states which can decay by this channel are restricted to the sequence $0^+$, $1^-$, $2^+$, $3^-$, etc. The calculated angular distribution for a given type of state is not unique in many cases in that an unknown mixture of the channel spins enters, as well as possible admixtures of higher l-values. The most plausible assignments for the character of the resonances on the basis of the observed angular distributions are being studied. Three of the angular distributions obtained are shown in Figs. 1.7, 1.8, and 1.9 for the resonances at 1.012, 1.287, and 1.137 Mev, respectively.

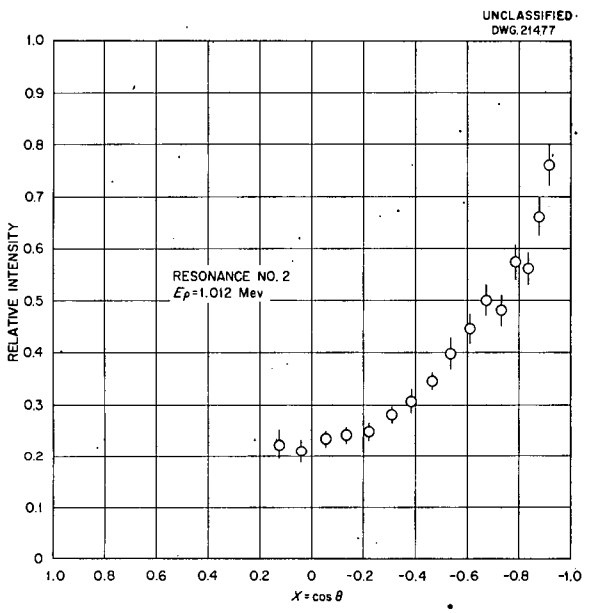


**Fig. 1.7. Angular Distributions of the Ground State Alpha-particles Produced by the $Na^{23}(p,\alpha)Ne^{20}$ Reaction of Resonances Indicated.**

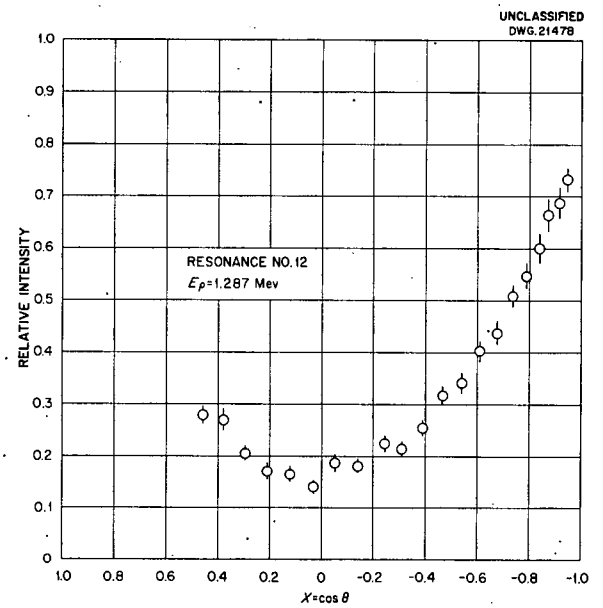


**Fig. 1.8. Angular Distributions of the Ground State Alpha-particles Produced by the $Na^{23}(p,\alpha)Ne^{20}$ Reaction of Resonances Indicated.**

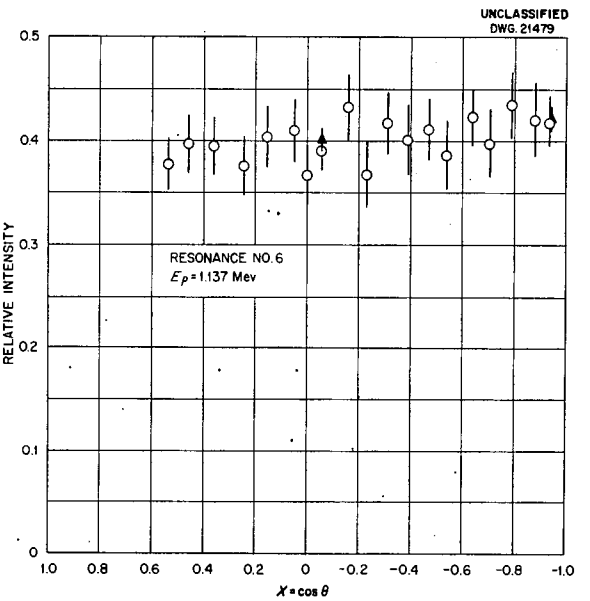


**Fig. 1.9. Angular Distributions of the Ground State Alpha-particles Produced by the $Na^{23}(p,\alpha)Ne^{20}$ Reaction at Resonances Indicated.**

# 2. RADIOACTIVITY AND NUCLEAR ISOMERISM

## ANGULAR CORRELATION OF GAMMA RAYS

E. D. Klema F. K. McGowan

The data obtained for the correlation of the gamma rays from the excited states of $Ni^{60}$ have been analyzed, and the results have been published.[1] The correlation function obtained from six runs with a dilute cobalt chloride source, each with data taken at 19 angular positions and with total coincidence counts of from $2 \times 10^5$ to $4 \times 10^5$, is

$$W(\theta) = 1 + (0.131 \pm 0.017) \cos^2 \theta + (0.024 \pm 0.017) \cos^4 \theta .$$

The theoretical correlation function for two quadrupole transitions between levels of angular momenta 4, 2, and 0, when smeared out to take into account the finite angular resolution of the detectors, is

$$W(\theta) = 1 + 0.1203 \cos^2 \theta + 0.0314 \cos^4 \theta .$$

The measured anisotropy $R$ [$R \equiv (a_2 + a_4)/a_0$, where $W(\theta) = a_0 + a_2 \cos^2 \theta + a_4 \cos^4 \theta$] is $0.1547 \pm 0.0010$. This is to be compared with the expected value for $R$ of 0.1517. A change in the anisotropy to a value of $0.1453 \pm 0.0023$ that resulted from a chemical change in the source was observed.

The angular correlations of the 624–513-kev and the 1045–513-kev cascades in $Pd^{106}$ have been measured, and the results have been submitted to the *Physical Review* for publication. A dilute solution of ruthenium chloride was used as a source, and the data were taken at 19 angular positions. The effect of the higher energy cascades was taken into account by measuring both the composite correlation of the 624–513-kev cascade and the higher energy cascades and by measuring the correlation that results from the higher energy cascades alone. A total of $2.8 \times 10^5$ coincidence counts was obtained in the runs on the composite correlation, and $1.2 \times 10^4$ counts were measured in the runs on the higher energy cascades. The measured correlation function of the 624–513-kev cascade is

$$W(\theta) = 1 + (0.3456 \pm 0.0079) P_2(\cos \theta) + (1.109 \pm 0.012) P_4(\cos \theta) ,$$

in which the finite angular resolution of the apparatus has been taken into account. The theoretical correlation function for the spin sequence 0 - 2 - 0 is

$$W(\theta) = 1 + 0.3571 P_2(\cos \theta) + 1.1429 P_4(\cos \theta) .$$

The discrepancies between the theoretical and experimental coefficients of $P_2$ and $P_4$ are about 3% and are 1.5 and 2.8 times the standard deviations of the measurements. It is believed that these discrepancies are caused by interfering radiation in the windows of the differential analyzers, even for the narrowest windows it was practical to use.

The correlation function of the 1045–513-kev cascade was measured in a series of four runs with a total of $10^5$ counts and found to be

$$W(\theta) = 1 + (0.0921 \pm 0.0027) P_2(\cos \theta) + (0.0350 \pm 0.0092) P_4 \cos \theta .$$

This measurement establishes the spin of the 1550-kev level as 2 and gives the intensity of the electric quadrupole radiation as $4.24 \pm 0.14\%$, relative to the intensity of the magnetic dipole radiation in the 1045-kev transition.

## ANGULAR CORRELATIONS OF GAMMA RAYS IN $Ta^{181}$

F. K. McGowan

The results of the directional angular correlation of the 132–480-kev gamma-ray cascade in $Ta^{181}$ were given in previous quarterly reports.[2] New measurements now include the differential directional angular correlation of the 132–480-kev gamma-ray cascade, the 132–345-kev gamma-gamma directional angular correlation, and the 345–135-kev gamma-gamma directional angular correlation.

A fast coincidence spectrometer employing sodium iodide detectors has made possible the measurement of the differential directional angular correlation of the 132–480-kev gamma-ray cascade, that is, directional angular correlation as a function

[1] E. D. Klema and F. K. McGowan, *Phys. Rev.* 91, 616 (1953).

[2] F. K. McGowan, *Phys. Quar. Prog. Rep. June 20, 1952*, ORNL-1365, p. 8; *Phys. Quar. Prog. Rep. Sept. 20, 1952*, ORNL-1415, p. 12; *Phys. Quar. Prog. Rep. Dec. 20, 1952*, ORNL-1496, p. 7.

of the time of emission of the 480-kev transition. For liquid sources of hafnium metal and $HfO_2$ in hydrofluoric acid as a solvent and for a resolving time, $2\tau_0$, equal to $1.3 \times 10^{-8}$ sec, the anisotropy is independent of the emission time of the 480-kev transition to within ±4%.

In order to obtain the experimental angular correlation function for the 132–345-kev gamma-ray cascade, the coincidences were collected at a time delay of $10^{-8}$ sec, which is sufficient to resolve all prompt coincidences that result from the 345–135-kev gamma-ray cascade. The window of the differential pulse-height analyzer, which accepts only the full energy pulse spectrum peak of the 345-kev gamma ray, also accepts a small portion of the Compton recoil electron pulse distribution from the 480-kev gamma ray. Thus the data collected represent a composite correlation function of the 132–480-kev and 132–345-kev gamma-ray cascades. The contribution that results from the 132–480-kev gamma ray is removed from the composite function by a direct measurement of the 132–480-kev gamma-gamma correlation at the same time delay and a determination of the number of counts in the window from the 480-kev transition.

In order to measure the correlation function of the 345–135-kev gamma-ray cascade, the following set of experiments was performed. At a time delay of $-7.7 \times 10^{-9}$ sec, coincidences were collected that were due to 132–480-kev, 132–345-kev, and 345–135-kev gamma-ray cascades. Since the observed angular correlation functions for the 132–480-kev and 132–345-kev gamma-ray cascades are independent of the time of emission of the 480 and 345-kev transitions, their effect in the composite correlation function is removed by a direct measurement. That is, the coincidence rates for 132–480-kev and 132–345-kev are measured at a time delay of $15.4 \times 10^{-9}$ sec. At this time delay, the coincidence rate is equal to that at a time delay of $-7.7 \times 10^{-9}$ second. A determination of the time delays that could be used in these measurements was obtained from a measurement of time-resolution curves for both prompt and delayed events. For instance, the latter measurements involved a measurement of a shift of $6 \times 10^{-10}$ sec of the centroids of two time resolution curves to within $\pm 5 \times 10^{-11}$ second. In addition to the contribution from the 132–480-kev and 132–345-kev gamma-ray cascades, there is another source of coincidences at a time delay of $-7.7 \times 10^{-9}$ sec, which is not present at a time delay of $15.4 \times 10^{-9}$ sec because of the Compton scattering of the 480-kev gamma ray between the detectors. This source of coincidences was measured directly by means of the 512-kev gamma ray from $Sr^{85}$, and it was found to be a 10% isotropic effect.

The influence of perturbing interactions in the intermediate state, which are caused by extranuclear fields, on the angular correlation of the 345–135-kev gamma-ray cascade was checked by measurements that were taken with a liquid source of $HfO_2$ in hydrofluoric acid as a solvent and with a polycrystalline source of $HfF_4$. Identical angular correlation functions were obtained; thus there is an indication that the intermediate state is prompt. This result is also assurance that the contributions from the 132–480-kev and 132–345-kev gamma-ray cascades have been properly removed from the composite data. The angular correlation coefficients, corrected for finite angular resolution, of the various terms in the expansion of the correlation function in Legendre polynomials for the 345–135-kev gamma-ray cascade are given in Table 2.1.

The directional angular coefficients for the various gamma-ray cascades in $Ta^{181}$ are summarized in Table 2.2. An analysis of these results, in combination with the measured $K$-shell internal conversion coefficients (shown in Fig. 2.1), indicates that an unambiguous assignment of the angular momenta of these three excited states in $Ta^{181}$ and a classification (multipole order and character) of these gamma rays are possible. Many spin sequences must be considered in the analysis, and, for completeness, those that are excluded by the experimental results are enumerated. In the case of the 132–480-kev gamma-ray cascade, the following decay sequences do not fit experiment: $j, j \pm 1, j \pm 2(E2)\ j = 7/2, 7/2 \pm 1(Q + D)7/2$ except the decay sequence $5/2(E2)9/2(E2 + M1)7/2$; $j, j \pm 1(Q + D)\ j = 7/2, 7/2 \pm 1(Q + D)7/2$; and $j \pm 2(E2 + M3)\ j = 7/2, 7/2 \pm 1(Q + D)7/2$. In this notation, $j_1 = j, j \pm 1$, or $j \pm 2$ and all combinations are considered. Since many of the possible spin sequences are already excluded by the correlation function of the 132–480-kev cascade, the only two spin sequences that need be considered in the analysis of the 132–345-kev gamma-ray cascade are $5/2(E2)9/2(Q + D)9/2$ and $5/2(E2)\ 9/2(Q + D)7/2$. The sign of the coefficient $(A_4)_{exp}$ immediately excludes the latter spin sequence.

TABLE 2.1. DIRECTIONAL ANGULAR CORRELATION COEFFICIENTS FOR THE 345–135-kev GAMMA-RAY CASCADE

| EXPERIMENT NUMBER | FORM OF THE SOURCE | EXPERIMENTAL COEFFICIENTS | |
|---|---|---|---|
| | | $A_2$ | $A_4$ |
| 1 | $Hf^{181}O_2$ in HF as a solvent | 0.2003 | –0.0343 |
| 2 | $Hf^{181}O_2$ in HF as a solvent | 0.2292 | –0.0541 |
| 3 | Polycrystalline $Hf^{181}F_4$ | 0.2010 | –0.0962 |
| 4 | Polycrystalline $Hf^{181}F_4$ | 0.2196 | –0.0712 |
| 5 | $Hf^{181}O_2$ in HF as a solvent | 0.1908 | –0.0547 |
| 6 | Polycrystalline $Hf^{181}F_4$ | 0.1710 | –0.0086 |

TABLE 2.2. DIRECTIONAL ANGULAR CORRELATION COEFFICIENTS FOR THE GAMMA-RAY CASCADES IN $Ta^{181}$

| CASCADE | FORM OF THE SOURCE | NUMBER OF COINCIDENCES COLLECTED | EXPERIMENTAL COEFFICIENTS | |
|---|---|---|---|---|
| | | | $A_2$ | $A_4$ |
| 132–480-kev | Hf metal in HF as a solvent<br>$Hf^{181}O_2$ in HF as a solvent | $4.3 \times 10^6$ | –(0.280 ± 0.004) | –(0.058 ± 0.003) |
| 132–345-kev | $Hf^{181}O_2$ in HF as a solvent | $6.8 \times 10^5$ | 0.110 ± 0.012 | 0.029 ± 0.014 |
| 345–135-kev | $Hf^{181}O_2$ in HF as a solvent<br>Polycrystalline $Hf^{181}F_4$ | $1.6 \times 10^6$ | 0.202 ± 0.009 | –(0.053 ± 0.014) |

Although $\alpha^K_{exp}$ (135-kev) indicates that the 135-kev transition is predominantly $M1$, the uncertainty in the measurement does not exclude a small admixture of $E2$ radiation. However, the presence of a $P_4(\cos\theta)$ term in the observed angular correlation function of the 345–135-kev gamma-ray cascade requires an admixture of $E2$ radiation. This is the first correlation that has been observed in which each transition is a mixture of electric and magnetic multipole radiation.

The computation of a correlation function for a mixed-mixed gamma-ray cascade is quite tedious. An explicit form of the correlation function has been derived by Rose.[3] The function contains the sum of nine separate correlation functions, each multiplied by various powers of $\delta_1$ and $\delta_2$ or products of these, where $\delta_1^2$ and $\delta_2^2$ are the reduced matrix elements[4] and are defined as the intensity ratio (in this case) of quadrupole radiation to dipole radiation in transitions 1 and 2, respectively. In the computation of the correlation of the function to compare with experiment, $\delta_1$ and $\delta_2$ must be allowed to take on both positive and negative values over four decades.

Of the possible spin sequences, $j$, $j \pm 1(Q + D)$ $j = 7/2$, $7/2 \pm 1(Q + D)7/2$, that need be considered for the 345–135-kev gamma-ray cascade, only the spin sequence $9/2(E2 + M1)9/2(E2 + M1)7/2$ fits experiment. A summary of the conclusions obtained from the analysis of the angular correlation results, in combination with the measured $K$-shell internal conversion coefficients, is tabulated in Table 2.3.

[3] M. E. Rose, *Phys. Rev.* (to be published).

[4] L. C. Biedenharn and M. E. Rose, *Revs. Mod. Phys.* 25, 729 (1953).

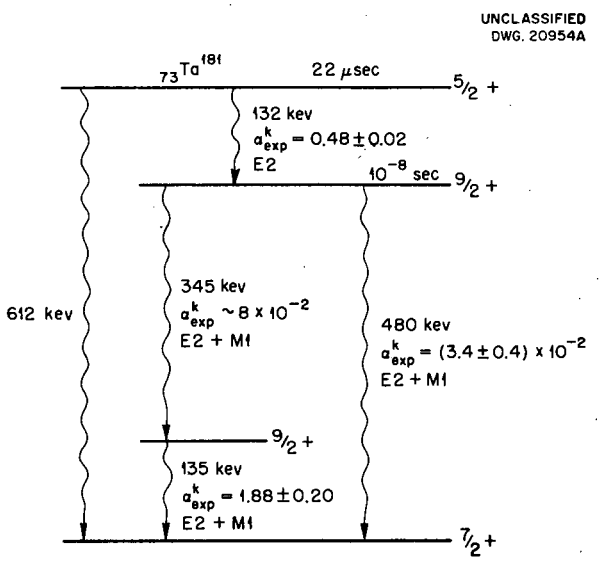


**Fig. 2.1. Decay Scheme of $Ta^{181}$ with *K*-Shell Internal Conversion Coefficients.**

The factors $G_{\nu j}$ are the attenuation coefficients in the correlation function

$$W(\theta) = 1 + \sum_{\nu} G_{\nu j} A_{\nu} P_{\nu} (\cos \theta) ,$$

which represent the effect of the perturbing interactions in the intermediate state of the nucleus. These attenuation coefficients are independent of the nature of the transitions to and from the intermediate state.[5] If the attenuation coefficients are attributed entirely to the interaction of the nuclear electric quadrupole moment of the 480-kev state with the gradient of the electric field from its surroundings (liquid state), the values quoted in Table 2.3 are not too consistent for $\delta_{480} = 1.25$, which was obtained from the measured *K*-shell internal conversion coefficient. However, for $\delta_{480} = 1.7$, a consistent set of attenuation coefficients, $G_{2\ 9/2} = 0.735$ and $G_{4\ 9/2} = 0.497$, is obtained. This leads to $\alpha^K(480) = 2.8 \times 10^{-2}$, which is still in fair agreement with the measured value. The attenuation coefficients determined from the 132–480-kev correlation function should, of course, be the same in the 132–345-kev angular correlation and are used in the analysis to determine $\delta_{345}$. Another independent determination of $\delta_{345}$ is obtained from the 345–135-kev angular correlation.

It is gratifying to find an unambiguous assignment of the angular momenta and relative parities of these excited states in $Ta^{181}$ (see Fig. 2.1) which is consistent with both the *K*-shell internal conversion coefficient and angular correlation measurements.

[5] A. Abragam and R. V. Pound, *Phys. Rev.* (to be published).

## INTERNAL CONVERSION ELECTRON-GAMMA DIRECTIONAL ANGULAR CORRELATION OF $Bi^{207}$

F. K. McGowan

The internal conversion electron-gamma directional angular correlation between the *K*-shell internal conversion electrons of the 1.055-Mev transition and the 0.555-Mev gamma ray of $Pb^{207}$, which follow the electron capture decay of $Bi^{207}$, has been measured. The results have been submitted for publication in the *Physical Review* as a Letter to the Editor.

**TABLE 2.3. SPIN ASSIGNMENTS OF THE EXCITED STATES AND CHARACTER OF THE GAMMA RADIATIONS IN $Ta^{181}$**

| CASCADE | SPIN SEQUENCE | $\delta_\gamma$ | $(G_{2\ 9/2})_{exp}$ | $(G_{4\ 9/2})_{exp}$ |
|---|---|---|---|---|
| 132–480-kev | 5/2(*E*2)9/2(*E*2 + *M*1)7/2 | $\delta_{480} = 1.25^{+0.29}_{-0.22}$ | $0.63^{+0.07}_{-0.02}$ | $0.60^{-0.08}_{+0.11}$ |
| 132–345-kev | 5/2(*E*2)9/2(*E*2 + *M*1)9/2 | $\delta_{345} = 1.0 \pm 0.1$ | | |
| 345–135-kev | 9/2(*E*2 + *M*1)9/2(*E*2 + *M*1)7/2 | $\delta_{345} = 1.0$<br>$\delta_{135} = 0.5 \pm 0.05$ | | |

### INTERNAL CONVERSION AND DIRECTIONAL ANGULAR CORRELATION OF THE $Bi^{207}$ GAMMA RAYS

F. K. McGowan E. C. Campbell

The *K*-shell internal conversion coefficients and the directional angular correlation of the 1.055- and 0.555-Mev gamma rays of $Pb^{207}$ that follow the electron capture decay of $Bi^{207}$ have been measured. The results have been submitted for publication in the *Physical Review* as a Letter to the Editor.

### MEASUREMENT OF THE HALF LIFE AND GAMMA SPECTRUM OF $Pb^{207m}$ BY LIQUID-FLOW TECHNIQUE

E. C. Campbell

The chemical separation procedure previously described[6] has been used to obtain the half life of the short-lived isomer in $Pb^{207m}$ from measurements of the attenuation of the activity downstream from the source.

A schematic diagram of the essential parts of the apparatus is shown in Fig. 2.2. The source consists of a small amount of the anion-exchange resin, Dowex-1, which has been treated by being placed in contact with a solution (0.5 *M* HCl) that contained radioactive $Bi^{207}$. It is found that at equilibrium the concentration of the bismuth inside the resin is about $10^5$ times the concentration in the surrounding solution. The radioactive bismuth, which has a half life of about 50 years, decays by electron capture via an isomeric state in $Pb^{207}$ The radioactive $Pb^{207m}$ is relatively free to diffuse cut of the tiny resin spheres into the surrounding liquid and to be transported downstream to the counter through a horizontal, uniform, cylindrical glass tube.

The horizontal tube is arranged so that it can be slid, while the axis is maintained parallel to itself, through the counter shield. The position of the tube is given by measuring the distance, $x$, between an index marker on the tube and the fixed counter shield. The thallium-activated sodium iodide counter and the associated amplifying and scaling circuits are all standard.

It is expected that the counting rate should decrease according to $e^{-(\lambda_x/v_0)}$ as the distance

[6] E. C. Campbell and F. Nelson, *Phys. Quar. Prog. Rep. Dec. 20, 1952*, ORNL-1496, p. 8; *Phys. Rev.* 91, 499A (1953).

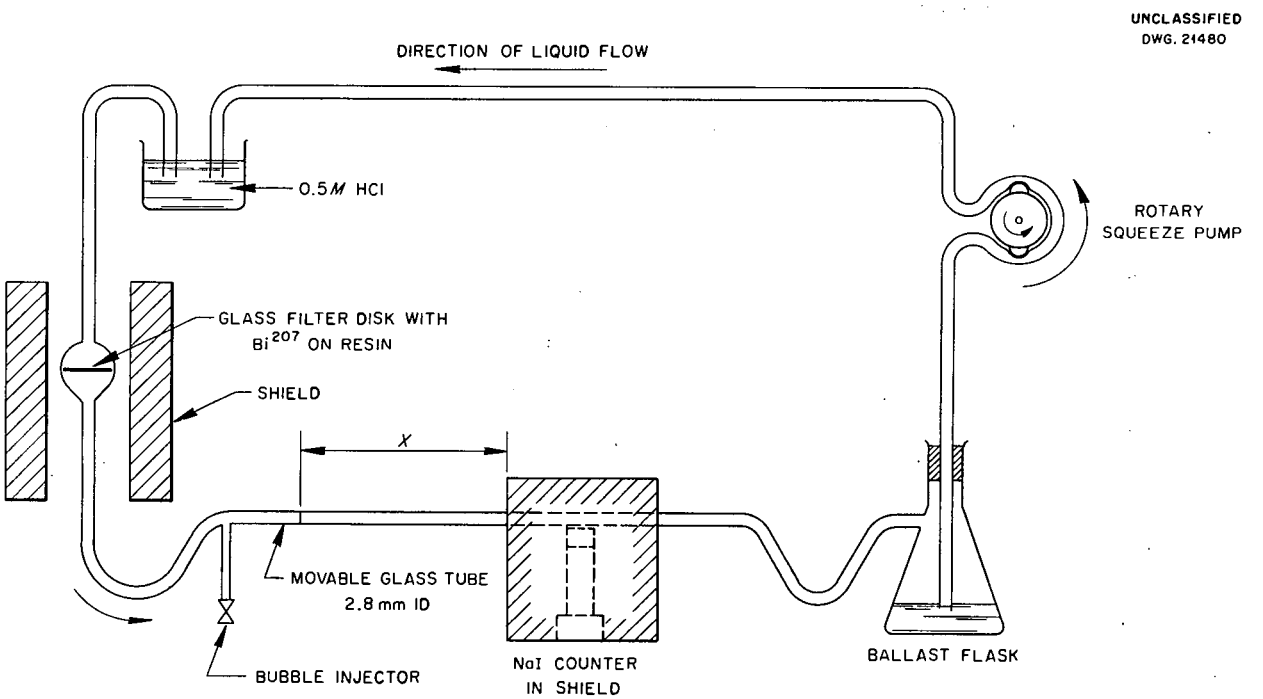


**Fig. 2.2. Schematic Diagram of Apparatus for Measurement of $Pb^{207m}$ Half Life.**

$x$ is varied, where $v_0$ is the velocity of flow and $\lambda$ is the decay constant. In order to avoid complications associated with the nonuniform velocity profile of laminar flow, air was allowed to leak into the system and to form uniform bubbles that were about equal to or larger than the diameter of the tube and were spaced at very regular intervals. The bubbles also provided a direct means of measuring the flow velocity. The time taken for bubbles to travel the distance between two markers 100.0 cm apart on the tube was measured with an electric stop watch during each of the counting intervals. The mean of 72 readings was 4.54 sec, with a standard deviation of 0.09 second.

The results are shown in Fig. 2.3. Between 50,000 and 100,000 counts were taken for each point. A measured background of 17.6 counts/sec, which was obtained with no flow, was subtracted from the observed counting rates to give the points plotted.

The straight line that gives the best fit corresponds to a half-distance, $x_{1/2}$, of 18.5 cm. This value gives a half life of 0.84 sec for the $Pb^{207m}$, with a probable error of 2%.

The yield of the separation process was measured in a separate experiment in which the flow rate through the resin was about 10 ml/second. When the liquid was flowing, it was found that the counting rate of the detector was 15.7% below that for no flow. The counter shielding was arranged so that any counts that resulted from decay downstream from the resin were eliminated. The conclusion is that at least 15.7% of the $Pb^{207m}$ produced is transported by the flowing liquid.

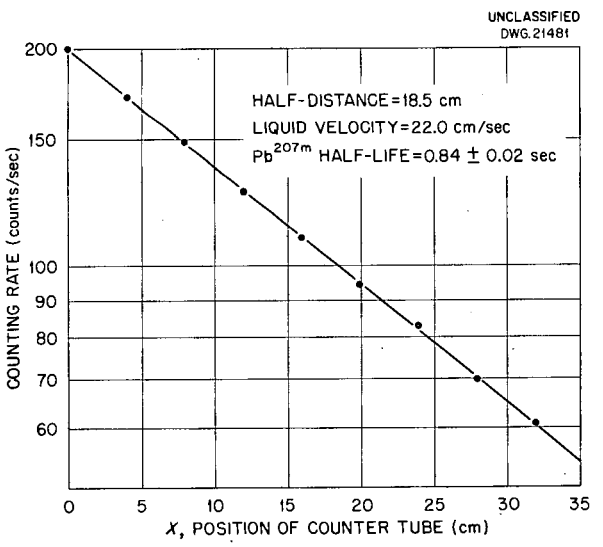


**Fig. 2.3. Attenuation of $Pb^{207m}$ Activity Downstream from Source in Continuous-Flow Experiment.**

The scintillation-counter spectrum of the separated $Pb^{207m}$ shows two gamma rays at energies of 0.555 and 1.055 Mev. These values are in excellent agreement with the values 0.55 and 1.05 Mev[7] that have been measured for the radiations from the short-lived activity of reactor-neutron-irradiated lead[8] produced by the reaction $Pb^{207}(n,n')Pb^{207m}$. The measured half life, 0.84 ± 0.03 sec,[8] of the directly produced isomer is in excellent agreement with that obtained in this experiment.

### FISSION GAMMA-RAY SPECTRUM

R. L. Gamble[9]

The energy spectrum of the prompt gamma rays from the thermal fission of $U^{235}$ is being measured with a single-crystal gamma-ray spectrometer that employs a sodium iodide crystal.

Neutrons from a polonium-beryllium source are moderated by paraffin. The resulting thermal neutrons cause fission of $U^{235}$ in a parallel-plate fission chamber, and the scintillation pulses from the gamma-ray spectrometer are fed into a coincidence circuit with a resolving time of 0.4 $\mu$sec. The coincidence spectrum is measured with a ten-channel pulse-height analyzer. In order to obtain the random coincidence spectrum, a 1-$\mu$sec delay cable is inserted in one leg of the coincidence circuit. The physical arrangement of the experiment is shown in Fig. 2.4. The paraffin moderator is in the form of a cube. The Lucite rod is used to transport the polonium-beryllium source, and it also helps to moderate the fast neutrons. The lead shadow shield protects the crystal from the direct gamma rays from the source, and the lithium shield protects the crystal from thermal neutrons. The photomultiplier tube is not shown.

The detection efficiency of the crystal for gamma rays that originate at the plates of the fission chamber was calculated by numerical integration in which the NBS values of the absorption coefficient of sodium iodide for gamma rays at various

[7] E. C. Campbell and M. Goodrich, *Phys. Rev.* 78, 640 (1950).

[8] E. C. Campbell, *Phys. Quar. Prog. Rep. Sept. 20, 1951*, ORNL-1164, p. 22; *Phys. Quar. Prog. Rep. June 20, 1952*, ORNL-1365, p. 9.

[9] ORINS Fellow, University of Texas.

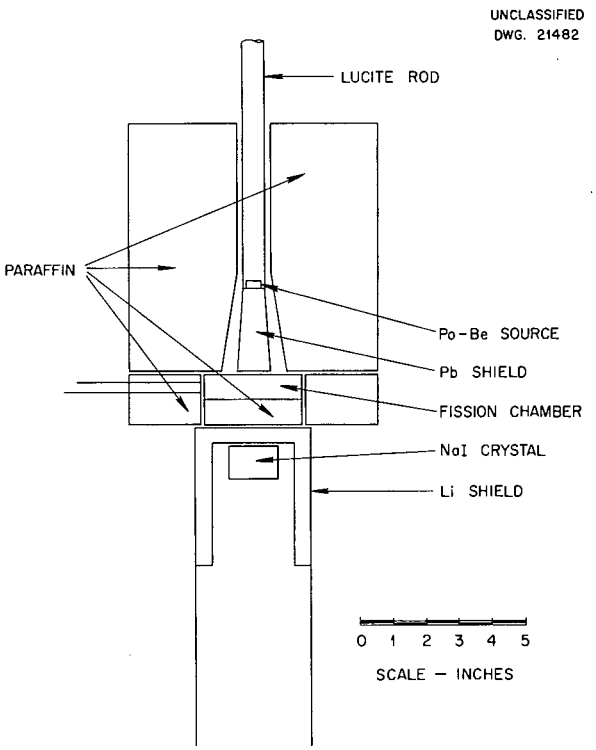


**Fig. 2.4. Geometry of Fission Gamma Experiment.**

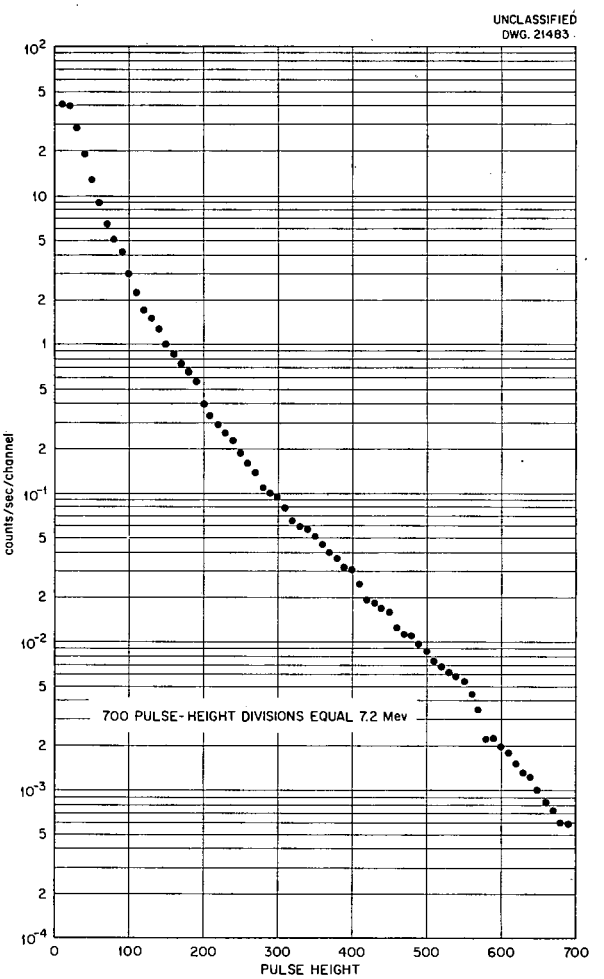


**Fig. 2.5. Fission Gamma Pulse-Height Spectrum.**

energies were used. The counts-per-second vs. pulse-height curve is shown in Fig. 2.5, in which there is no evidence for a line structure in the spectrum.

At present, only a rough translation has been made from the counts-per-second vs. pulse-height curve to the photons-per-Mev vs. energy curve, which is shown in Fig. 2.6. The prompt gamma-ray energy per fission, on the basis of Fig. 2.6, is approximately 8 Mev, and, on the average, about seven photons are emitted per fission between 0.25 and 7 Mev.

### BROAD-BEAM GAMMA-RAY ATTENUATIONS

R. Stephenson P. R. Bell

Experiments are in progress for measuring the attenuation of gamma radiation under broad-beam or poor-geometry conditions. The detector consists of a sodium iodide scintillation counter that is 1½ in. in diameter and 1 in. thick and that rests inside a 22 × 26 in. lead protective barrier that is 12 in. high. The walls of the barrier are 4 in. thick and it is lined with 0.060 in. of cadmium and 0.020 in. of copper to stop lead x rays. The signal from the scintillation counter is amplified by an A-1 and is then fed to the 120 × 20 channel analyzer to obtain the counting rate as a function of pulse height. Sources of various energy can be suspended above the scintillation counter in a small polystyrene cup, and 29½ × 26 in. sheets of 1-in. aluminum or ¼-in. lead absorber are placed between the source and the detector. The distance from the source to the detector is chosen so that the source will be located approximately at the surface of the absorber when the greatest attenuation is obtained for a given run.

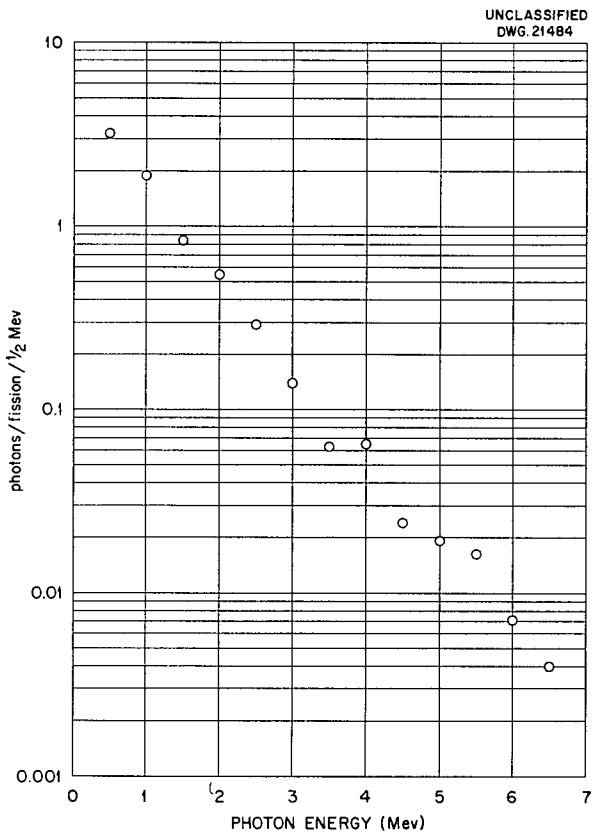


**Fig. 2.6. Energy Distribution of Prompt-Gamma Photons from Fission of $U^{235}$.**

The resulting spectrum consists of a peak that corresponds to the primary gamma energy plus a degraded spectrum of scattered photons of less than the primary energy. This spectrum may be analyzed as follows. First, the primary peak plus its Compton distribution is peeled off to obtain the pure degraded spectrum. By starting at the high-energy end, Gaussians of the proper width, as determined by the resolution of the crystal, and their estimated Compton distributions are successively peeled off to separate the degraded radiation into its components. Biological buildup factors may then be calculated from the relative biological effectiveness of the scattered and the primary radiations.

The following experiments have now been completed:

1. $Cs^{137}$ (661-kev) in lead at 25- and 100-cm distance from source to detector,
2. $Cs^{137}$ in aluminum at 100 cm from the detector,
3. $K^{42}$ (1.51-Mev) in lead at 25 cm from the detector,
4. $K^{42}$ in aluminum at 100 cm from the detector,
5. $Na^{24}$ (2.76- and 1.38-Mev) in lead at 30 cm from the detector,
6. $Na^{24}$ in aluminum at 100 cm from the detector.

It is also planned to measure the attenuation, in lead, aluminum, and water, of the 4.44-Mev gammas from excited carbon by using a polonium-beryllium source and to measure the attenuation of $Cs^{137}$, $K^{42}$, and $Na^{24}$ in water by means of a water tank that is 5 ft in diameter and 5 ft high.

The data obtained to date are presented in Figs. 2.7 through 2.13. A preliminary analysis of older data has shown that the experimentally determined buildup factors in aluminum and lead are of the same order of magnitude as the values calculated theoretically.

### Po-Be AND Po-B GAMMA-RAY SPECTRA

F. C. Maienschein T. A. Love

It is well known that the bombardment of the light element beryllium with alpha particles from polonium not only produces neutrons but also gives off high-energy gamma radiation, and several investigations[10,11,12,13] of the gamma spectrum have repeatedly confirmed the production of a 4.43-Mev gamma ray. During intensity calibrations of a three-crystal spectrometer that was developed in this laboratory, the 4.43-Mev gamma ray was again investigated.[14] Additional measurements have recently been made on this spectrum, and the work has been extended to an examination of the gamma radiation given off when boron is bombarded.

The gamma-ray spectra from the Po-Be and the Po-B sources are produced by the reactions $Be^9(\alpha,n)C^{12*}$ and $B^{10,11}(\alpha,n)N^{13,14*}$, respectively. Both spectra have been examined with the three-crystal pair spectrometer and the single-crystal spectrometer, and the results are given in Figs. 2.14 and 2.15. The high-energy portions

[10] W. Bothe, *Z. Physik* 100, 273 (1936).

[11] H. Maier-Leibnitz, *Z. Physik* 101, 478 (1936).

[12] P. R. Bell and W. H. Jordan, *Phys. Rev.* 79, 392 (1950).

[13] J. Terrell, *Phys. Rev.* 80, 1076 (1950).

[14] F. C. Maienschein, *Multiple-Crystal Gamma-Ray Spectrometer*, ORNL-1142 (July 3, 1952).

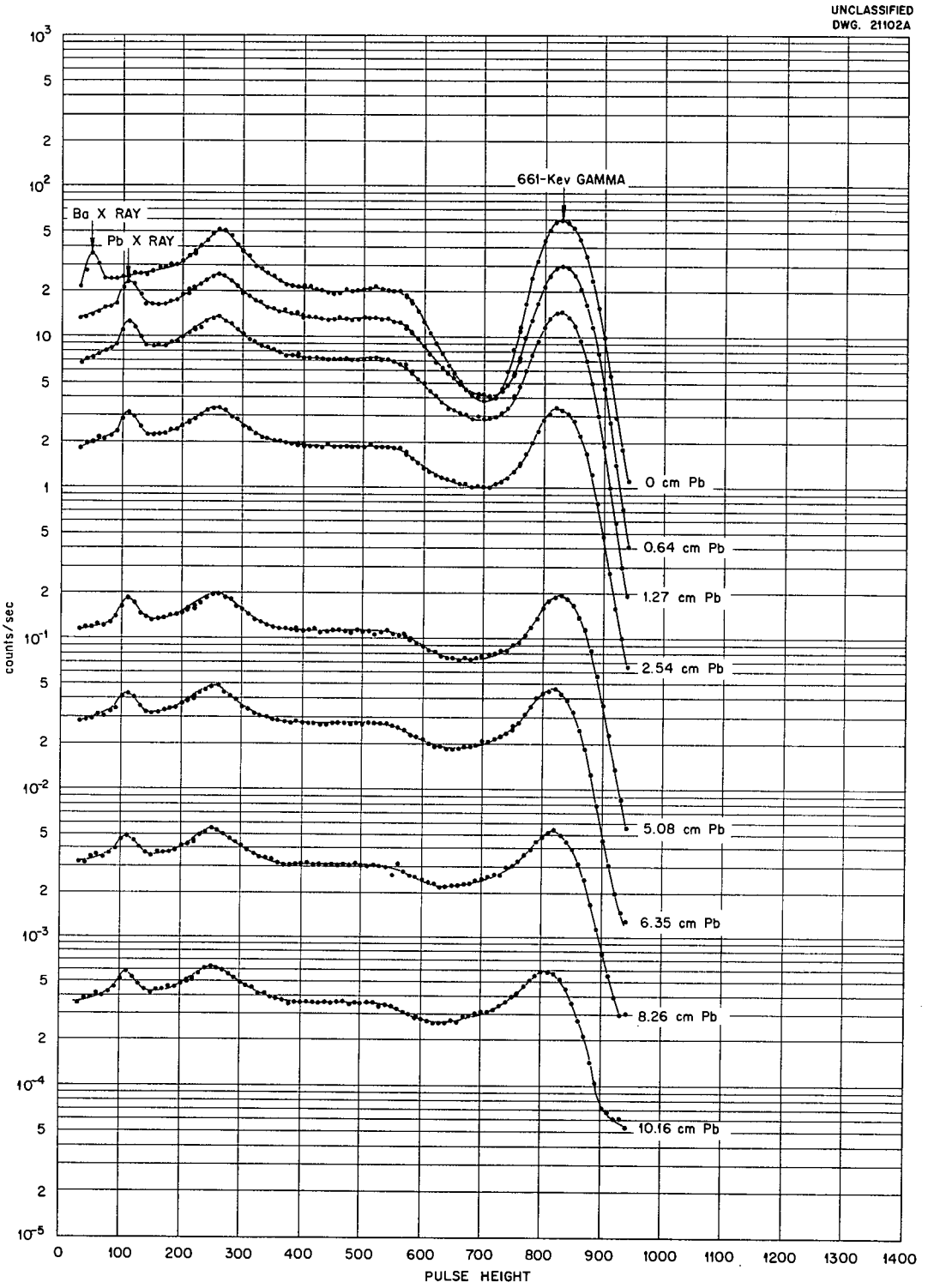


**Fig. 2.7. Broad-Beam Attenuation; $Cs^{137}$ in Lead. Source 25 cm from detector.**

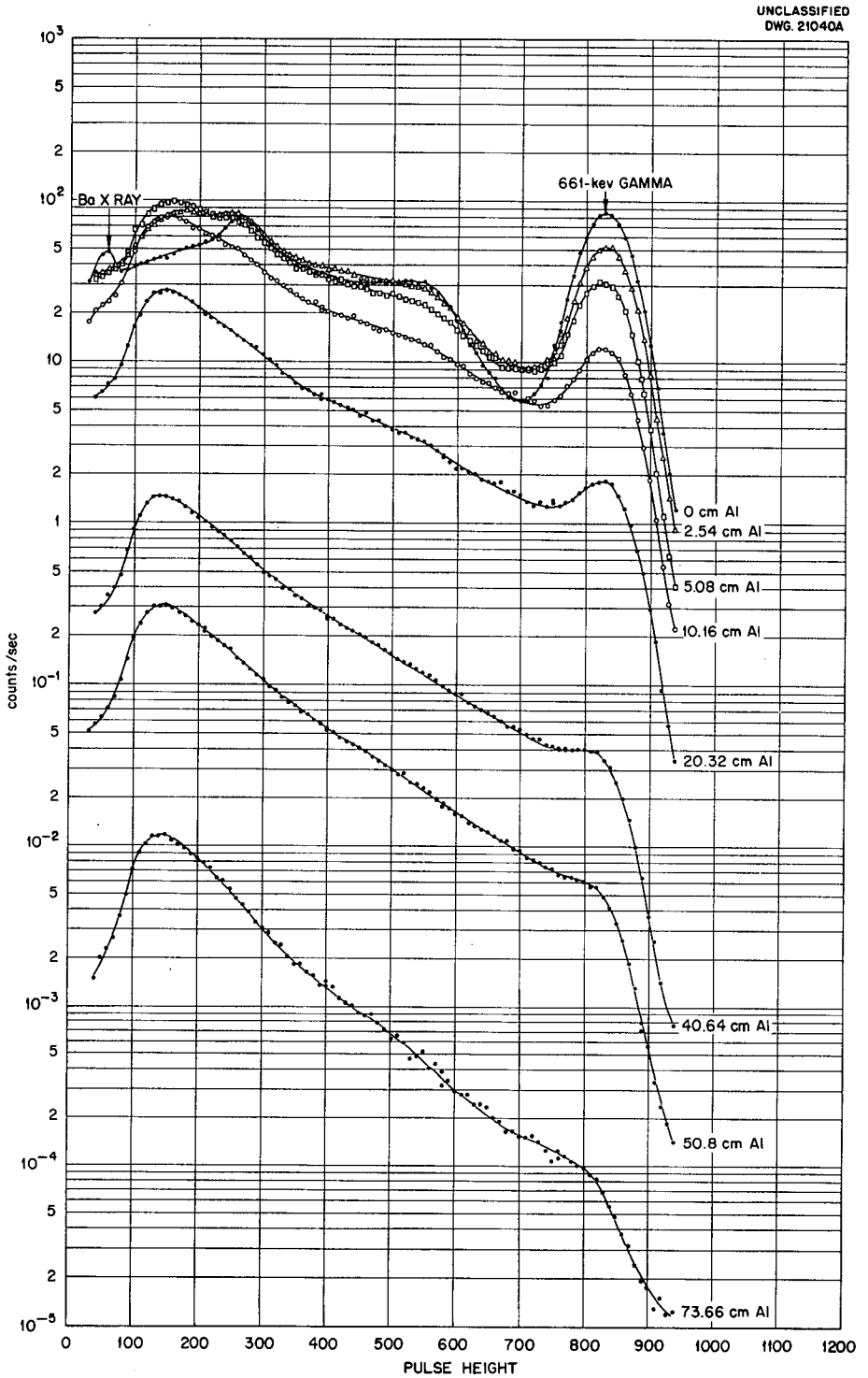


**Fig. 2.8. Broad-Beam Attenuations; $Cs^{137}$ in Aluminum. Source 100 cm from detector.**

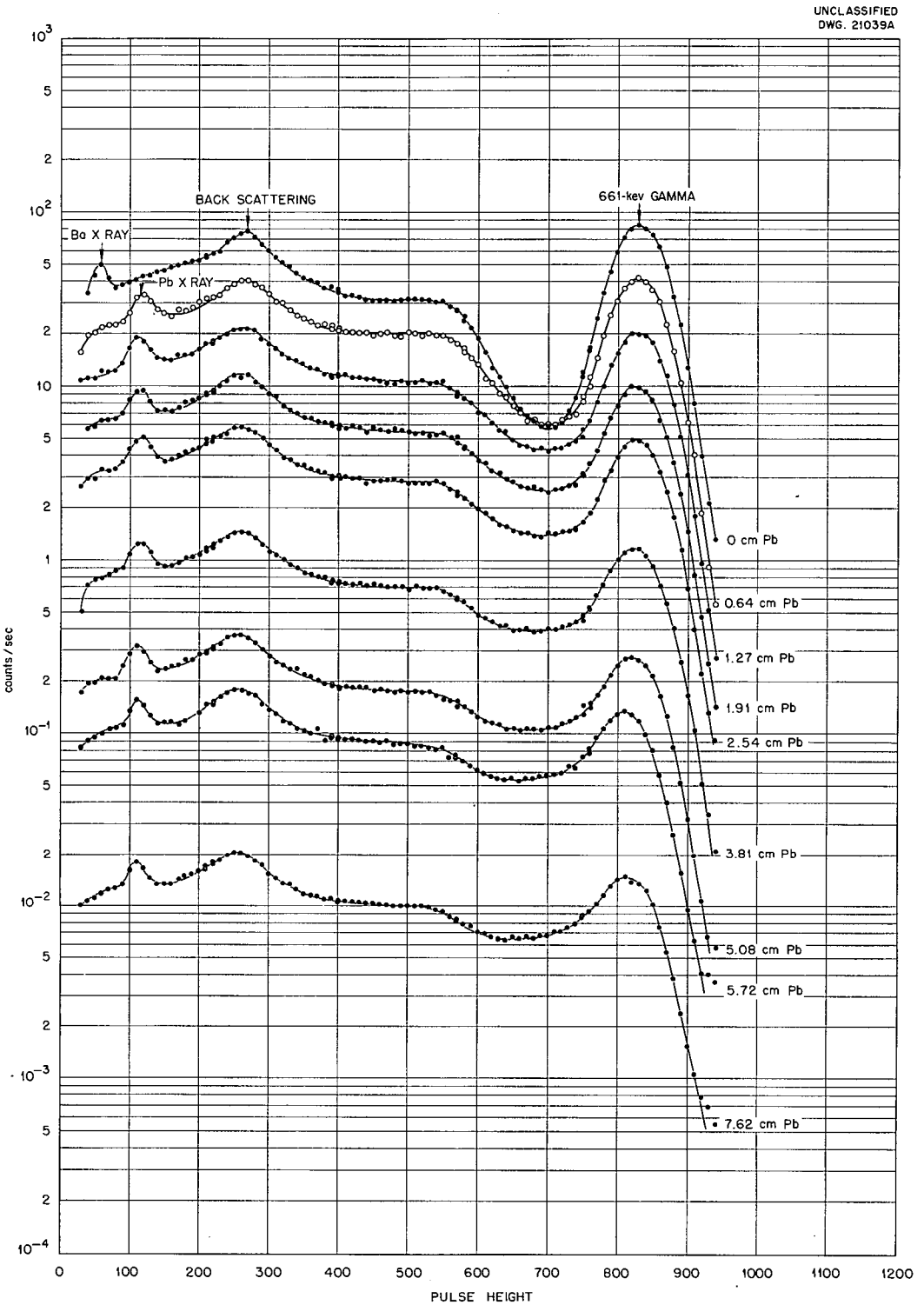


**Fig. 2.9. Broad-Beam Attenuations; $Cs^{137}$ in Lead. Source 100 cm from detector.**

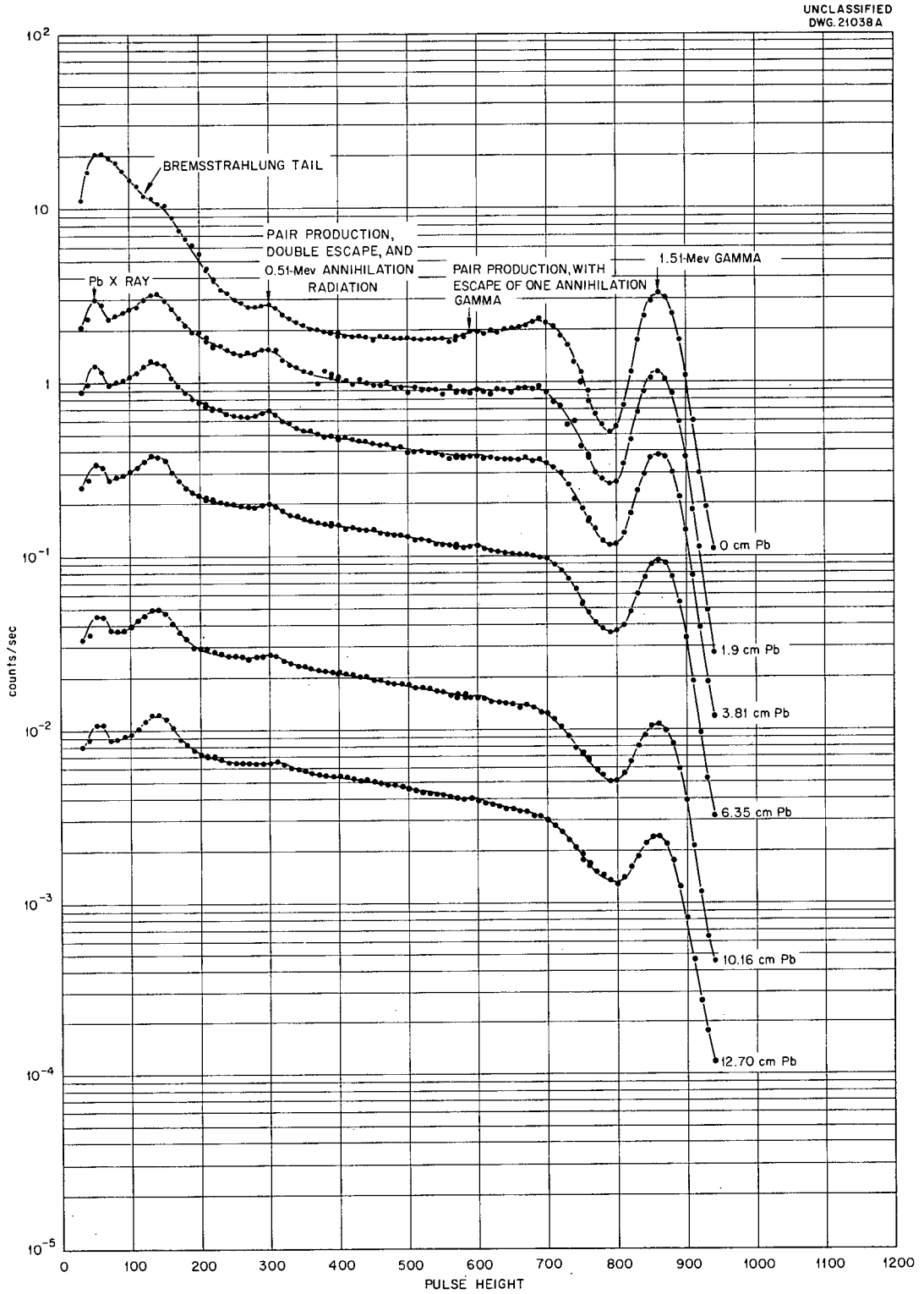


**Fig. 2.10. Broad-Beam Attenuations; $K^{42}$ in Lead. Source 100 cm from detector.**

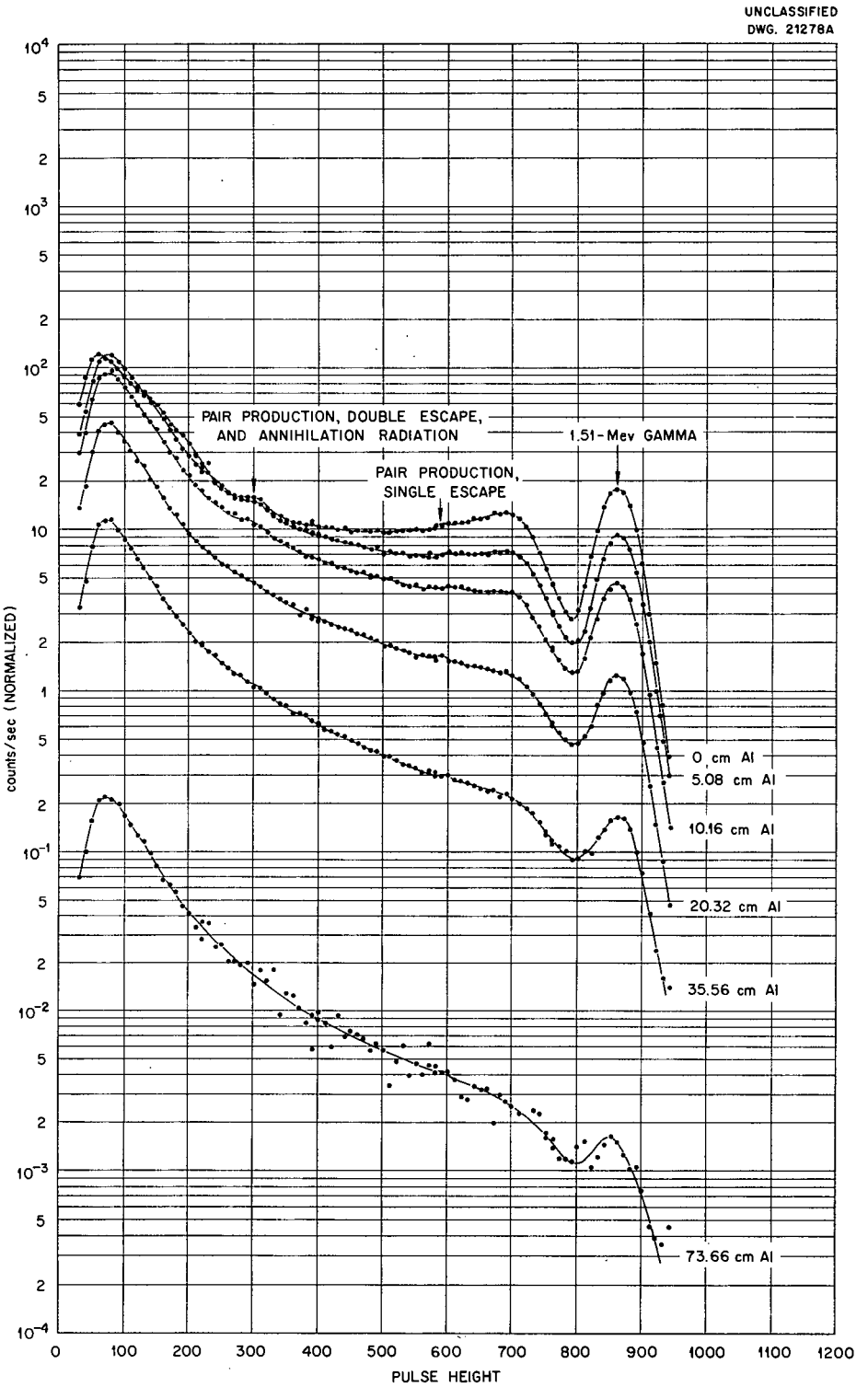


**Fig. 2.11. Broad-Beam Attenuations; $K^{42}$ in Aluminum. Source 88 cm from detector.**

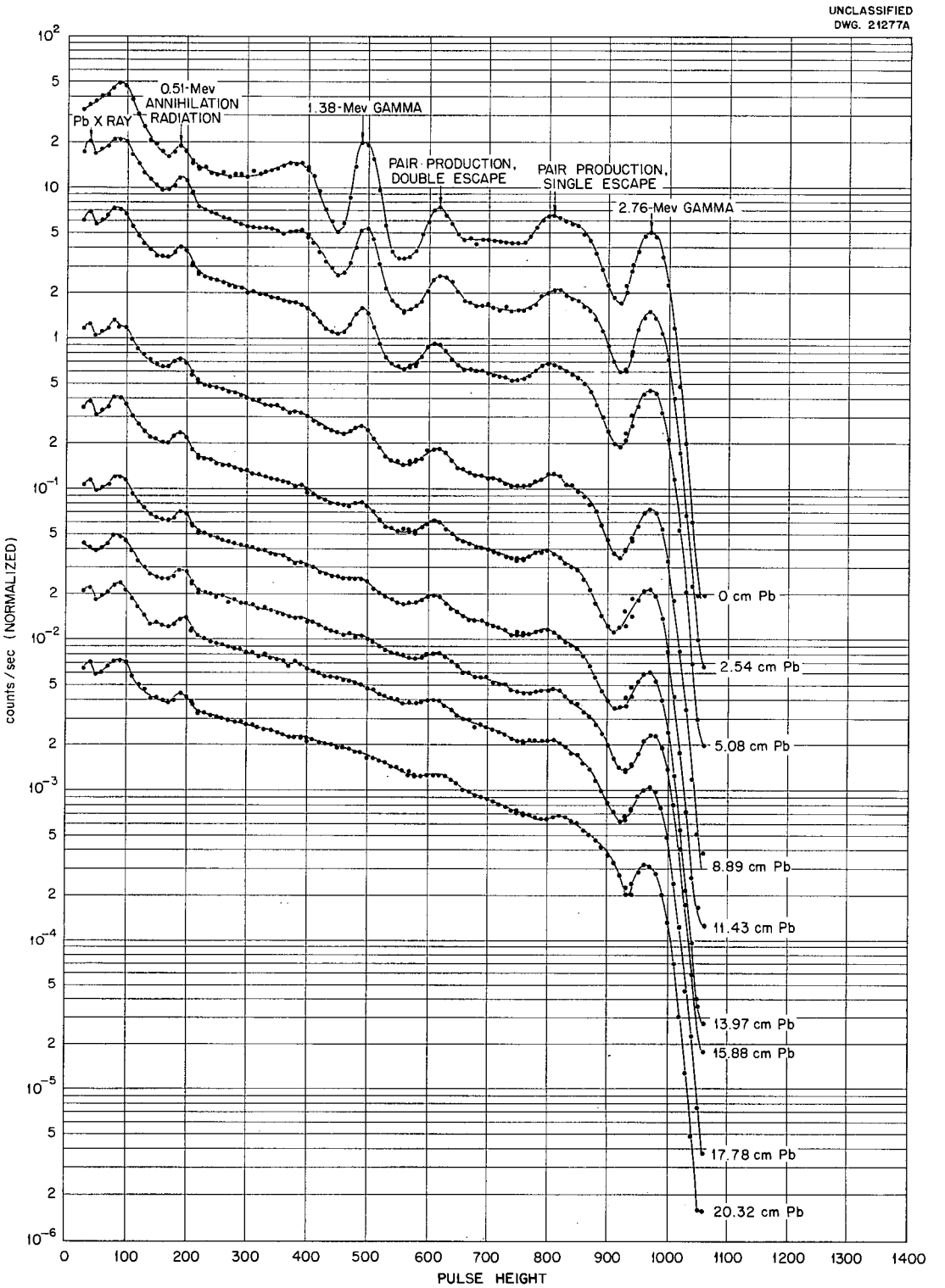


**Fig. 2.12. Broad-Beam Attenuations; $Na^{24}$ in Aluminum. Source 88 cm from detector.**

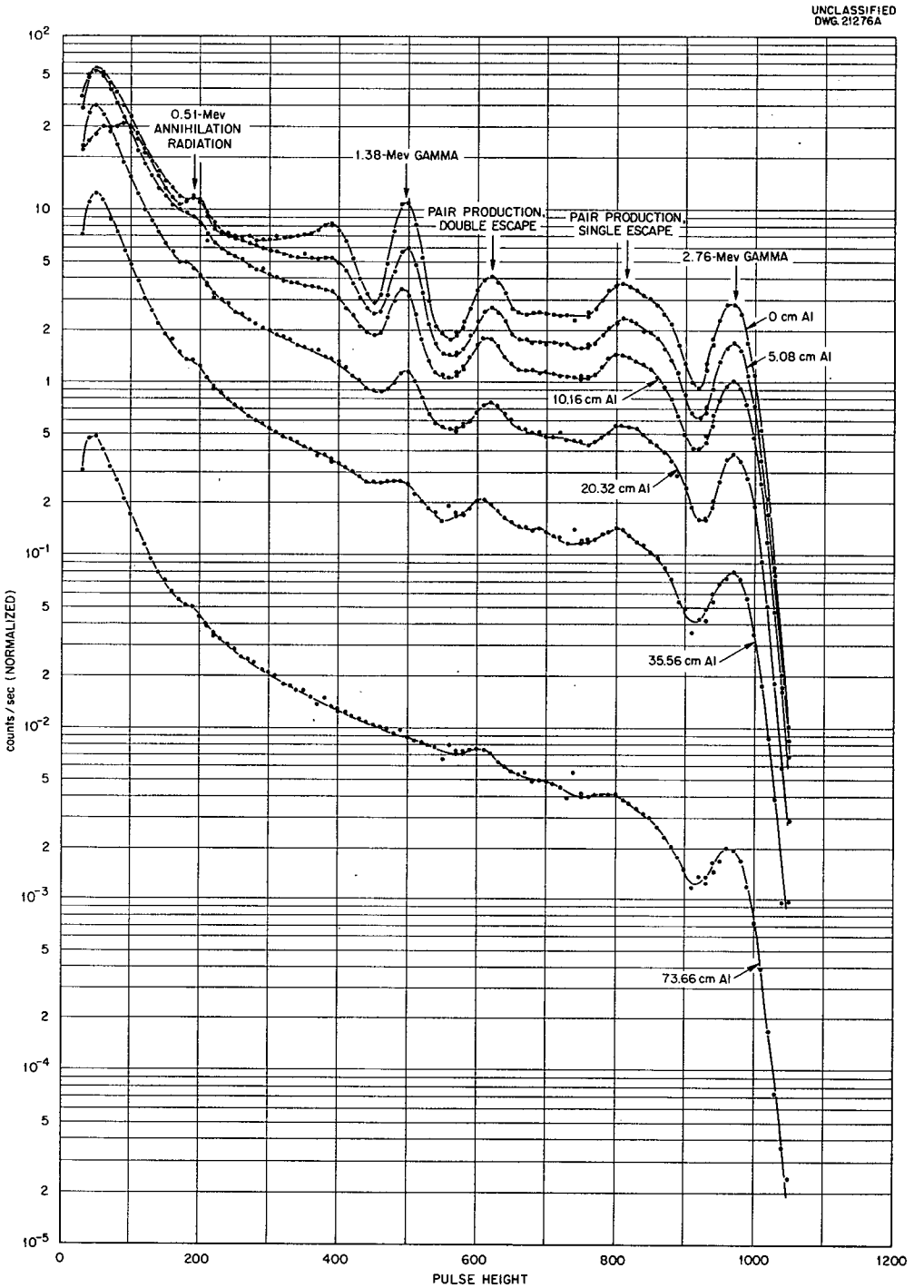


**Fig. 2.13. Broad-Beam Attenuations; $Na^{24}$ in Lead. Source 32 cm from detector.**

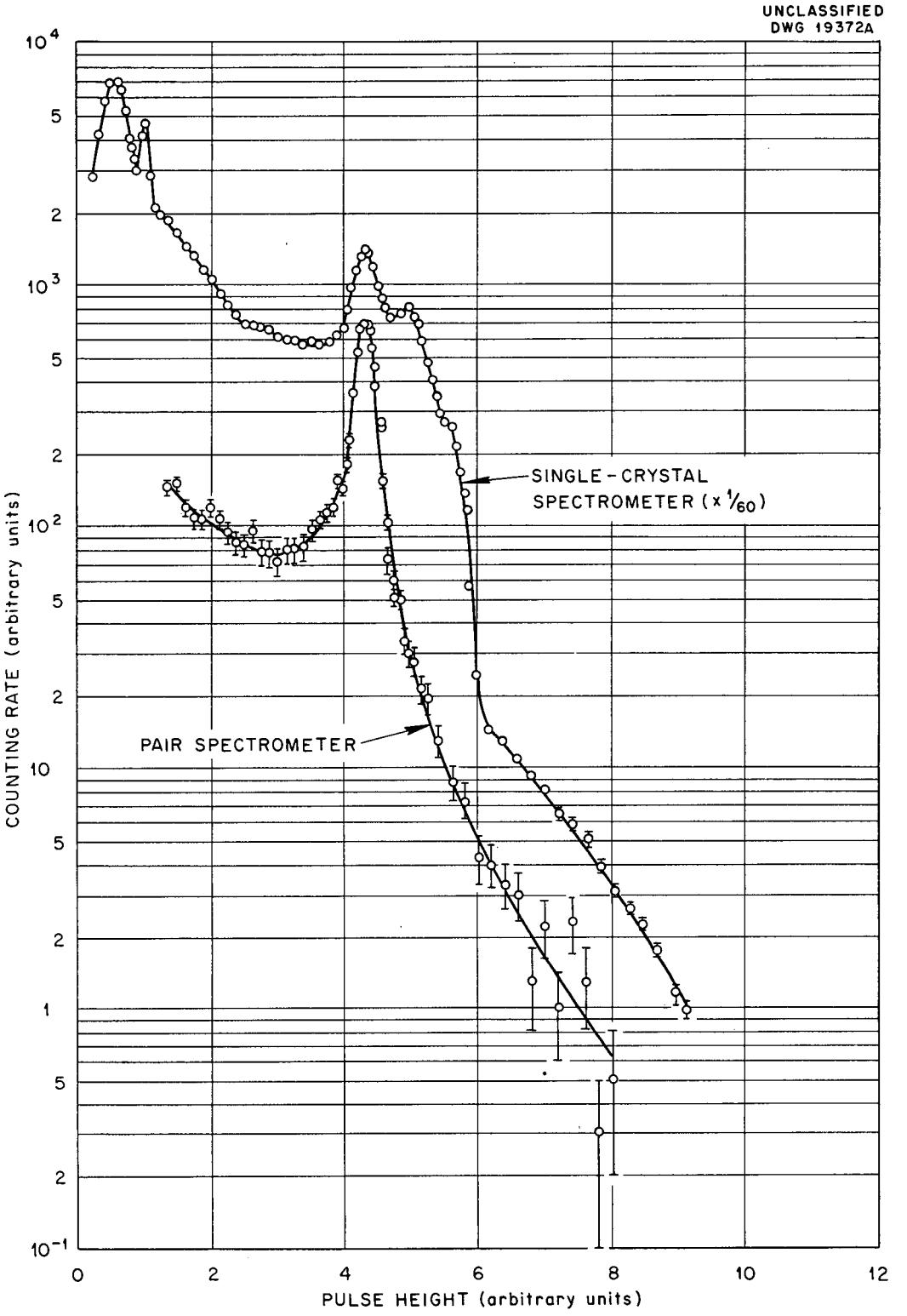


**Fig. 2.14. Gamma-Ray Spectrum Emitted by a Po-Be Source.**

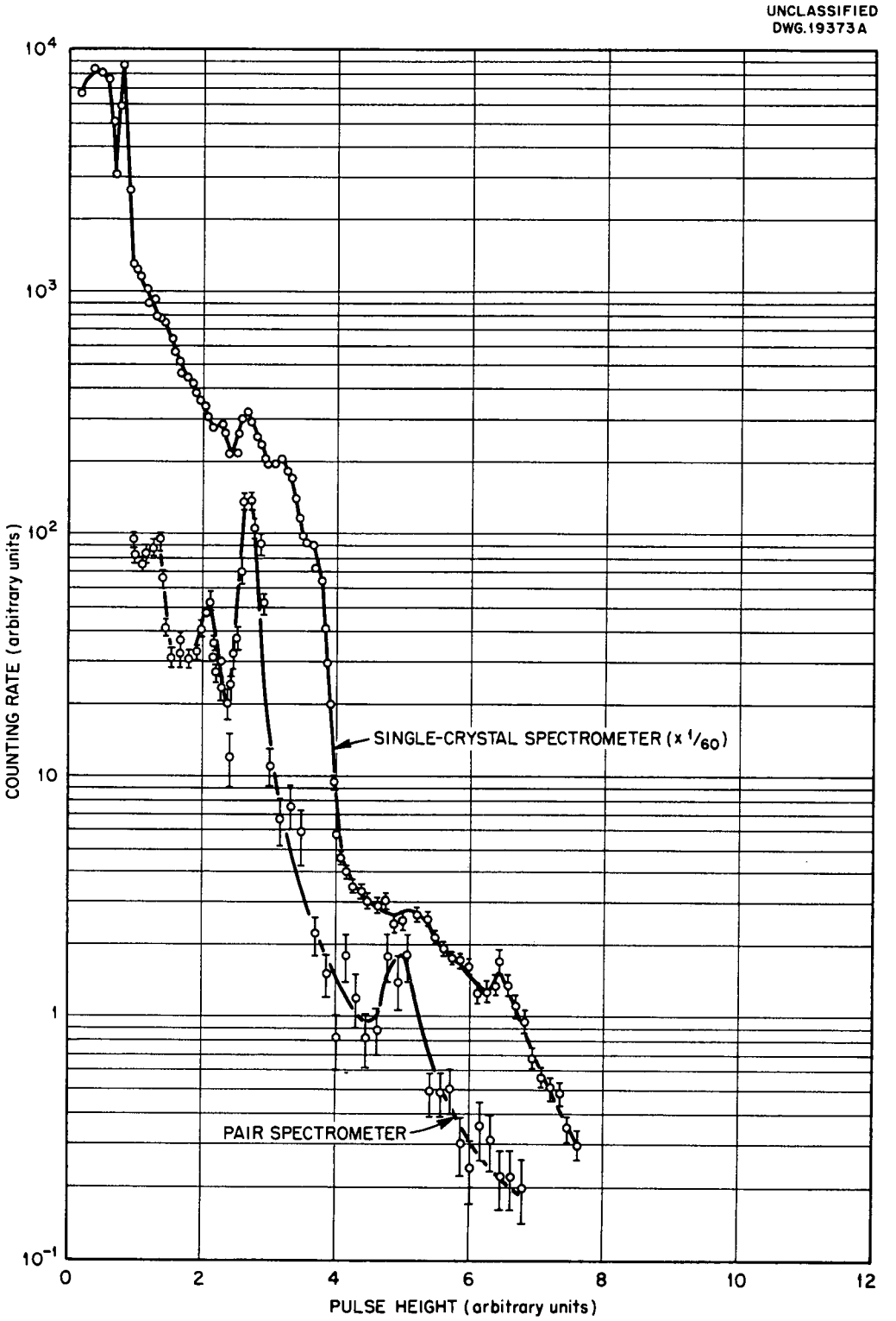


**Fig. 2.15. Gamma-Ray Spectrum Emitted by a Po B Source.**

of the spectra were investigated with the source and detector suspended in air (~8 ft to the nearest wall) in order to lower the neutron-capture gamma-ray production. A 6-in. lead shield was used to reduce the background in the low-energy regions.

Some doubt still exists concerning the production of a 2.7-Mev gamma ray by a Po-Be source as reported by earlier investigators. The present measurements indicate, however, that the intensity of this gamma ray, if present, must be less than 10% of the intensity of the 4.43-Mev gamma ray. If the energy of the prominent gamma ray in Fig. 2.14 (4.4 pulse-height units) is taken as 4.43 Mev, it can be used as a reference to determine the energies of the gamma rays emitted by a Po-B source, with results as shown in Table 2.4. The approximate relative intensities of the Po-B gamma rays, in comparison with those from Po-Be, were obtained by determining the relative amounts of polonium present. The polonium content was determined from the intensity of the 0.803-Mev polonium nuclear gamma ray as seen by the single-crystal spectrometer. The relative intensities of the gamma rays from the Po-B source are based on the known variation of the pair-spectrometer sensitivity with incident gamma-ray energy.[5] The energy levels in the residual nuclei as determined from other reactions, in addition to the measured energies and intensities, are listed in Table 2.4.

TABLE 2.4. ENERGY LEVELS AND RELATIVE INTENSITIES OF GAMMA RAYS FROM Po-Be AND Po-B SOURCES

| SOURCE | KNOWN ENERGY LEVEL (Mev) | MEASURED ENERGY LEVEL (Mev) | RELATIVE INTENSITY |
|---|---|---|---|
| Po-Be | | 2.7* | <20 |
| | 4.43 (in $C^{12}$) | 4.43** | ~220 |
| Po-B | 2.31 (in $N^{14}$) | 2.27 | 15 |
| | | 3.03 | 3.4 |
| | 3.558 (in $N^{13}$) | 3.59 | 15 |
| | 5.7 (in $N^{14}$) | 5.95 | 0.3 |
| | 7.69 (in $N^{14}$) | 7.7 | 0.2 |

*Reported by earlier investigators only; see W. Bothe, *Z. Physik* 100, 273 (1936), and H. Maier-Leibnitz, *Z. Physik* 101, 478 (1936).

**Reference.

# 3. NEUTRON DIFFRACTION[1]

## MAGNETIC SCATTERING STUDIES OF ERBIUM METAL IN THE TEMPERATURE RANGE OF 300 TO 4.2°K

W. C. Koehler E. O. Wollan

The previous quarterly report[2] included a preliminary account of neutron-diffraction experiments on the rare earth metals, and it presented some qualitative conclusions that concern the magnetic properties of metallic erbium. During the past six months, the apparatus has been modified and the measurements have been repeated at a number of stable temperatures and with much improved resolution. The data obtained may be grouped into three temperature regions for convenience of discussion: room temperature to 80°K, 80 to 35°K, and 35 to 4.2°K.

At room temperature, the neutron pattern is characteristic of a paramagnetic material. The magnetic scattering is incoherent and makes an angularly dependent contribution to the diffuse scattering. The magnitude of the magnetic scattering in the forward direction and the variation of the paramagnetic scattering with scattering angle are in close agreement with the corresponding characteristics of the scattering from $Er_2O_3$. This suggests that at room temperature erbium metal has 11 electrons (three vacancies) in the 4-*f* shell which are relatively unaffected by neighboring atoms. The nuclear reflections from metallic erbium are superimposed upon the paramagnetic scattering background and may be indexed on the simple hexagonal close-packed lattice.

[1]The authors gratefully acknowledge the assistance of Thelma Arnette in making computations and in the preparation of data.

[2]W. C. Koehler and E. O. Wollan, *Phys. Quar. Prog. Rep. Dec. 20, 1952*, ORNL-1496, p. 12.

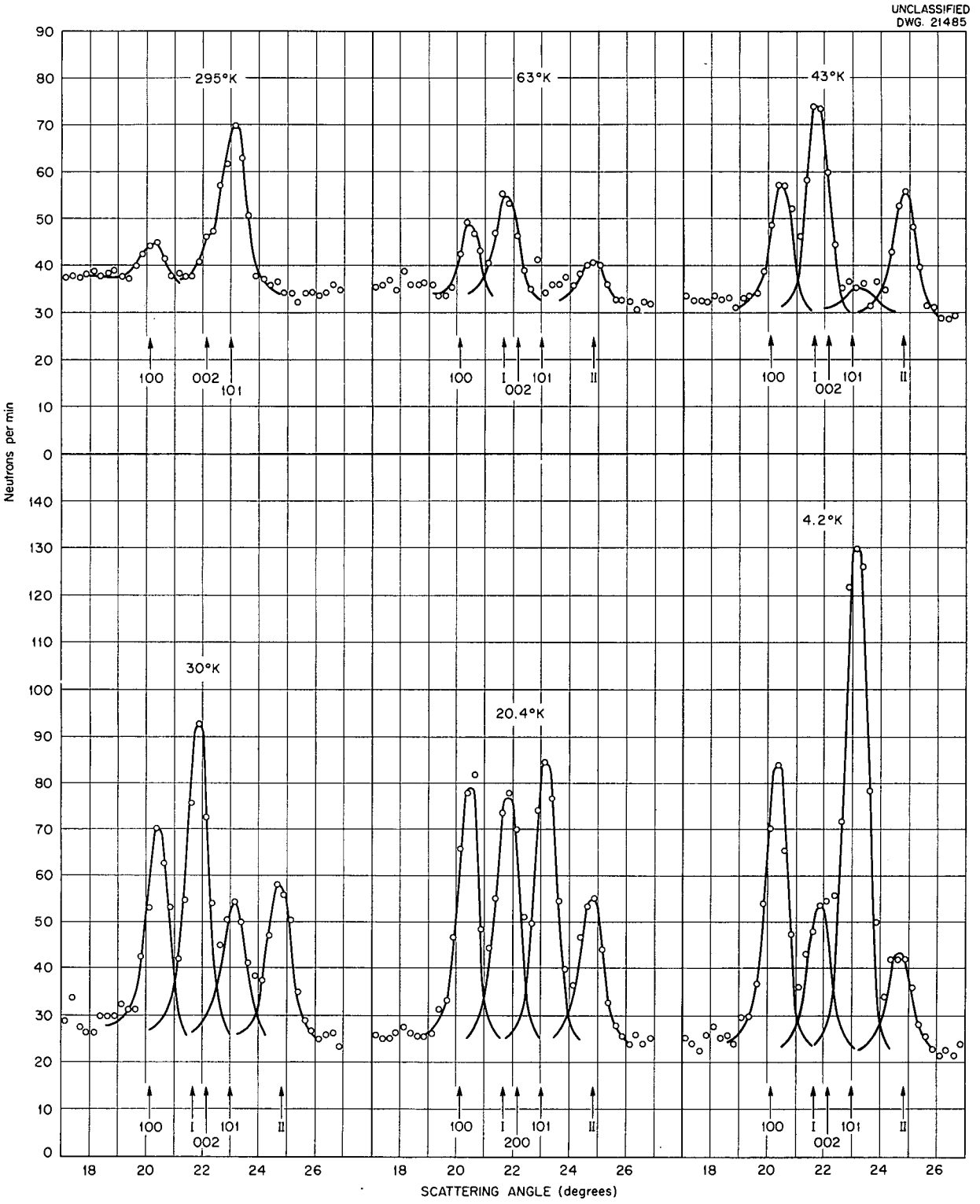


**Fig. 3.1. Diffraction Patterns for Erbium Metal as a Function of Temperature.**

At temperatures below about 80°K, some additional coherent intensities are observed, and the temperature dependence of the additional lines is somewhat complex. Portions of the higher resolution diffraction patterns, from which the temperature-corrected coherent nuclear part of the room-temperature pattern has been subtracted, are shown in Fig. 3.1.

These patterns thus display additional coherent intensities which are developed as the temperature is reduced. Two lines, which are indicated on the patterns as I and II, occur at positions which are forbidden to the simple hexagonal close-packed lattice; the indices given refer to this lattice. The temperature dependence of the several lines shown is illustrated in Fig. 3.2, in which are plotted values of $j|F|^2$ expressed on an absolute scale by quantitative comparison with the room-temperature pattern. No change of intensity is noted above 35°K for the (101) and (102) reflections; below this temperature, the experimental points lie fairly well

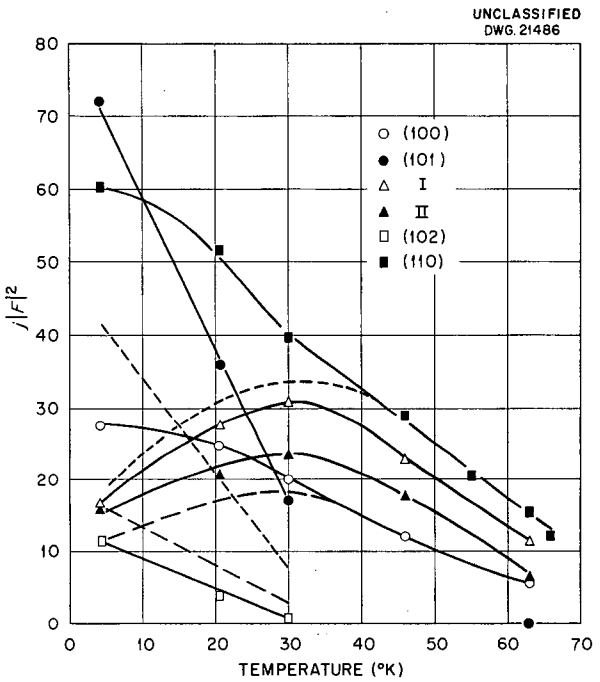


**Fig. 3.2. Temperature Dependence of the Magnetic Coherent Scattering by Erbium Metal.** The low-temperature ferromagnetic transition is shown by the (101) and (102) reflections. The dashed and dotted lines indicate how the (100) and (110) reflections may be resolved into a mixture of the low- and high-temperature magnetic phase.

on a straight line that shows no tendency to curve toward the temperature axis, even at 4.2°K. The lines at the (100) and (110) positions and the extra lines I and II, on the contrary, exhibit a pronounced growth in intensity, even at 77°K. For the extra lines, which are well resolved so that the temperature dependence is unambiguous, it can be noted that the intensities of these lines begin to decrease at about 35°K, although a measurable contribution at the lowest temperature can still be observed. For the (100) and (110) lines, however, the intensities continue to increase, although there is a definite curvature of the lines at the lowest temperatures.

A study of these data suggests that a magnetic transition, the detailed nature of which is as yet unknown, sets in at about 80°K and that this phase contributes intensity to the (100) and (110) positions, as well as to those denoted by I and II. At 35°K, a second magnetic transition occurs, for which intensity is contributed to the (101) and (102) positions, as well as to the (100) and (110) reflections. The shapes of the latter two curves in the low temperature region are attributed to the competition between the two phases.

At the lowest temperature, 4.2°K, where the contribution of the high-temperature phase is the smallest, the diffraction pattern is characteristic of a ferromagnetic material which has the same structure (simple hexagonal close-packed) as that of the chemical cell and for which the moments are directed along the hexagonal axis.

If the extrapolated $j|F|^2$ obtained from the (101) and (102) reflections, which are presumably uncontaminated by the upper temperature phase, are used to calculate the expected contribution from the ferromagnetic phase to the (100) and (110) reflections and if it is assumed that there is a linear temperature dependence, then the dashed lines in the figure that fall off at temperatures below 35°K may represent the behavior of the residual high-temperature phase contribution to those reflections.

Some correlations of these considerations with other experiments may be given.

1. The resistivity-vs.-temperature curve for erbium shows a break at about 80°K, and it was because of these measurements that Spedding suggested a ferromagnetic phase in erbium.

2. Magnetization measurements have also been carried out at Ames Laboratory, and it has been found that the metal undergoes a ferromagnetic

transition at about 35°K. There is also a suggestion of an antiferromagnetic region with a Néel point in the neighborhood of 80°K. The value for the magnetic moment, which has been deduced from the magnetization curves at 20.4°K, is 8.0 Bohr magnetons, and this value is not inconsistent with the diffraction data.

The diffuse scattering level of the patterns decreases with increasing temperature, as may be seen by inspection of the data of Fig. 3.1, although even at 4.2°K there is still a small but noticeable angular dependence to the diffuse scattering. A temperatures above 35°K, there is a suggestion of ferromagnetic short-range order.

It has not been possible with the present data to arrive at a unique interpretation of all aspects of the problem. Further experiments in which the sample is to be placed in a magnetic field are being planned for the near future.

### MAGNETIC STRUCTURE OF $Mn_2Sb$

N. S. Gingrich[3] M. K. Wilkinson
C. G. Shull

Further work has been done on the determination of the magnetic structure existing in the ferromagnetic compound, $Mn_2Sb$. This material is thought to be a *ferrimagnetic* substance in which the two manganese atoms possess different magnetic moments that are coupled in an antiparallel fashion. In an earlier study, a considerable discrepancy existed between the observed neutron-diffraction intensities and those calculated on the basis of the suspected model. Part of this discrepancy has now been accounted for by a redetermination of the structural parameters that describe the atomic positions in the crystal structure. The older x-ray data in the literature were found to be considerably in error. Use of the improved structural parameters has still not resulted in satisfactory agreement, and a start has been made on a single-crystal analysis of the magnetic structure.

### MAGNETIC DISORDER SCATTERING IN IRON-CHROMIUM AND COBALT-CHROMIUM ALLOYS

C. G. Shull M. K. Wilkinson

It is known from magnetization studies that the ferromagnetism in disordered alloys of chromium added to iron or cobalt becomes weaker as additional chromium is introduced. If it is assumed that the magnetic moment of the solvent atom (iron or cobalt) is unchanged in the alloy, a study of the magnetization data suggests that the chromium moment is small or zero when chromium is added to iron and that it is very large ($5\mu_B$) and antiparallel to the cobalt moment when chromium is added to cobalt. Neutron-diffraction studies offer the possibility of determining the individual atomic moments rather than the average moment in the alloy, as is seen in magnetization studies. A series of alloys of varying composition was examined by the neutron-diffraction technique.

All the alloys were studied in the disordered state, that is, the structure in which there exists a random distribution of solute atoms at solvent atom sites, and the magnetic scattering appeared as a disorder scattering that was superimposed on the normal diffuse scattering in the neutron-diffraction pattern. This magnetic disorder scattering was determined as the difference between the diffuse scattering level when the sample was unmagnetized and the level when the sample was magnetized in a direction parallel to the scattering vector. In the latter case, all the magnetic scattering should disappear. The disorder scattering, when placed on an absolute scale by suitable normalization, is given by the expression

$$p^2 = 0.0484\, g_1 g_2 (\mu_1 - \mu_2)^2 \cdot 10^{-24} \quad \text{cm}^2/\text{average atom},$$

where $g_1$ and $g_2$ are the fractional abundances of the two types of atoms and $\mu_1$ and $\mu_2$ are their magnetic moments expressed in Bohr magnetons. Thus the diffuse scattering analysis permits the determination of the difference between the two atomic moments. A combination of this difference with the magnetization data, which give the weighted sum of the atomic moments, allows the evaluation of the individual moments. There are, however, alternative solutions for the moments because of the quadratic nature of the above equation, and the experiment does not make it possible to resolve this ambiguity. Independent arguments must therefore be used.

The atomic magnetic moments found in the Fe-Cr and the Co-Cr series of alloys are summarized in Figs. 3.3 and 3.4. In both figures, the alternative sets of values are shown by the solid lines and by the dashed lines. For both series of alloys, the

[3] Summer Participant, University of Missouri, Columbia, Missouri.

moment of the solvent atom decreases as the solute concentration increases, and the solute atomic moment is either small or very large and parallel to the solvent atomic moment. It is to be noted that the addition of chromium to cobalt cannot result in an antiferromagnetic arrangement of moments because all the moments possess the same sign. Such an antiparallel alignment of moments in Co-Cr, as mentioned earlier in this section, would have produced a very much larger disorder scattering than was observed. No detailed conclusions concerning the variation of atomic moments with alloy concentration, as shown in the figures, can be given at this time.

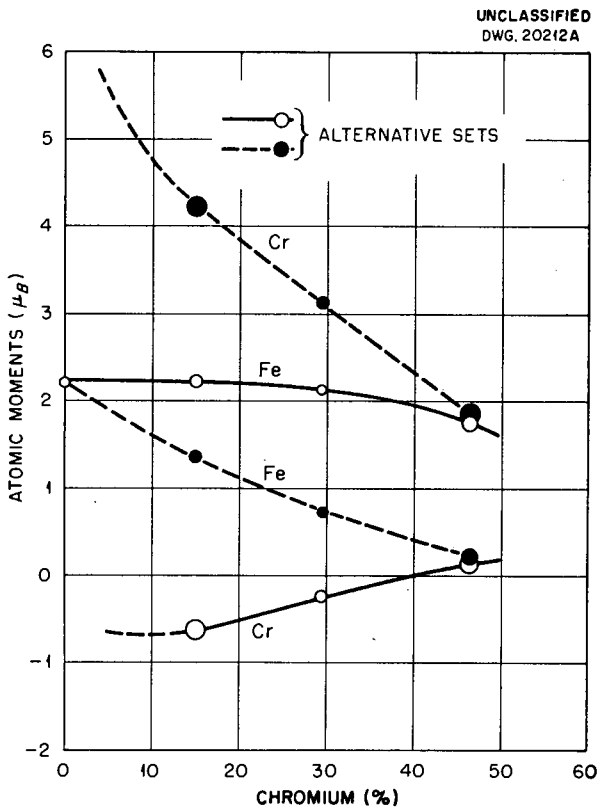


**Fig. 3.3. Atomic Magnetic Moments Existing in the Fe-Cr Series of Alloys.** The size of the experimental points is a measure of their precision. Experiment is unable to select from the alternative sets.

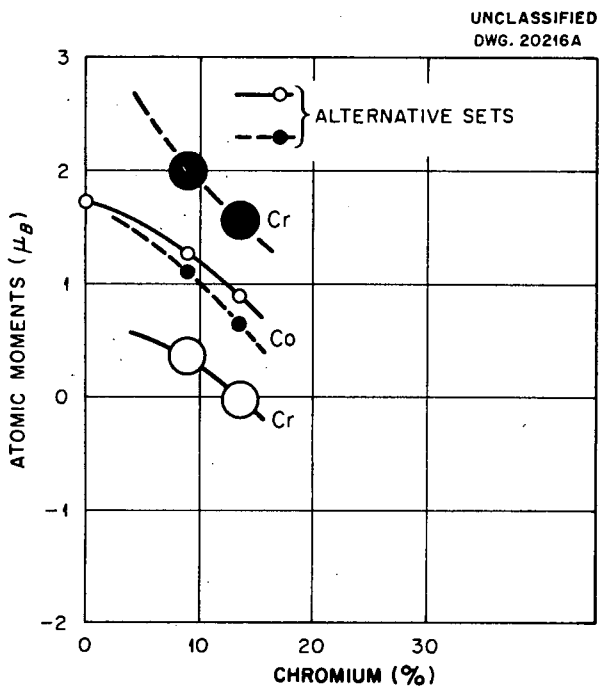


**Fig. 3.4. Atomic Magnetic Moments Existing in the Co-Cr Series of Alloys.** The size of the experimental points is a measure of their precision. Experiment is unable to select from the alternative sets.

# 4. LOW TEMPERATURES AND NUCLEAR POLARIZATION

## CAPTURE OF POLARIZED NEUTRONS BY POLARIZED MANGANESE NUCLEI

S. Bernstein C. P. Stanford
L. D. Roberts J. W. T. Dabbs
T. E. Stephenson

An attempt was made to observe directly the dependence of the capture cross section of polarized $Mn^{55}$ nuclei for polarized neutrons upon the relative orientation of incident and bombarded particles. The target material was the paramagnetic substance, manganous ammonium sulfate, which is known to have a large hyperfine structure coupling. The compound was placed in a magnetic field of 2350 oersteds at a temperature of 0.201°K. Under these conditions, the polarization of the paramagnetic electrons is about 85%. Because of the large magnetic field created by the polarized paramagnetic electrons at the manganese nucleus, the nuclei should achieve a polarization of 16%. The 2.6-hr activity of the residual nucleus, $Mn^{56}$, was measured after the sample had been bombarded with a beam of slow neutrons, polarized to the extent of 32% by passage through magnetized iron. The activity for neutron-polarizing field and sample-polarizing field parallel was found to be 3.4% less than that for the fields antiparallel. The difference in the two activities was found to depend upon the sample temperature in accordance with theory. The difference was found to be unaccompanied by a corresponding change in sample transmission. These results are interpreted to mean that the change in sample activity was due to the dependence of the capture cross section of the polarized manganese nuclei upon the relative orientation of the polarized neutrons. A report of this work is being sent to the *Physical Review*.

## INTERACTION OF POLARIZED NEUTRONS WITH POLARIZED $Sm^{149}$ NUCLEI

L. D. Roberts J. W. T. Dabbs
S. Bernstein C. P. Stanford
T. E. Stephenson

Preliminary experiments have been made on the polarization of $Sm^{149}$. In these experiments, the transmission of neutrons at 0.075 ev has been observed as a function of relative spin orientation of the nuclei and neutrons. A maximum single-transmission effect of approximately 4% and a maximum net double-transmission effect of approximately 19% were observed. These changes in transmission are interpreted as being due to the spin dependence of the capture cross section.

**Polarization of Samarium Nuclei.** The paramagnetic salt $Sm(C_2H_5SO_4)_3 \cdot 9H_2O$ is characterized in the powder form by an average hfs coupling of 0.0153 $cm^{-1}$. By cooling to a temperature of approximately 0.05°K and by applying a field of a few kilogauss, a nuclear polarization of $Sm^{149}$ of approximately 30% may be obtained. This type of experiment was performed in which

$$Fe(NH_4)_2(SO_4)_2 \cdot 6H_2O$$

was used as a coolant and a metal connecting bar was employed. Heat contact was made by pressing 12 g of the iron salt into a silver cup located at the lower end of the 5-in.-long bar and by pressing the samarium salt into a flat plate geometry of copper (salt thickness 0.058 in.) at the upper end of the bar. After demagnetization of the iron salt from 15.4 kilogauss and 1.2°K, the sample tube that contained this assembly was lowered to such a position that the iron salt was inside a magnetic shield at approximately 0 gauss. A field of approximately 5 kilogauss was then applied to the upper samarium salt sample by means of the same Weiss magnet that was used in the demagnetization. As the heat of magnetization of the samarium salt was conducted to the iron salt, the samarium nuclei became polarized. The relaxation time for this process was reasonably short.

**Detection of Polarization.** A thermal-neutron beam from the graphite reactor was allowed to fall on the samarium salt sample, and the transmitted beam was reflected from the 220 planes of a magnetized single crystal of $Fe_3O_4$. These neutrons were counted with a $BF_3$ long counter. The magnetite crystal and counter were set at angles that satisfied the first-order Bragg condition corresponding to 0.075 ev. This energy lies near the peak of the lowest resonance (16,000 b at 0.094 ev) in $Sm^{149}$, and it also permits the use of suitable filters in the beam to reduce higher order neutron intensities. Thus the samarium salt sample served as a neutron polarizer when the samarium nuclei were polarized, and the magnetite crystal served as an energy selector and analyzer.

Counting rates were obtained as follows: (*a*) in this arrangement; (*b*) with a thin unmagnetized sheet of polycrystalline iron in the beam; the iron served to depolarize the beam after transmission through the samarium sample, and (c) with the $Sm^{149}$ nuclei unpolarized. In obtaining rates of the types (*a*) and (c), the thin iron sheet was located in the beam between the reactor and the samarium sample; thus the effect of its small attenuation of the beam in (*b*) was canceled.

These rates were obtained as a function of time after the demagnetization and application of the nuclear polarizing field. The counting rate (*a*) was observed to go through a minimum which was approximately 12% lower than that of (c) about 1 hr after the application of the field, while (*b*) was observed to go through a maximum about 4% higher than (c) at about the same time. Both effects decreased as the sample temperature increased, as was to have been expected.

Examples of the observed rates were:

| | Counts/Minute |
|---|---|
| Background | 137 ± 4 |
| Background + samarium, unpolarized (c) | 609 ± 4 |
| Background + samarium, iron shim in (*b*) | 624 ± 8 |
| Background + samarium, shim out (*a*) | 551 ± 5 |

Within experimental accuracy, these results are consistent with the present knowledge of the temperatures, higher order content of the neutron beam, and neutron polarization by the magnetite.

## MEASUREMENT AND CALCULATION OF THE LIQUID-HELIUM VAPOR PRESSURE-TEMPERATURE SCALE FROM 1 TO 4.2°K

R. A. Erickson L. D. Roberts

Measurements that were made between 1.2 and 4.2°K on a paramagnetic salt and that employed a mutual inductance bridge apparatus indicate that there are errors in the presently accepted liquid-helium temperature scale. The errors amount to 12 millidegrees at the λ-point. These data, together with those of Kistemaker, are found to be in good agreement with a temperature scale that was calculated from the other thermodynamic properties of helium. The calculated scale is further confirmed by a comparison between the calculated and the observed latent heat of vaporization. If the boiling-point determination of Keesom and Clusius is accepted as correct, the estimated accuracy of the proposed temperature scale is 1.5 millidegrees at temperatures below the λ-point and 3 millidegrees above the λ-point.

The results are shown in Fig. 4.1. A paper describing this work is being submitted for publication in the *Physical Review*.

## SUSCEPTIBILITY STUDIES OF THE ANTIFERROMAGNETISM IN $MnCl_2$ AND $UI_3$

L. D. Roberts R. A. Erickson

Preliminary studies of the magnetic susceptibility of powdered samples of anhydrous $MnCl_2$ and $UI_3$ indicate these compounds to be antiferromagnetic. The results for $MnCl_2$ are given in Fig. 4.2, and they show that at the higher temperatures the susceptibility follows a Curie-Weiss law with a Weiss constant of 4.35°K (antiferromagnetic). The indicated Néel temperature is at 2.2°K, below which the material is presumed to be antiferromagnetic. The single-crystal susceptibilities, as functions of magnetic field and temperature, are being studied on a spherical sample cut from a single-crystal specimen that was prepared by J. Schenck.

The low-temperature differential susceptibility of $UI_3$ is shown in Fig. 4.3. The susceptibility

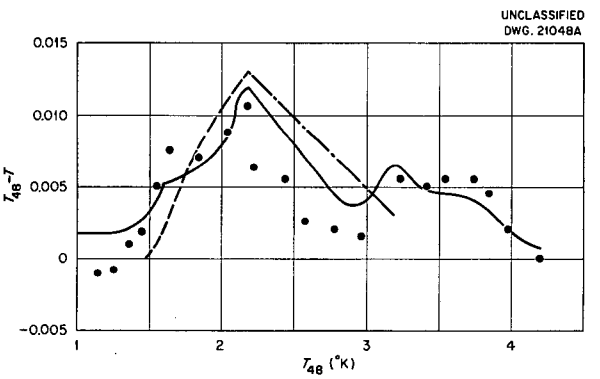


**Fig. 4.1. Corrections to the 1948 Liquid-Nitrogen Temperature Scale.** The points represent measured deviations from the 1948 scale, the solid curve gives the present calculated result, and the broken line represents the correction consistent with the measurements of Kistamaker [*Physica* **12**, 272, 281 (1946)] and of Abraham, Osborne, and Weinstock [*Phys. Rev.* **80**, 366 (1950)].

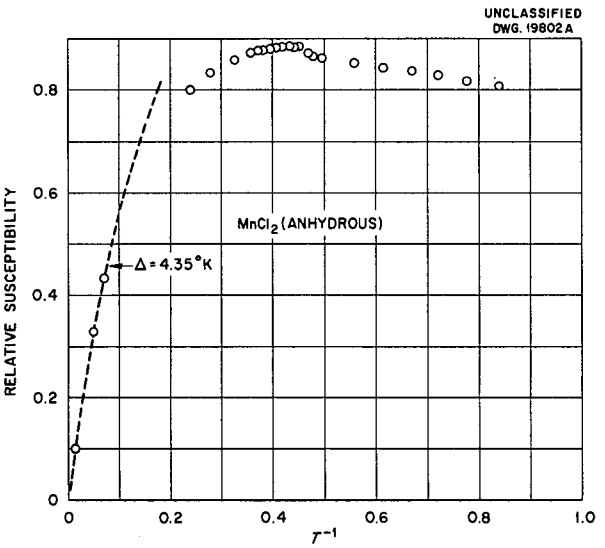


**Fig. 4.2. Magnetic Susceptibility of Anhydrous Manganous Chloride as a Function of Reciprocal Temperature.**

maximum at 3.2°K is interpreted as an antiferromagnetic transition. In this region, the imaginary component of the complex susceptibility (the loss component) remains at its residual low level. The peak at 1.5°K in the real susceptibility is quite different from that at the Néel temperature. In this region, the loss component rises sharply to a maximum at 1.37°K, and both components of susceptibility are quite sensitive to the bias magnetic field, which is applied through a solenoid coil mounted coaxially to the susceptibility-measuring coils. The phenomena associated with the second susceptibility maximum are presumed to be intrinsic properties of $UI_3$, since they have been observed in two different preparations of this compound. The observations are tentatively accounted for by assuming that, while the bulk of the material develops an antiferromagnetic ordering below 3.2°K, some of the atoms (~1 in $10^5$) cooperate in forming a ferromagnetic lattice that has a Curie temperature of about 1.5°K. In some respects, this phenomenon is

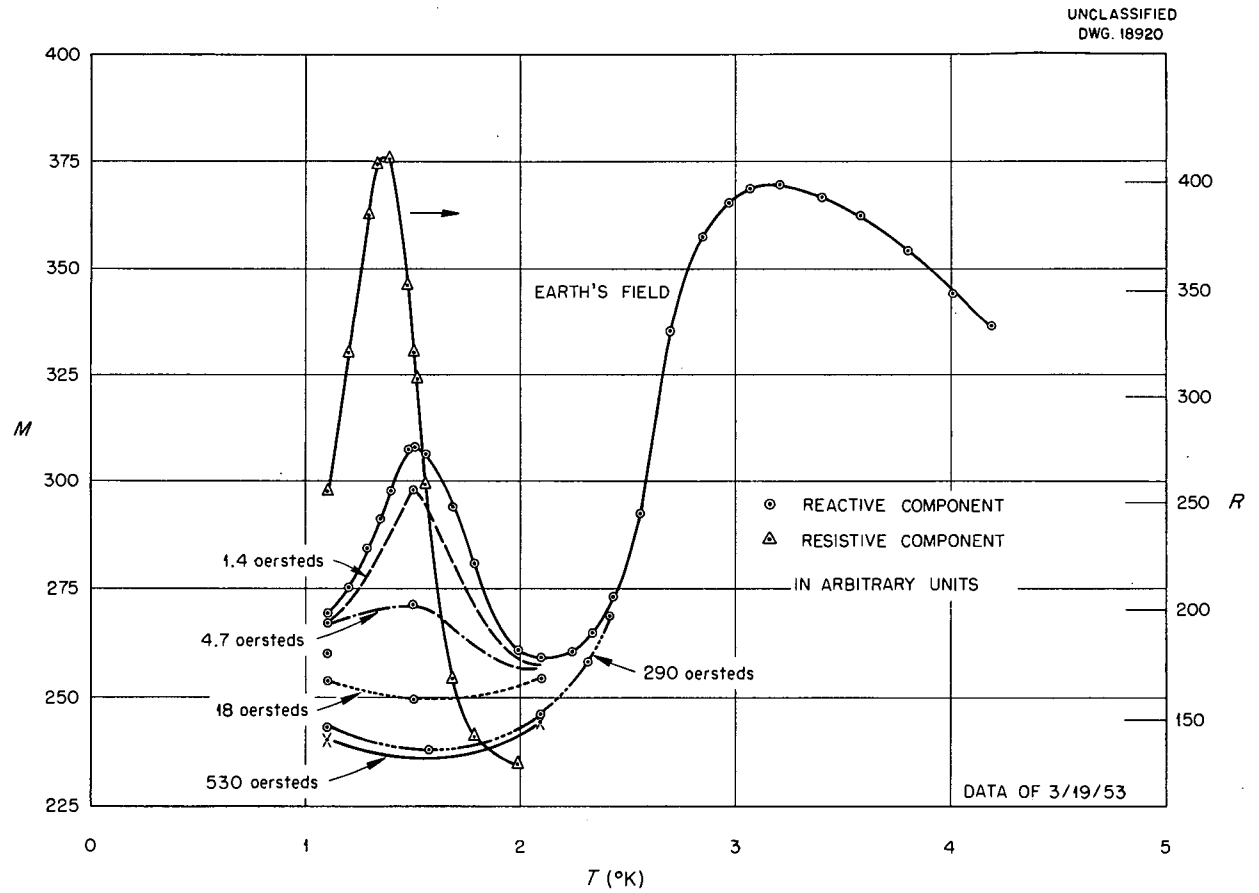


**Fig. 4.3. Magnetic Susceptibility vs. Temperature for $UI_3$ for Magnetic Fields in the Range 0 to 530. oersted.**

similar to the ferromagnetic effects found by Kurti and Simon in iron ammonium alum near 0.04°K.

### HEAT CAPACITY MEASUREMENTS

R. B. Murray

A new cryostat has been designed and constructed for the purpose of heat capacity measurements in the temperature range 1 to 20°K. This cryostat is being used to determine the heat capacities of anhydrous $MnCl_2$ and $UI_3$, both of which become antiferromagnetic near 2°K. Heat capacity measurements are carried out by cooling the sample to 1°K by means of thermal contact with a bath of liquid helium that is boiling under reduced pressure, thermally isolating the sample from its surroundings, and then observing the small change in temperature of the sample as it is heated. Heating is accomplished by passing current through a coil wrapped on the sample; the sample temperature is determined by the resistance of a carbon radio resistor that is embedded in the sample.

### MUTUAL INDUCTANCE BRIDGE AND CRYOSTAT FOR LOW TEMPERATURE MAGNETIC MEASUREMENTS

R. A. Erickson L. D. Roberts

The conventional apparatus for measuring magnetic susceptibility employs either a magnetic balance, for temperatures above 4°K, or a mutual inductance apparatus for temperatures obtained with liquid helium or by adiabatic demagnetization. A mutual inductance bridge and a cryostat that are capable of measuring susceptibilities from 77°K down to adiabatic demagnetization temperatures have been put into operation. The precision of measurement of the relative susceptibility of a 12-mm spherical sample is about $10^{-6}$ cgs. In addition, the apparatus provides the following features: a usable frequency range of 5 kilocycles for the study of paramagnetic relaxation and paramagnetic specific heat; measurement of longitudinal susceptibilities in fields up to 3000 oersteds, and transverse susceptibilities in fields up to 13,000 oersteds; and a simple method for changing samples that involves a minimum dismantling of the equipment.

A detailed report on this apparatus will be submitted for publication in the *Review of Scientific Instruments*.

### SOME THERMODYNAMIC PROPERTIES OF $Mn(ND_4)_2(SO_4)_2 \cdot 6D_2O$ BELOW 1°K

J. W. T. Dabbs L. D. Roberts

Measurements of $Mn^{55}$ nuclear polarization, in which $Mn(ND_4)_2(SO_4)_2 \cdot 6D_2O$ was employed, are described elsewhere in this report.[1] In this connection, the authors have measured the magnetic moment (Fig. 4.4) and the absolute temperature (Fig. 4.5) of the same salt as a function of final field in adiabatic demagnetizations from fields of 10 to 17 kilogauss and temperatures of approximately 1.2°K. These measurements have been carried out over a final field range $0 < H_f \leq 4560$ gauss and over a temperature range of 0.119 to 0.35°K. Gamma-ray heating was used to establish one point at 0.201°K of the $T - H$ relation, with $M$ as the "thermometric parameter," and the region was covered by using the equation

$$T_1 - T_2 = \int_{H_1}^{H_2} \left(\frac{\partial M}{\partial S}\right)_H dH \ .$$

Calibration of the gamma-ray heat input was obtained by direct comparison with a measured electrical heat input in the region 0.4 to 0.5°K. This approach has several advantages. If this measurement is made near 1°K, where the specific heat is usually well known, the background heat leak is usually quite large compared with that at the lower temperatures and compared with the specific heat of the salt. If this calibration is made at somewhat lower temperatures where the salt

[1] See *Capture of Polarized Neutrons by Polarized Manganese Nuclei* of this report.

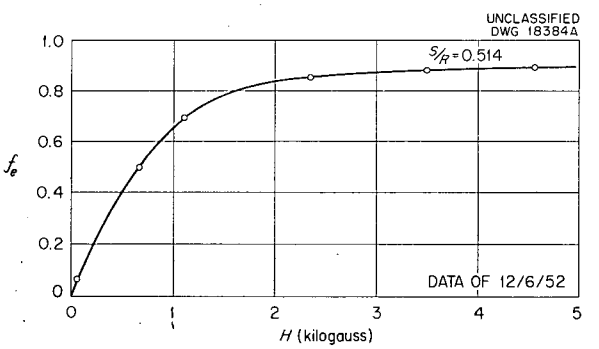


**Fig. 4.4. Magnetic Moment (Fraction of Electrons Polarized) as a Function of Final Field for S/R = 0.514 in Manganous Ammonium Sulfate.**

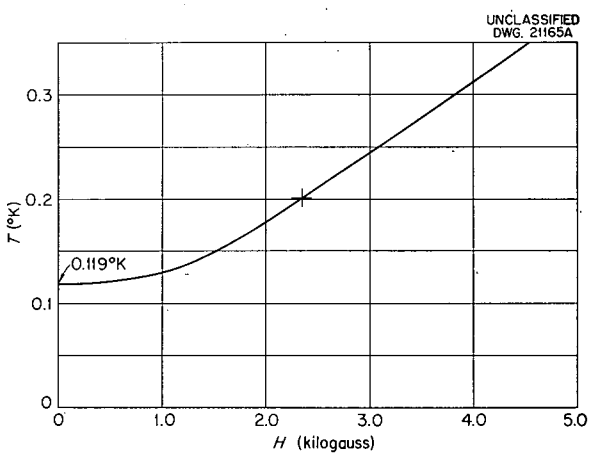


**Fig. 4.5. Absolute Temperature of Manganous Ammonium Sulfate as a Function of Final Field.** $S/R$ = 0.514.

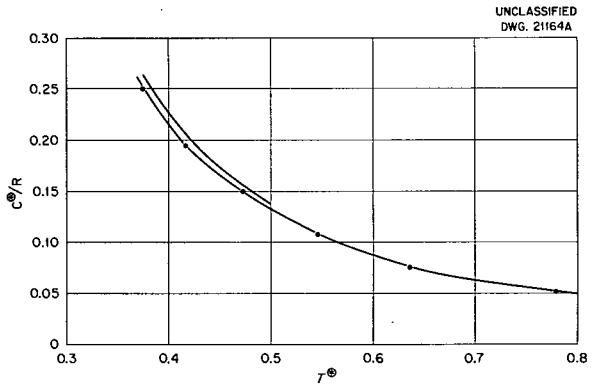


**Fig. 4.6. Specific Heat on the Magnetic Scale of Temperature as a Function of Magnetic Temperature of Manganous Ammonium Sulfate (lower curve).**

specific heat is considerably larger and the background heat leak relatively small and temperature independent, the specific heat is usually not well known. The resulting uncertainties in $dQ/dt$ have been one of the larger sources of error in the measurement of temperature below 1°K by gamma-ray heating. To reduce this error, the gamma-ray heating has been compared with a measured electrical heat input in the temperature region near 0.4°K where the thermal conductivity of the salt is adequate. At lower temperatures, electrical heating would lead to serious temperature inhomogeneities, whereas gamma-ray heating does not. At 0.4°K, the specific heat of the salt is sufficiently large compared with the "background" heat leak to permit precise measurements of susceptibility as a function of time for either heat source.

Figure 4.6 shows a curve of the specific heat,

$$C^{\circledast} = \frac{dQ}{dT^{\circledast}} ,$$

of $Mn(ND_4)_2(SO_4)_2 \cdot 6D_2O$ as a function of $T^{\circledast}$ (reciprocal susceptibility) as determined by electrical heating. For this measurement, the salt was pressed into a slitted cylindrical copper sleeve, $^5/_{16}$ in. in diameter and $^{15}/_{16}$ in. in length. A constantan wire heater was wound on the copper cylinder, and baked Araldite was used to obtain thermal contact. Heater leads that extended through the wall of the sample tube into the liquid helium were made of 1-mil lead-coated constantan wire. Heater current and potential measurements were made by means of precision potentiometers and a standard resistor. The observed magnetic temperature, $T^*$, was corrected to that for a sphere, $T^{\circledast}$, with the assumption that the sample was an ellipsoid with $c/a$ = 3. These measurements lead to a calculated gamma-ray heat input

$$\frac{dQ}{dt} = 2890 \text{ ergs/minute} .$$

It is interesting to note that the constantan heater showed a minimum of electrical resistance at about 0.5°K.

These measured values of the magnetic moment and the temperatures were used to calculate the nuclear polarization, $f_N$, as a function of $H_e$ at $S/R$ = 0.514. This result is given in the lower curve of Fig. 4.7.

## MEASUREMENT OF OPERATING TEMPERATURE IN THE COLLINS HELIUM LIQUEFIER

J. W. T. Dabbs R. B. Murray
L. D. Roberts

Greater efficiency in the operation of the Collins helium liquefier has been obtained by replacing the thermocouples that monitored the temperature of the two liquefier expansion engines with carbon resistors, which are much more sensitive at low temperatures. A resistor was also attached to the Joule-Thompson valve; thus the operator has better control over the final expansion. Temperatures at the various points in the liquefier are indicated by a current-sensitive

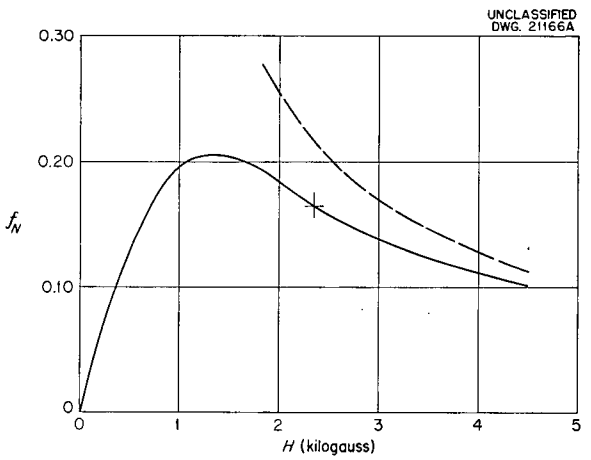


**Fig. 4.7. Nuclear Polarization of $Mn^{55}$ as a Function of Final Field (solid curve).**

circuit which responds to changes in resistance of the carbon resistors. The signals from this circuit are read directly on milliammeters by the operator, and they are also permanently recorded on a micromax recorder.

# 5. HEAVY-ION PHYSICS

## MEASUREMENT OF ELECTRON CAPTURE AND LOSS CROSS SECTIONS

P. M. Stier C. F. Barnett
G. E. Evans V. L. DiRito

As part of the general program of investigating the various processes for energy transfer from a heavy particle (fission fragment, recoil atom, etc.) to the stopping material, the Heavy-Ion Physics Group has been studying charge exchange.

The current series of experiments is designed to measure the fraction of the particle beam in each possible charge state as a function of energy, stopping gas, and incident ion species. Measurements are made at stopping gas pressures that are sufficiently high to establish equilibrium between competing capture and loss reactions (that is, the particles in the beam assume an average, pressure-independent, charge) but low enough so that the energy degradation of the beam may be neglected. Some of the capture and loss reactions which are possible when $He^+$ ions pass through argon gas are:

(1) $He^+ + A^0 \rightarrow He^0 + A^+$

(2) $He^+ + A^0 \rightarrow He^{++} + A^0 + e^-$

(3) $He^0 + A^0 \rightarrow He^+ + A^0 + e^-$

(4) $He^{++} + A^0 \rightarrow He^+ + A^+$

At equilibrium, the ratio of the number of particles in the different charge states is almost exactly the ratio of complementary cross sections for transitions between the charge states.[1] Thus the ratio of helium atoms to ions in the above example is the ratio of the cross sections for the reactions (1) and (3).

The apparatus used for these experiments is shown schematically in Fig. 5.1. The ion beam, homogeneous in mass and energy, delivered by the Cockcroft-Walton accelerator, passes through the windowless gas cell and is analyzed according to charge. The differential pumping properties of the system allow a stopping-gas pressure of up to 0.2 mm Hg to be established in the gas cell without the pressure in the accelerator or electrostatic analyzer being appreciably altered. The undeflected (uncharged) beam impinges on a differential foil thermocouple, similar to that described by Gardon,[2] although a much thinner foil is used ($5 \times 10^{-5}$ in.), and higher sensitivity results at some sacrifice in time constant. Also, as seen in Fig. 5.2, the unit may be used as an efficient Faraday cup for the

[1] H. S. W. Massey and E. H. S. Burhop, *Electronic and Ionic Impact Phenomena*, p. 506, Oxford University Press, 1952.

[2] R. Gardon, *Rev. Sci. Instr.* 24, 366 (1953).

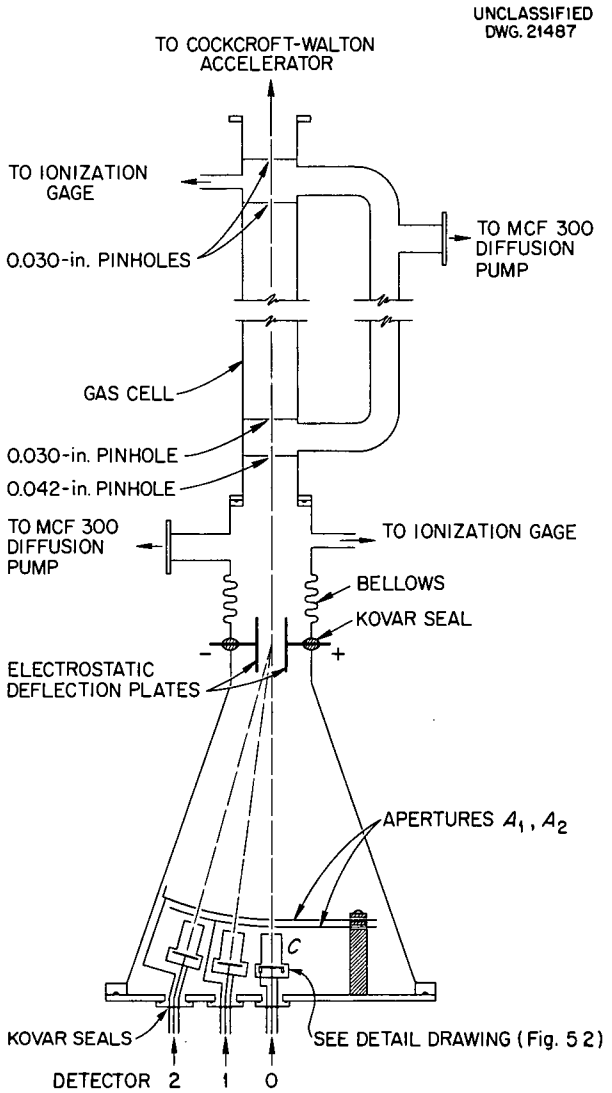


**Fig. 5.1. Schematic Drawing of Apparatus used to Measure Ratio of Electron-Capture and Electron-Loss Cross Sections.**

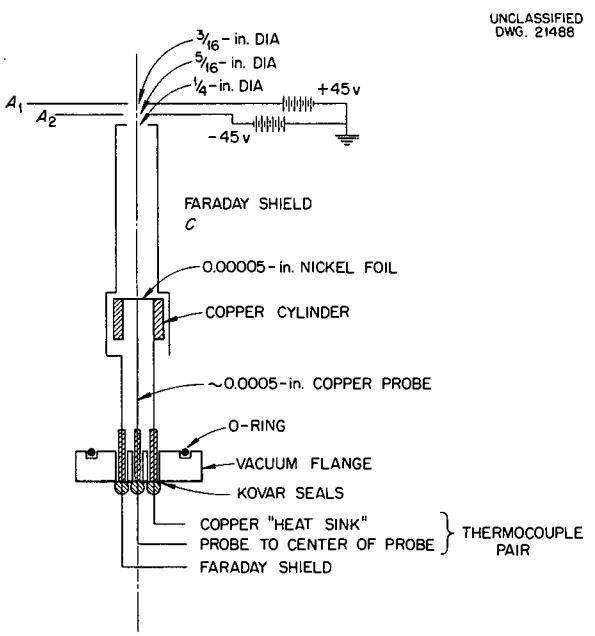


**Fig. 5.2. Schematic Drawing of Neutral (±0) Detector Unit.**

charged particles, or the secondary electron emission collected on C can be used as a measure of the number of incident particles. The other detector units (No. 1 and 2) shown in Fig. 5.1 are identical to No. 0, except they contain no thermocouple element. The apertures $A_1$ and $A_2$ (Fig. 5.1) serve to define the beam and to control secondary electrons and low-energy positive ions.

The usual method used to measure the fraction of the beam in the various charge states was to record the thermocouple response and/or the secondary electron emission that resulted from the total beam, charged and uncharged; then the charge components were measured on detectors No. 1 and 2, while again the response of the No. 0 detector was recorded. The results of such measurements are shown in Figs. 5.3, 5.4, and 5.5. In order to ensure that the charge distribution of the beam emerging from the gas cell was the equilibrium distribution for the particular energy, the measurements were repeated for at least one significantly different gas-cell pressure. Since the literature contains the results of a few measurements of these cross sections for hydrogen[3] and helium[4] ions, these ions were studied first. The agreement for protons, although not good, may be considered as satisfactory, but the differences between the helium results and those of Snitzer[4] are larger than can be attributed to random errors in measurement. In an attempt to resolve these differences, several changes in apparatus and procedure have been made, without materially affecting the results. Additional equipment with which the separate capture and loss cross

[3]For example, see for $H^+$ in hydrogen: F. L. Ribe, *Phys. Rev.* 83, 1217 (1951); for $H^+$ in air: H. Kanner, *Phys. Rev.* 84, 1211 (1951).

[4]E. Snitzer, *Phys. Rev.* 89, 1237 (1953).

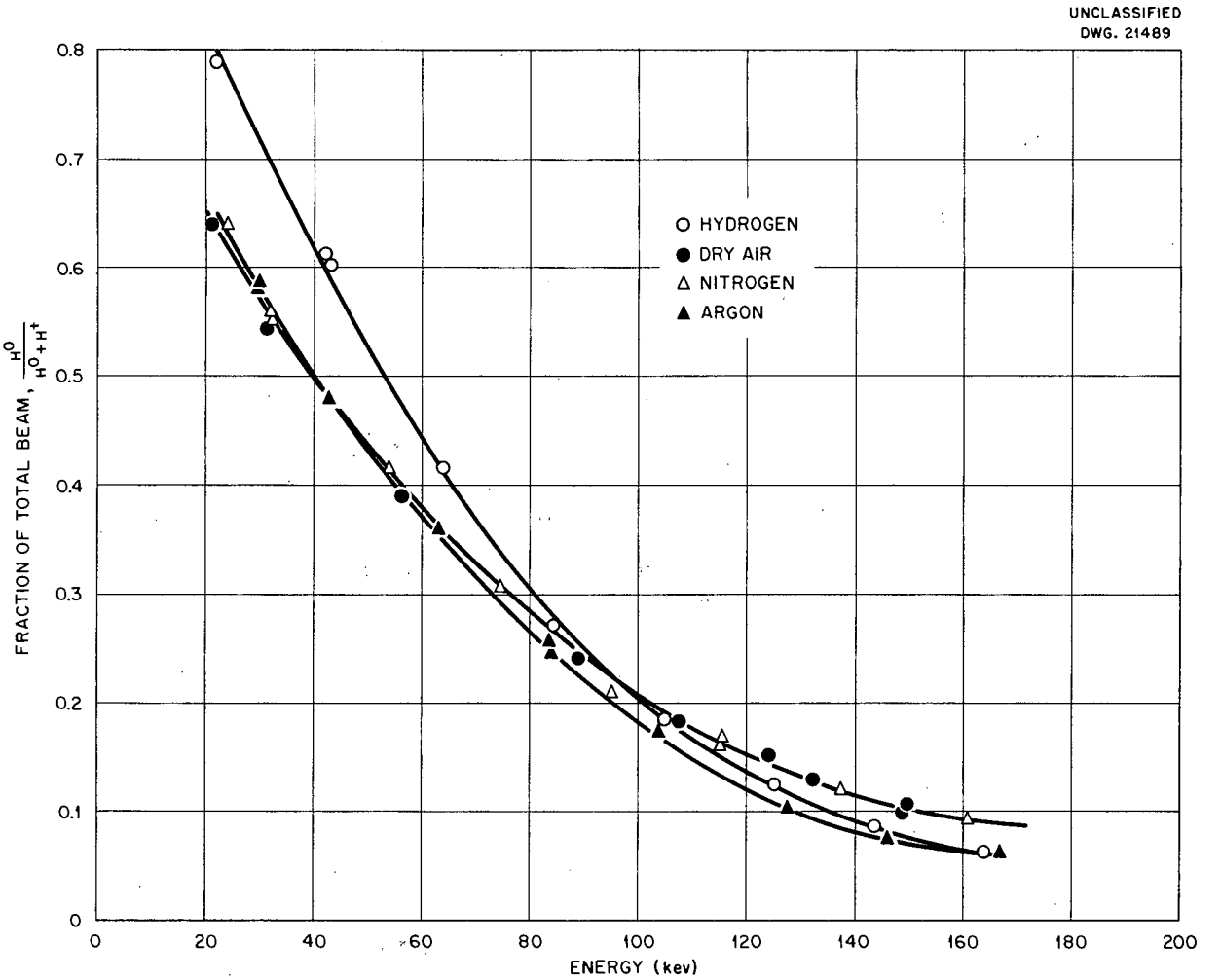


**Fig. 5.3. Variation of the Equilibrium Fraction of $H^0$ in the Beam after Passing Through the Gas Cell.**

sections will be measured is being assembled. The independently measured ratio of cross sections described here is expected to indicate the correctness and consistency of the separate cross section measurements.

### ELECTRON MULTIPLIER STUDIES

C. F. Barnett P. M. Stier
G. E. Evans

The investigation of the Allen type of electron multiplier as a detector for heavy positive ions has been completed.[5] It has been established that this type of multiplier is an excellent relative detector for many applications, and if proper care is taken, it is a reliable device for quantitative measurements.

The efficiency for counting positive ions of energy greater than 10 kev can be made 100% (Fig. 5.6). With a few exceptions (notably neon ions), the gain of the multiplier at higher energies increases as the mass increases, although no simple relation is apparent (Fig. 5.7). (The term "gain" is defined as the number of electrons collected at the last dynode per incident positive ion.) Positive-ion currents as large as $10^{-15}$ amp may be detected with high-speed counting circuits, and the multiplier may be used as a linear current amplifier in the range $10^{-15}$ to $10^{-12}$ ampere. As reported earlier,[5]

[5] G. E. Evans, P. M. Stier, C. F. Barnett, and V. L. DiRito, *Phys. Quar. Prog. Rep. Dec. 20, 1952*, ORNL-1496, p. 18.

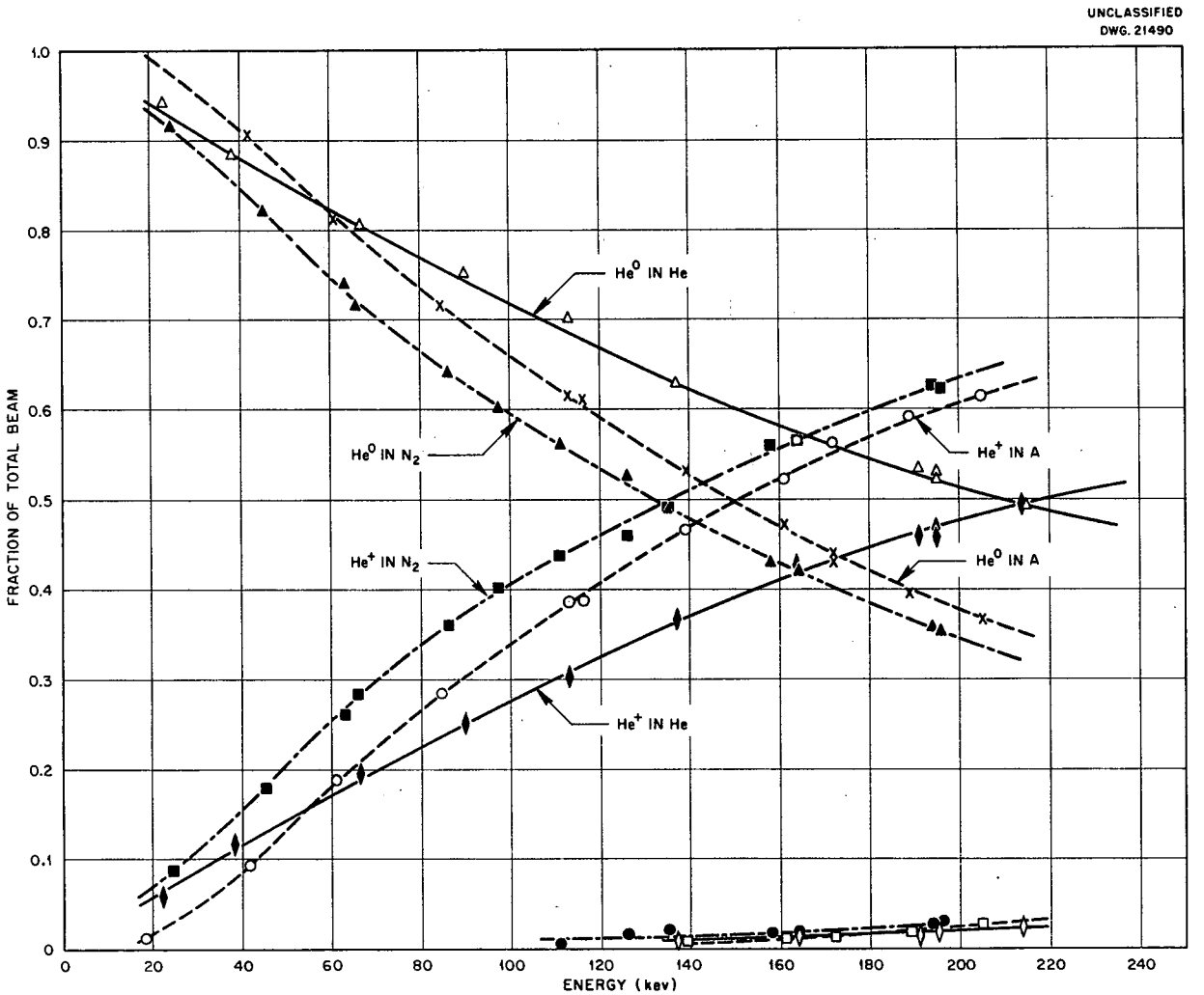


**Fig. 5.4. Equilibrium Charge Distribution on Helium Beam after Passing Through the Gas Cell.**

after the first few hours of operation, changes in multiplier gain as a result of dynode aging were found to be negligible, and the multiplier characteristics are pressure independent below $10^{-4}$ mm Hg. For each application, the efficiency should be determined by an analysis of the pulse-height spectrum. Typical pulse-height spectra from a well-activated multiplier are shown in Fig. 5.8 for 9- and 100-kev nitrogen ions. The secondary electron multiplier may be used as a detector of high-energy neutral particles, although further comparisons should be made between the pulse-height spectra for atoms and ions of the same mass and energy.

A detailed report for the investigations of the performance of this electron multiplier as a heavy-ion detector is being prepared for publication in the near future.

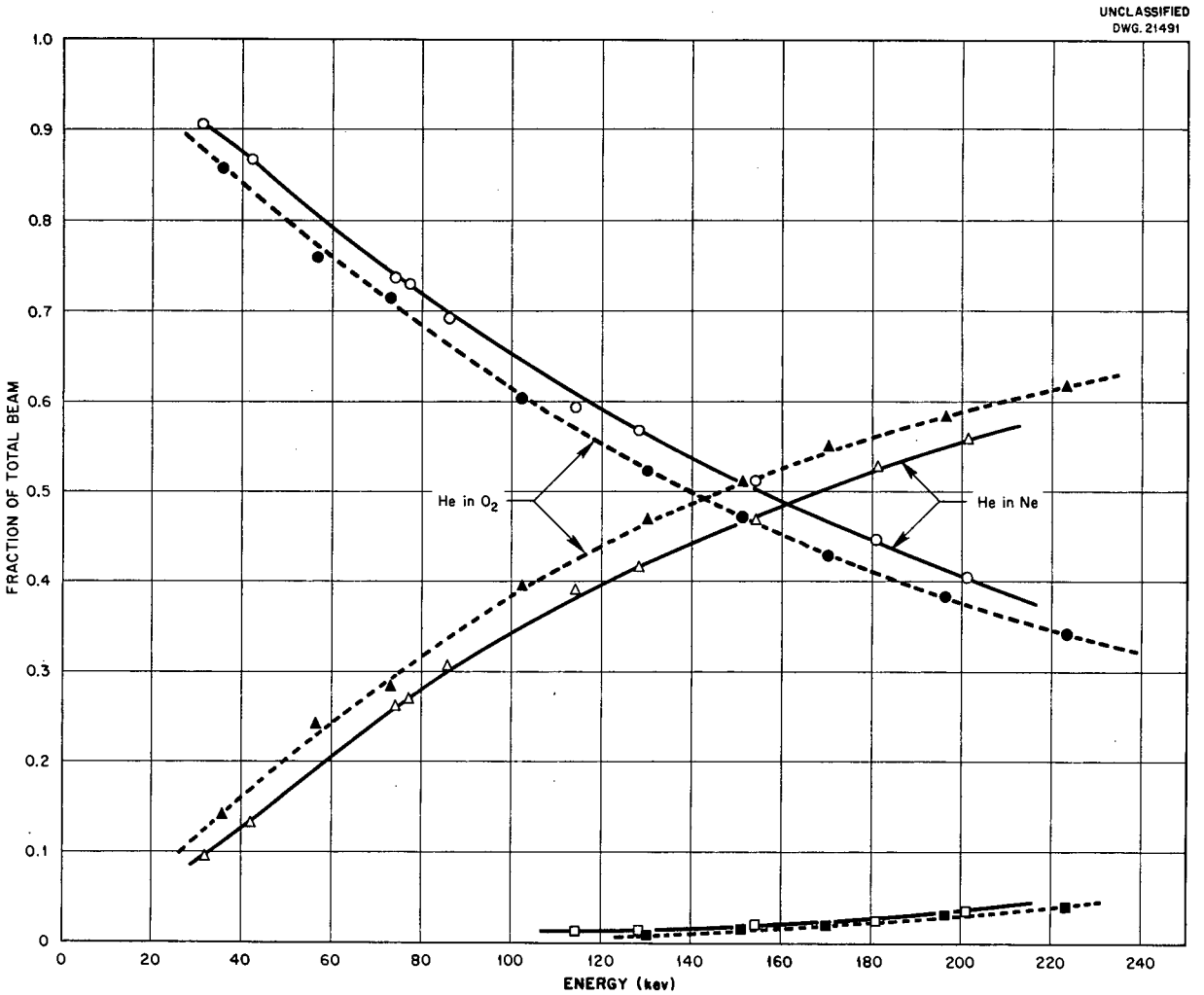


**Fig. 5.5. Equilibrium Charge Distribution in Helium Beam after Passing Through the Gas Cell.**

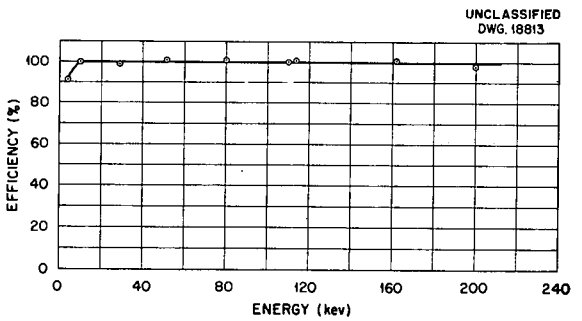


**Fig. 5.6. Counting Efficiency vs. Energy, for $N^+$.**

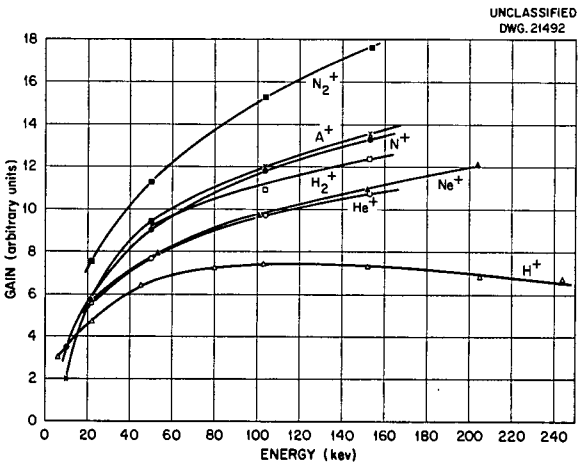


**Fig. 5.7. Electron Multiplier Gain as a Function of Energy for Various Masses.**

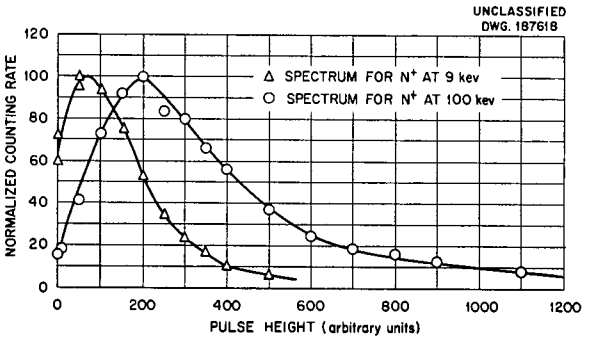


**Fig. 5.8. Pulse Spectrum from Electron Multiplier.**

# 6. NEUTRON CROSS SECTIONS

## STABLE ISOTOPE NEUTRON CROSS SECTIONS

H. Pomerance

Measurement of the thermal neutron capture cross section of $Th^{230}$ (ionium) with the ORNL pile oscillator gave a value of 26 ± 2 barns with 95 barns for gold as the standard for comparison. The sample was 335 mg of $ThO_2$, separated at Y-12 by electromagnetic methods from an enriched source of material supplied by the Argonne National Laboratory; the final assay was 87.85% $Th^{230}$ and 12.15% $Th^{232}$. The presence of $Th^{232}$ was corrected for at 7.0 barns per atom; the chemical impurities, known spectrographically, accounted for 1.5% of the capture by the sample. The accuracy of 2 barns is somewhat arbitrary, being the value (±7%) quoted for pile oscillator work in the past with a single available sample of a substance.

This new value agrees with one of the two previous measurements of the activation cross section to form $Pa^{231}$. Hyde found 29 barns, based on $\sigma(Th^{232})$ = 7.0 barns, whereas Jaffey and Hyde found 61 barns from an absolute flux and absolute counting rate determination.

[1]A. H. Jaffey and E. K. Hyde, NNES, Div. IV, Vol. 1713, paper 9.3 (classified).

## NEUTRON TIME-OF-FLIGHT SPECTROMETER

G. W. Pawlicki E. C. Smith
P. E. F. Thurlow

Measurements on Th, $Ni^{62}$, and $Tc^{99}$ have been made with a resolution of 0.5 μsec/meter full width at half maximum. The results are presented below.

**Technetium-99.** The transmission of a sample of $KTc^{99}O_4$ containing 1.605 g/cm$^2$ of $Tc^{99}$ was found in an energy range down to 2 ev, as illustrated in Fig. 6.1. The level appearing at 2.14 ev may be due to an impurity. An analysis of the 5.6-ev level indicates that $\sigma_0\Gamma^2$ = 130 ± 5 barns-ev$^2$. As yet, no accurate energies have been assigned to the levels above 54 ev because of the statistical uncertainty in the data in this region. Further data are to be taken.

**Nickel-62.** Preliminary measurements on the $Ni^{62}$ sample were given in the last progress report.[2] Another run at a resolution of 0.5 μsec/meter was made, and the data were extended to lower energies with a run at a resolution of 1.5 μsec/meter. These data appear in Fig. 6.2 and indicate a resonance for which $E_0$ = 3900 ev, whence $\sigma_0 = 4\pi\lambda\!\!\!^{-}{}_0^2$ = 666 barns. Since the $Ni^{62}$ is only 92.7% abundant in the sample,

[2]G. S. Pawlicki, E. C. Smith, and P. E. F. Thurlow, *Phys. Quar. Prog. Rep. Dec. 20, 1952*, ORNL-1496, p. 14.

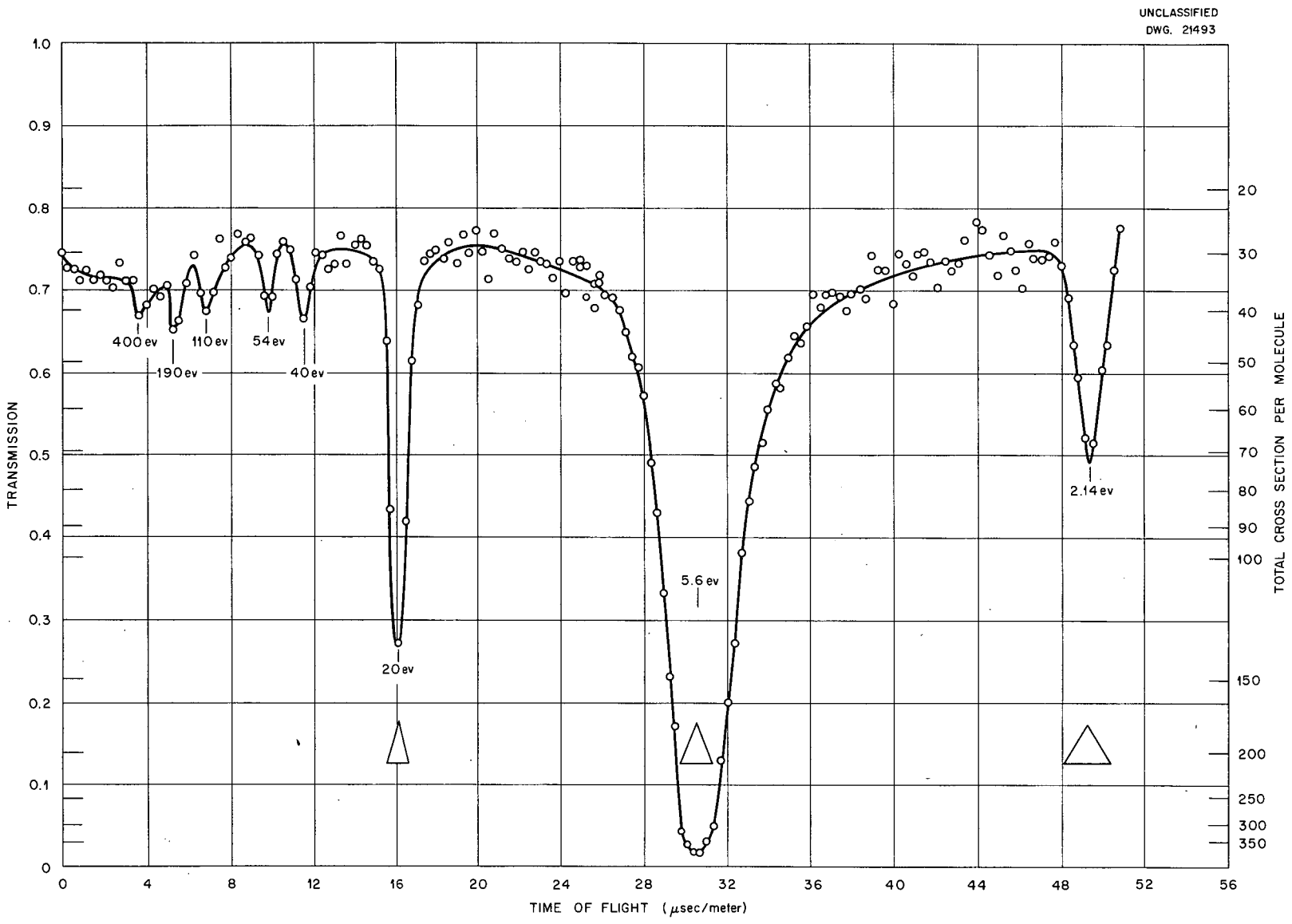


**Fig. 6.1. Transmission of K $Tc^{99}O_4$ Obtained by Using a Sample Containing 1.605 g/cm$^2$ of $Tc^{99}$.**

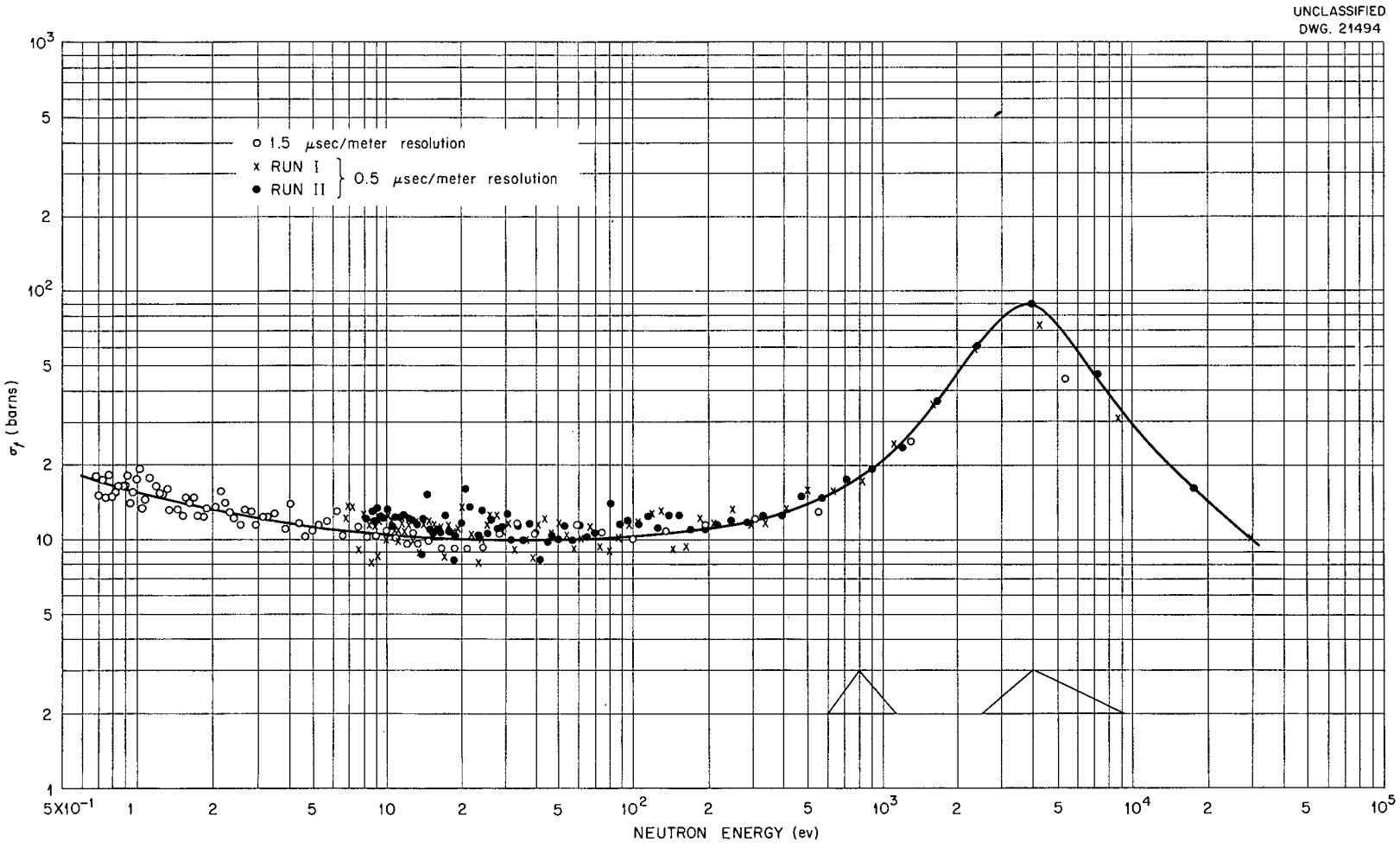


**Fig. 6.2. Cross Section of $Ni^{62}$, 1.89-g/cm$^2$ Sample.**

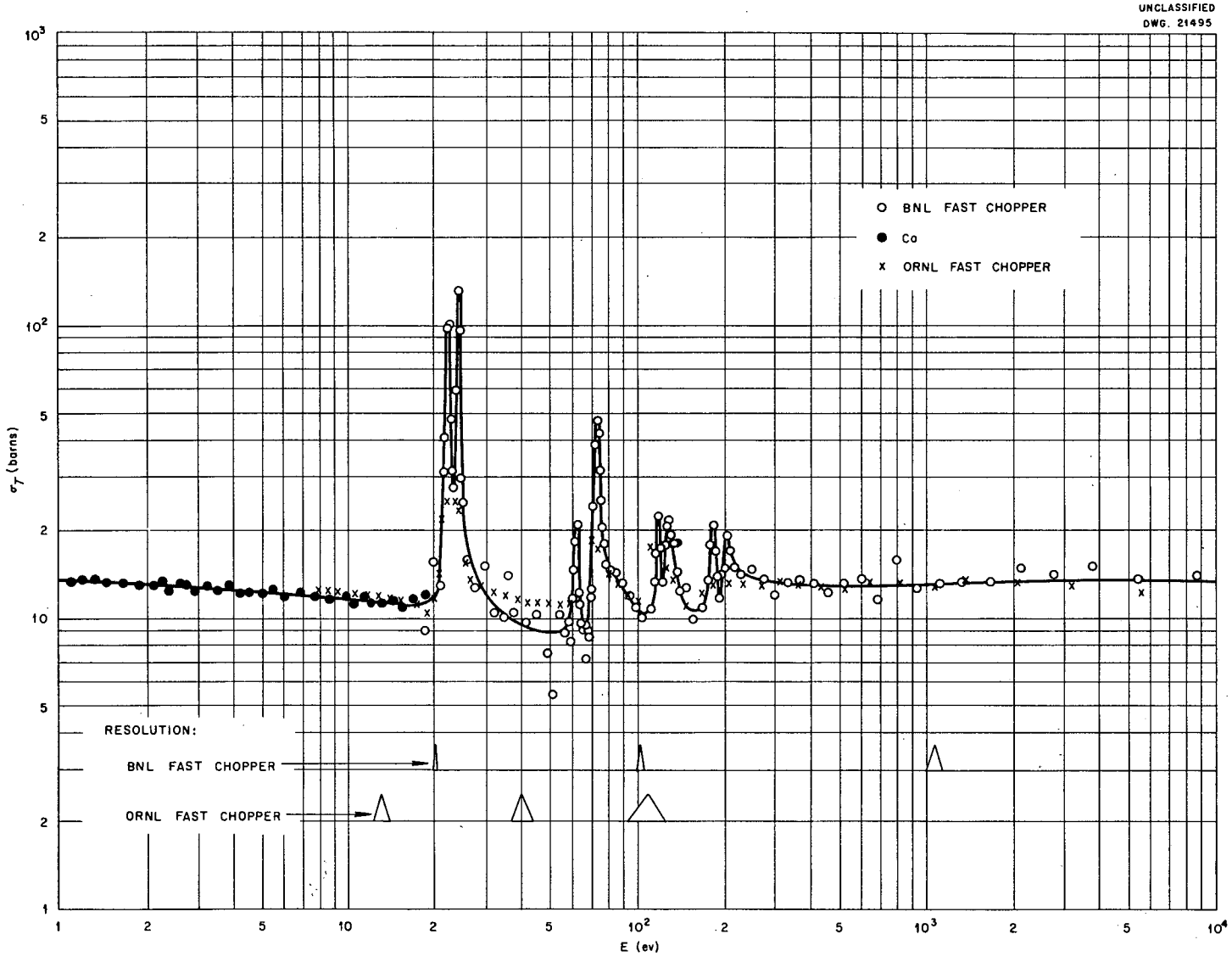


**Fig. 6.3. Thorium – Total Cross Section Comparison of Fast Chopper Data of BNL and ORNL.**

the sample $\sigma_0$ should be 620 barns. The area above the transmission dip indicates that $\sigma_0\Gamma^2 = 617 \times 10^6$ barns-ev$^2$, so $\Gamma \approx 1000$ ev.

**Thorium.** The cross section obtained from transmission measurements on a 35.03 g/cm$^2$ sample of Ames thorium of high purity is presented in Fig. 6.3, along with the data in supplement 2, AECU-2040. Although the data from the Brookhaven fast chopper were obtained with 3.3 times better resolution, the statistical accuracy of the present work indicates a better quality of data in the region between 30 and 55 ev, where an unfavorable transmission was probably used by the other workers.

**Neutron Detector.** A scintillation type of neutron detector, designed to replace the present $BF_3$ chamber, has been assembled and is undergoing preliminary tests. The detector consists of an enriched boron slab that is located in the neutron beam; the slab is surrounded by sodium iodide scintillation counters. Monoenergetic $Li^{7*}$ gamma rays are counted by using a pulse-height analyzer to reduce gamma-ray background.

# 7. INSTRUMENTATION

## DOUBLE-LINE LINEAR AMPLIFIER

J. E. Francis P. R. Bell
G. G. Kelley

A tentative model of a new linear amplifier that is the result of several previous attempts to improve the A-1 linear amplifier has been built and partially tested. There were three main reasons for rejecting the previous models: the difficulty in driving the connecting cable between the preamplifier and the main strip while still maintaining linearity; the small overshoots, which were caused by slight mistermination of the delay line used for differentiating the signal and which were amplified into large false signals under overload conditions; the large negative excursions of the base line when a modulated or rapidly varying source such as obtained from a pulsed cyclotron was used. Several features have been incorporated into this new design to improve operation under overload conditions.

Figure 7.1 is a diagram of one of the previous attempts to improve the design of the A-1 amplifier.

UNCLASSIFIED
DWG. 21496

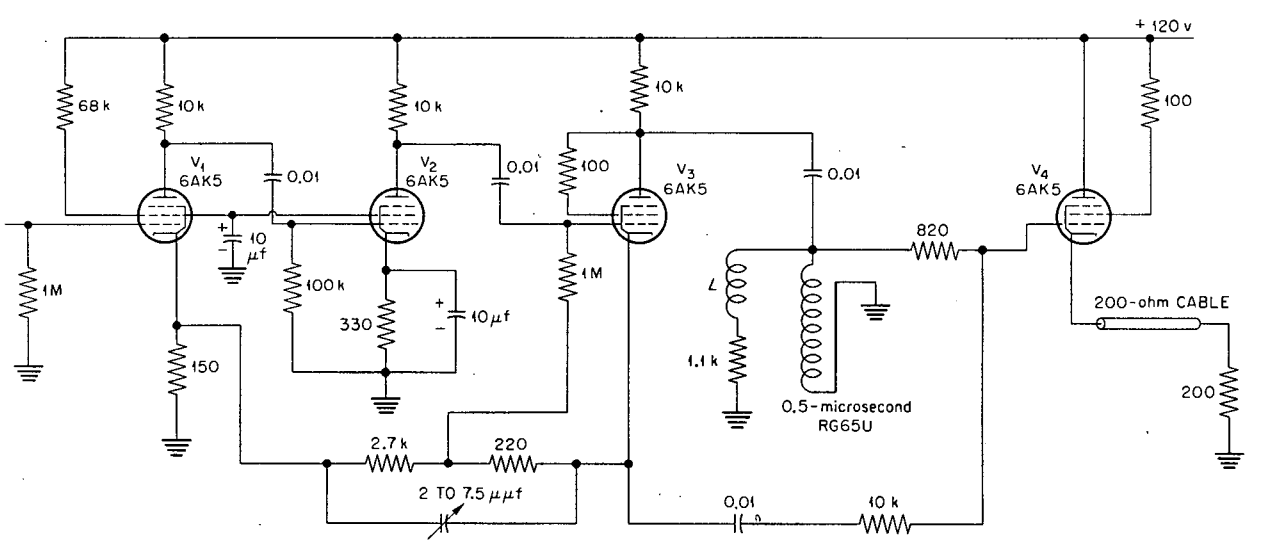


**Fig. 7.1. Preamplifier of A-5 Linear Amplifier.**

Tubes $V_1$, $V_2$, and $V_3$ comprise a conventional feedback group with a gain of 20. The signal is inverted by taking the signal from the plate of $V_3$. A portion of the signal is taken from the cathode of $V_3$ to compensate for the frequency response of the delay line. This model was abandoned because the output of the cathode follower, $V_4$, was not linear enough for signals in the operating range. The differential linearity could not be made better than 1%.

Figure 7.2 is a diagram of a preamplifier which contains two feedback loops tied together to drive one output. Tubes $V_1$, $V_2$, and $V_3$ comprise a conventional feedback group with a gain of 20. Tubes $V_3$ and $V_4$ are also a two-tube feedback group. The $V_4$ was added so that the output point would always present a low impedance, even when the first loop overloads. This arrangement was abandoned after it was found that the impedance of the output changed from 12 to 20 ohms under overload conditions, which was sufficient to misterminate the delay line differentiator at the far end of the 200-ohm cable. This mistermination produced a multiple overshoot which gave false signals under overload.

The double-line amplifier was finally evolved as a result of the two unsatisfactory designs. This amplifier has an over-all gain of 6000 and has been tested with signal-generator pulses which were 50 times overload and with scintillation-counter pulses which were approximately 20 times overload.

Figure 7.3 is a circuit diagram of the new linear amplifier. The preamplifier ($V_1$, $V_2$) is a two-tube feedback loop designed to accept an input pulse as large as 4 volts without overloading and able to drive the 200-ohm connecting cable to 20 volts without overloading. However, since the pulse is integrated at the input, the maximum signal that can be tolerated is determined by the counting rate or pileup.

The output of the preamplifier is fed into a 200-ohm line which is terminated only on the preamplifier end. This step signal is differentiated by a shorted delay line whose characteristic impedance is 1000 ohms so that a pulse signal is obtained. For this model, the pulse is 1 $\mu$sec in duration and is fed into the grid of $V_3$. A portion of the preamplifier signal is also taken from the 200-ohm line and is fed through a network to the cathode of $V_3$ to compensate for the complex frequency response of the delay line.

A fairly successful attempt was made to design an amplifier that would use the output from $V_4$

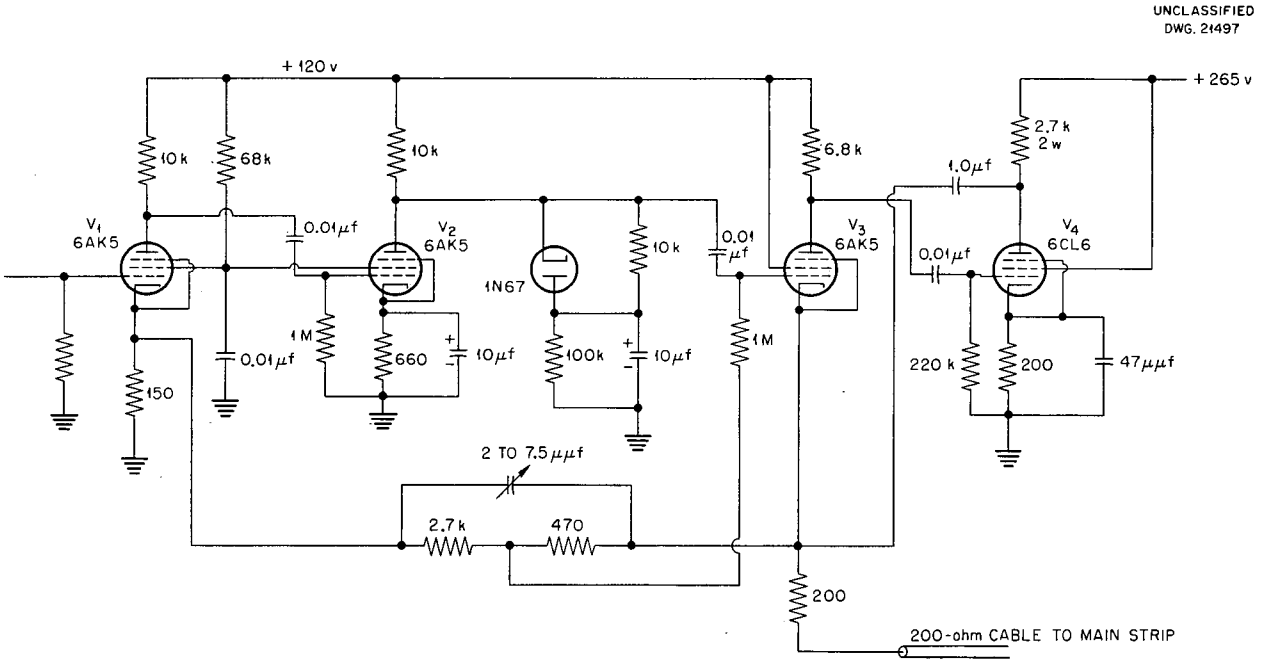


**Fig. 7.2. Preamplifier of A-6 Linear Amplifier.**

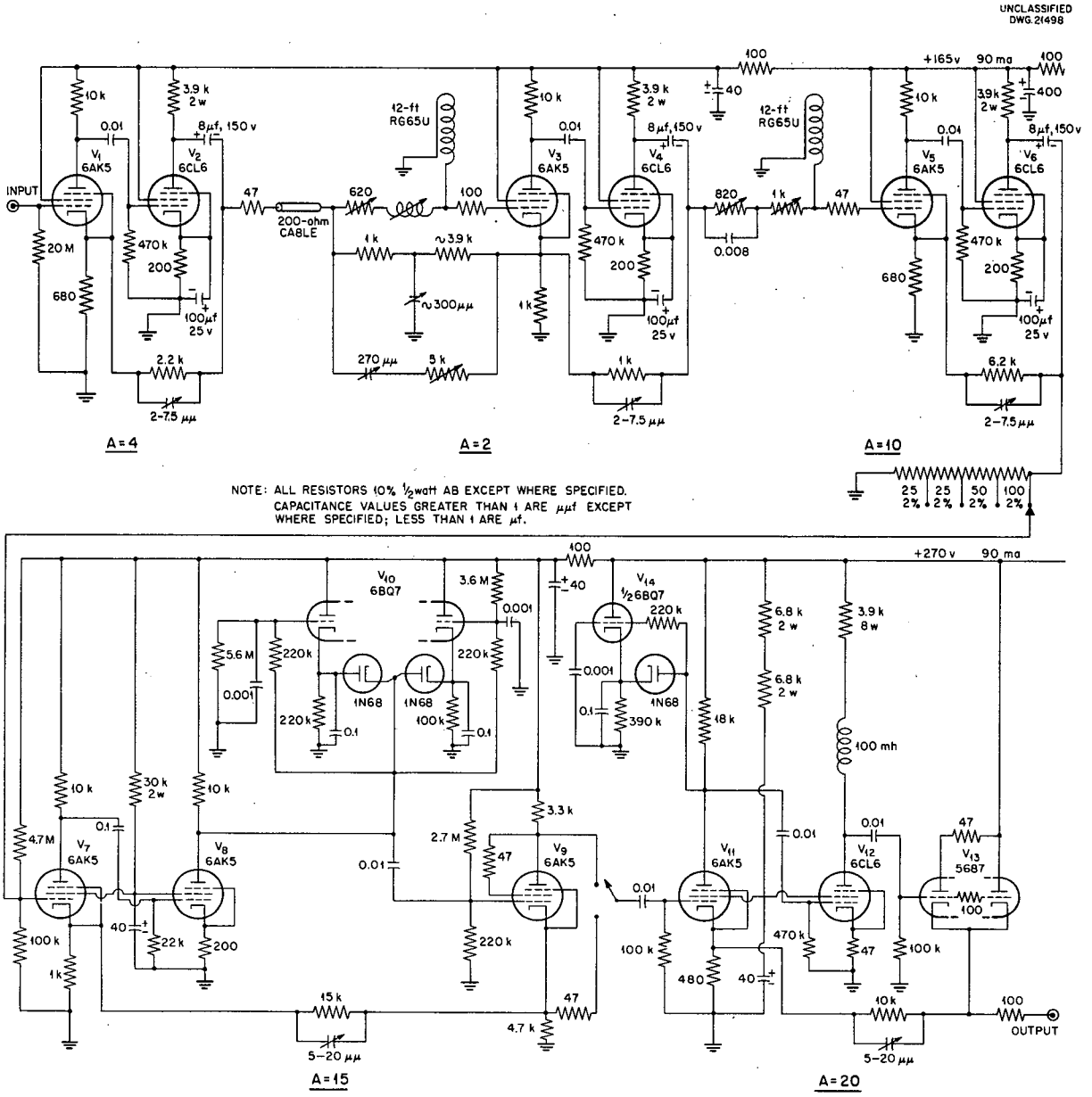


**Fig. 7.3. Double Line Linear Amplifier – Preliminary Design.**

without differentiating a second time. By using the same tubes as shown in the diagram, the second line was replaced by a 1000-ohm resistor to ground. If this amplifier were built as a final design, the third loop ($V_5$, $V_6$) would be omitted. Under these conditions and for most purposes, the amplifier worked as well as an amplifier with two lines. The main objections were the shift in the base line with a modulated source and a high counting rate and the critical adjustment of the d-c compensation of the delay line.

The signal from the second loop ($V_3$, $V_4$) drives a second shorted delay line through its characteristic impedance (1000 Ω). The second line is cut to the same length as the first. This double differentiation produces a signal which is almost

symmetrical about the base line and therefore causes the average signal current in the following stages to be almost zero.

Tubes $V_5$ and $V_6$ provide an additional gain of ten. A step potentiometer at the output provides the gain control over a range of 16.

Tubes $V_7$, $V_8$, and $V_9$ comprise a conventional feedback loop with a gain of ten. Provision is made for accepting either a positive or a negative pulse at the input, and, since the output group delivers only a positive pulse, the signal is inverted for a negative input pulse. Maximum signal size to the output group ($V_{11}$, $V_{12}$, and $V_{13}$) is limited by means of diode limiters on the plate of $V_8$ in order to prevent drawing grid current in the following stages.

Tubes $V_{11}$, $V_{12}$, and $V_{13}$ compose the output group with the addition of a diode limiter to limit the positive pulse from the plate of $V_{11}$. The circuit constants were chosen so that the maximum output pulse may be fed into a 1000-ohm delay line without drawing grid current in the 5687 output cathode follower.

Figure 7.4 shows the spectra obtained under three different conditions. The plain dots show the spectrum obtained from $Cd^{109}$. The lower peak is due to the 22-kev x ray from the silver daughter, and the upper peak is approximately 88 kev. The crosses show the spectrum obtained from the $Cd^{109}$ in the presence of a thorium source which has a 2.67-Mev gamma ray. The circles show the thorium alone under the same conditions, and the peak at 1185 pulse-height units is evidence of the overload level. The limiter in the fourth group was set low for this test. In the final model, the limit level will be raised so that all overload pulses will appear above 1400 pulse-height units.

The amplifier was also tested by using a scintillation counter with a thallium-activated sodium iodide crystal and a modulated source. The modulated source was made by placing a strong source of $Co^{60}$ in a centrifuge so that the source distance from the crystal varied rapidly between 6 and 36 cm. A $Cd^{109}$ source was also placed on top of the crystal. The voltage on the scintillation counter was then adjusted so that the 22-kev x ray from the silver daughter of the cadmium could be seen on an oscilloscope. Figure 7.5 is a photograph of the oscilloscope trace under two conditions. In the top trace, the centrifuge was spinning so that the source strength was varying rapidly, while in the bottom trace both sources were stationary. There is very little shift in the base line, as is evidenced by the base line being the same width in both traces. No shift or widening of the 22-kev line was observed when the centrifuge was spinning. There is a shift in the limit level of the overload pulses, but this does not cause any serious difficulty.

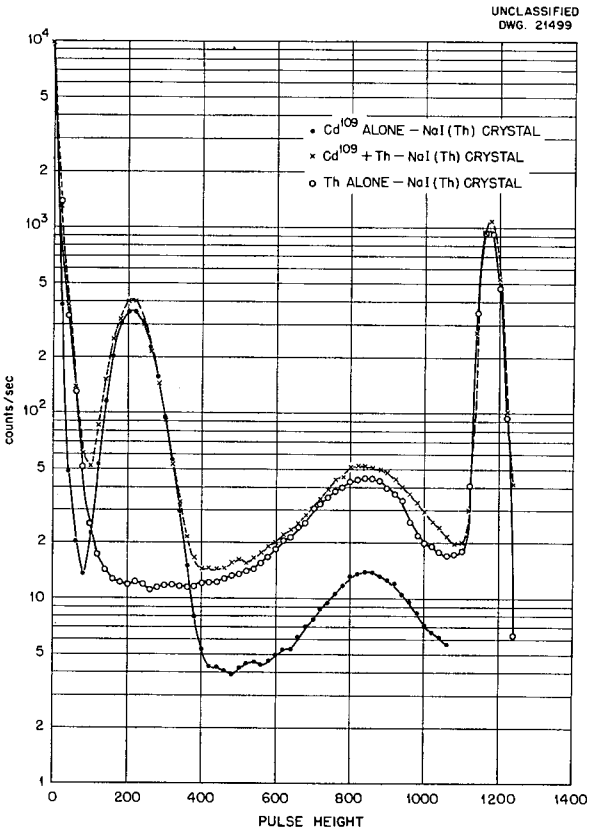


**Fig. 7.4. Spectra Taken by Means of the Double Line Amplifier – Overload Characteristics of the Amplifier are Demonstrated.**

The amplifier has a rise time of approximately 0.2 $\mu$sec. It is expected to operate under overload conditions up to 50 times overload as long as the pileup at the input does not exceed 4 volts. This amplifier will facilitate greatly the study of low-energy radiation in the presence of high-energy radiation.

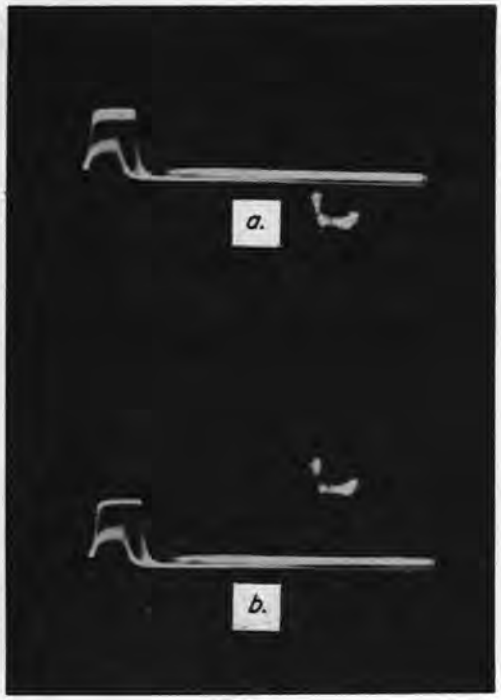


**Fig. 7.5. Amplifier Output with Intensity-Modulated Source.**

## MULTICHANNEL ANALYZERS

G. G. Kelley P. R. Bell
C. C. Harris

The analyzer described in a previous report[1] was called a 20-channel analyzer. This name is misleading because it gives the impression that the analyzer divides an entire pulse spectrum into 20 channels. The instrument is really a 120-channel analyzer – 20-at-a-time. This analyzer is now being produced commercially and two of the units have arrived at the Laboratory. The original instrument is still in use by the Physical Electronics Group.

Work is in progress to develop an analyzer to cover the entire pulse spectrum at once. Techniques developed recently by the Physical Electronics Group have made such a device feasible. All the circuitry has been designed and tested, and the mechanical layout and construction remain to be done. It is proposed that the analyzer be contained in a portable console type of frame with a sloping panel to contain all registers, interpolation lights, and controls. The 120 channels are divided into three groups of 40; each group has its own window amplifier but all use the same pulse-lengthener and interrogation equipment. There will be an overlap channel between the top discriminator of one group and the bottom discriminator of the next higher group. These channels, 39 and 79, will not be stable and will not be used in plotting a spectrum; however, they will provide a check on the setting of the bias in the window amplifiers of the upper two groups. Channel zero, which will bracket the zero pulse height, and channel one also will not be used.

The analyzer will work on delay-line differentiated pulses of any length from less than 1 μsec to tens of microseconds. One control, associated with a circuit used to reject pileup pulses, must be reset when the signal pulse length is changed. Interrogation occurs 0.6 μsec after the end of a signal and requires an additional 0.6 μsec. A 1-μsec dead time is provided thereafter to permit the pulse lengthener to be reset. It is intended that this same design may be used for an analyzer similar to the present 20-channel analyzer, a 120-channel, 20-at-a-time.

The following sections contain descriptions of some of the circuits for the new 120-channel analyzer and the description of the improved scalers now in use in the 20-channel analyzer.

### Pulse-Handling Equipment for the 120-Channel Analyzer

A new and better method has been devised for producing an interrogate pulse only at the proper time. The circuit refuses to interrogate a signal if its pulse-height-selector pulse is preceded or followed by a pulse spaced too closely or if the pulse itself is abnormally long (indicating pileup). Figure 7.6 is a diagram of the circuit. The circuit receives a signal from a pulse-height selector in the new, double-differentiated linear amplifier described elsewhere in this report. This pulse-height selector is designed to produce a negative square pulse of about 10 volts amplitude that lasts during the time the signal exceeds a low set discrimination level. The pulse is fed in succession through four sections of 1000-ohm delay line that are 0.6, 0.6, 0.5, and 0.5 μsec long. The voltages at the input and the first two taps are joined through three diodes, which may be seen above

[1] G. G. Kelley, P. R. Bell, and C. G. Goss, *Phys. Quar. Prog. Rep. Dec. 20, 1951*, ORNL-1278, p. 27.

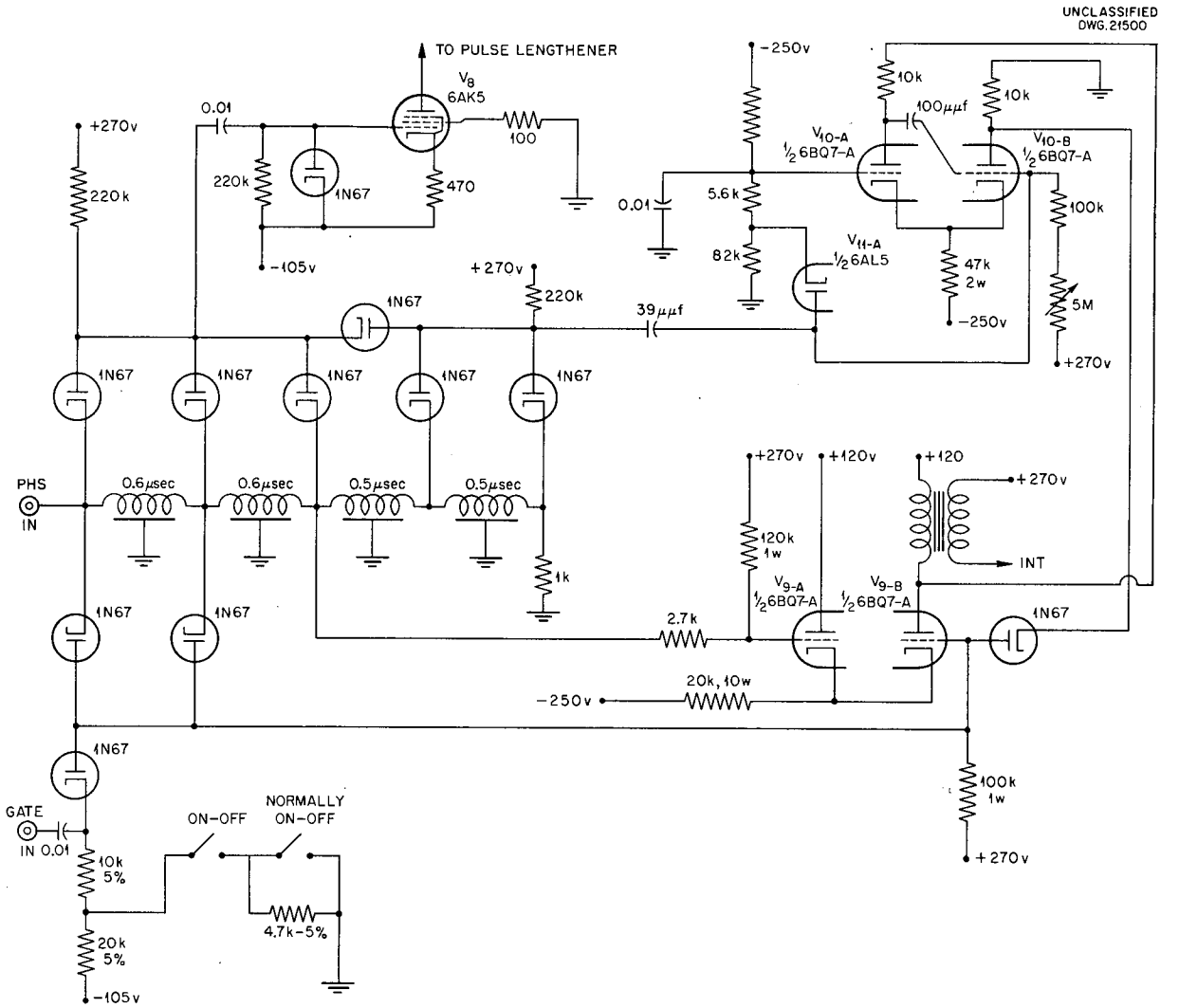


**Fig. 7.6. Interrogate-Pulse Generator for Multichannel Analyzer.**

the lines in the diagram, and provide a gate for the pulse-lengthener current tube, $V_8$. They also connect to a second bus, along with diodes from the third tap and from the end of the line. A pulse is present on this bus from the start of an input signal until 2.2 μsec after the end. The purpose of the pulse will be described later.

Below the line are two diodes which connect the grid of $V_{9\text{-}B}$ to the input and the first tap. This tube, along with $V_{9\text{-}A}$, forms a long-tailed pair. The grid of $V_{9\text{-}A}$ is connected to the second tap on the line through a resistor which, by means of a fixed current, produces an essentially fixed positive bias of about 5 volts. This bias is sufficient to ensure that $V_{9\text{-}A}$ takes all the cathode current unless the negative signal is present on $V_{9\text{-}A}$ but not on $V_{9\text{-}B}$. It can be seen then that current is transferred to $V_{9\text{-}B}$ 0.6 μsec after the end of a pulse-height-selector pulse. At this time the grid of $V_{9\text{-}B}$ rises to ground, but the grid of $V_{9\text{-}A}$ does not rise until 0.6 μsec later. Thus, $V_{9\text{-}B}$ draws current and produces a 0.6-μsec interrogate pulse beginning 0.6 μsec after the signal has passed down through the pulse-height-selector discrimination level. The arrival of a new signal during the interrogation time will remove the interrogation pulse before the signal has risen to the extent that a false answer can be recorded.

Interrogation can be prevented by holding down on either of two diodes connected to the grid of $V_{9\text{-}B}$. One of the diodes is used to permit gated operation and to provide for turning the analyzer on and off. With both the "on-off" and the "normally-on–normally-off" switches closed, the cathode of the gate diode is at ground and the circuit is permitted to function at all times. In the open position of the "normally-on–normally-off" ("normally-off") switch, the cathode is held down at about –10 volts and the grid is thus prevented from rising unless a 10-volt positive gate pulse drives the cathode up to ground. With the "on-off" switch off, the cathode is biased so far negative that no pulse can be recorded even in the presence of a gate pulse.

Tube $V_{10}$ is a timing multivibrator used to reject abnormally long pulse-height-selector pulses and to prevent interrogation when a pulse occurs before the pulse lengthener has had a chance to reset after a previous pulse. Tube $V_{10}$ is driven by the signal, previously described, which is derived by diode coincidence from all the taps on the delay line. It is thrown into its astable condition at the beginning of a signal and transfers the current from $V_{10\text{-}B}$ to $V_{10\text{-}A}$. Tube $V_{10\text{-}B}$ then permits $V_{9\text{-}B}$ to rise and produce an interrogation when called for. The cross-coupling condenser discharges at a rate determined by the setting of a 5-megohm rheostat, and if the input signal lasts too long, the multivibrator will have timed out, the grid of $V_{9\text{-}B}$ will be clamped down again, and interrogation will be prevented. The circuit is adjusted to time out just after the beginning of the longest normal pulse-height-selector pulse. The circuit is prevented from timing out during interrogation, if it has not already done so, by the plate of $V_{10\text{-}A}$ being connected through its load resistor to the interrogation voltage at the plate of $V_{9\text{-}B}$. The presence of an interrogation pulse extends the relaxation time of the cross-coupling circuit, thus preventing the multivibrator from timing out until at least the end of the interrogation pulse. The triggering signal is present until 1 $\mu$sec after the pulse lengthener starts to reset, and thus it prevents a new signal, which might appear during this interval, from retriggering the timing multivibrator and thereby prevents recording of the signal. Thus, there is a 1-$\mu$sec reset time provided for the pulse lengthener.

### Pulse Lengthener and Window Amplifier

A new type of pulse lengthener has made it feasible to lengthen the signal before amplification in the window amplifier. This allows the window amplifier to be slower because the window amplifier operates on the lengthened signal and makes it unnecessary for the lengthener to handle the large signal voltages which are fed to the discriminators. There will be three window amplifiers, each covering 40 channels and providing an output of about 4 volts per channel. Figure 7.7 is a circuit diagram of the pulse lengthener and a window amplifier. The signal from the linear amplifier is fed in through a 1N68 germanium diode which, with $V_1$, forms one side of a long-tailed pair. From the plate of this tube, the signal is fed back through $V_{2\text{-}A}$, a cathode follower with both a-c and d-c coupling, and through two series diodes to its grid. Vacuum diode $V_{3\text{-}A}$, connected to the grid of $V_1$, is the high back-resistance-lengthening diode. A capacity-coupled surge at the end of a pulse is prevented by an arrangement similar to that used in the present analyzer,[2] $V_{3\text{-}A}$ being caught by a diode connected to the cathode of $V_1$. Except during a signal, lengthening is prevented by current from the plate of $V_8$ through an isolating diode, $V_{3\text{-}B}$. This diode prevents residual plate current in $V_8$ from discharging the lengthening capacitor because its cathode is held at practically the potential of the cathode of $V_1$ whenever $V_8$ is cut off. The lengthened signal is fed through another cathode follower, $V_{4\text{-}A}$, to the window amplifier input. Here the d-c level may be adjusted, by means of a helipot, to position the bottom discriminator at any desired position in the spectrum.

The window amplifier is conventional except that d-c coupling is used throughout. This arrangement is particularly important between $V_5$ and $V_6$ because it prevents a distortion, which is due to steady-state current transfer to $V_5$, of the low end of the spectrum. Tube $V_{2\text{-}B}$ regulates the screen voltage for $V_5$ and $V_6$ and provides the 120 volts which is used elsewhere in the circuit.

### Test-Pulse Generator

The motor-driven helipot used to produce a uniformly changing pulse height gave considerable

[2] G. G. Kelley, *Nucleonics* 10, No. 4, 34 (1952).

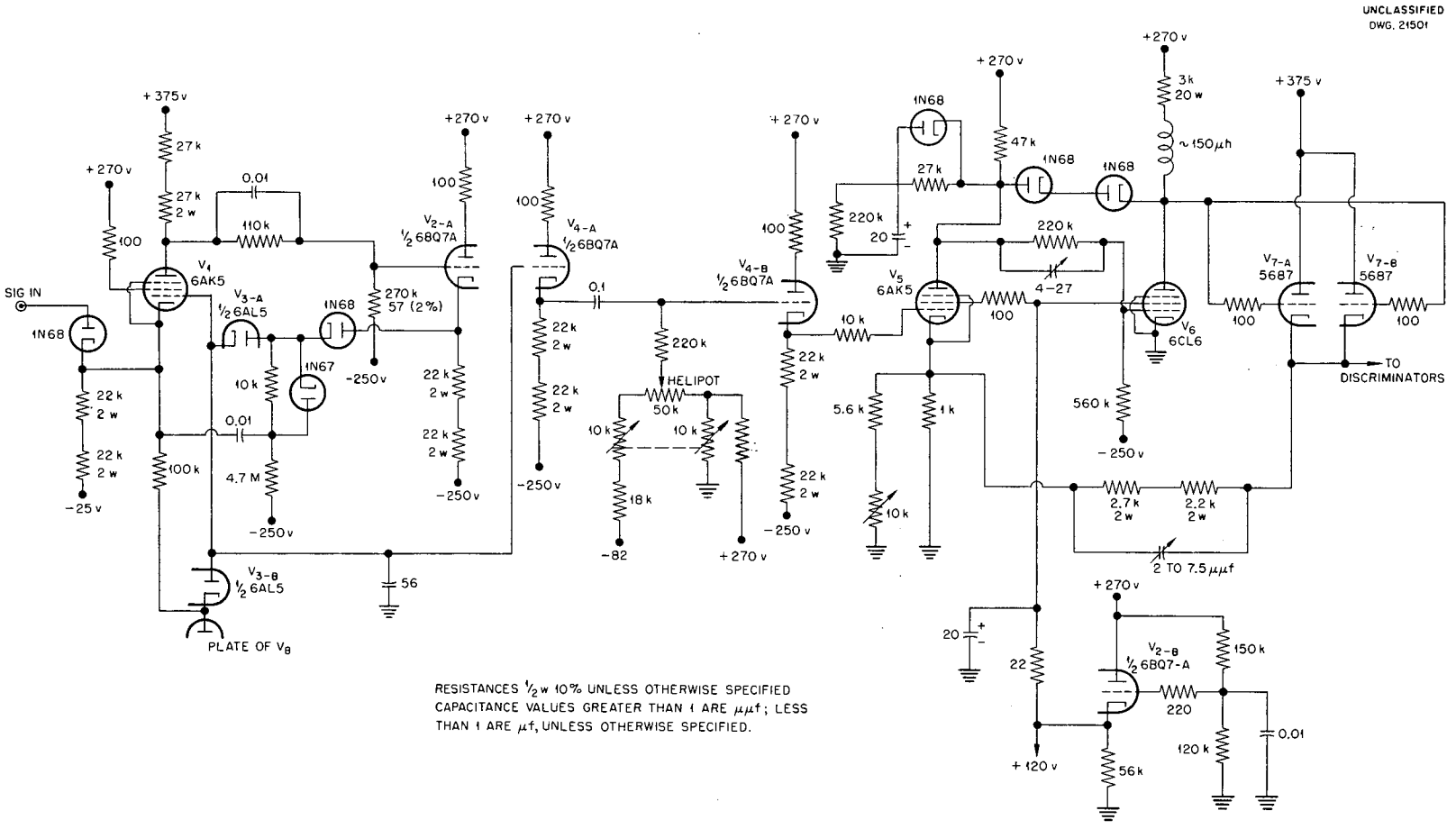


**Fig. 7.7. Pulse Lengthener and Window Amplifier for Multichannel Analyzer.**

trouble and has been replaced by an electronic integrator. A circuit diagram is given in Fig. 7.8. A vacuum tube d-c amplifier is fed back through a large, high quality condenser. The input is provided with a constant current; the output then rises at a rate which is constant within 0.1%. When the output has risen to 100 volts, $V_{4\text{-}B}$ conducts; thus closing $RY_1$ which shorts the condenser and returns the cathode of $V_{4\text{-}A}$ to approximately ground potential. When $SW_1$ is closed, the relay contacts remain shorted. A small portion of the sweep signal ($\frac{1}{2}$ volt maximum) is added to an adjustable d-c voltage. This voltage is made, by means of a mercury relay and shorted delay line, to produce pulses with amplitude exactly proportional to the d-c voltage.

### Double Scale of 16 for Multichannel Analyzer

The 20 scaling channels of the current models of the multichannel pulse-height analyzers employ ten double scales of 16 of improved design. The circuit is of the Higinbotham type and employs a 6AL5-12AU7 scale-of-two. A 12AT7 serves as a register amplifier for both channels, and the drivers for the Veeder Root registers are type 6AK6. The circuit is similar to the miniature scale of 16 previously reported, there being slight changes in component values. Resolving time is approximately 11 $\mu$sec. Reliability is extremely good.

The physical arrangement has resulted in greatly improved accessibility and in lowered construction costs. The unit is constructed on a $4\frac{1}{4} \times 9\frac{5}{8}$ in. flat plate and mounts in the outer wall of the main equipment rack of the multichannel analyzer. The underside of the chassis is mounted outward for accessibility, and the tubes are inside the cabinet and in the main cooling airstream. Point-to-point construction is used throughout. Figure 7.9 is a circuit diagram of one unit of this device. Figures 7.10 and 7.11 show the construction details.

### Improved Scale of 256

An improved fast scale of 256 has been developed for the total and surplus channels of the present analyzer. The circuit offers extreme reliability and moderate speed with considerably less than the usual power drain. Physically, the appearance is quite similar to the aforementioned double scale of 16, since the same chassis and construction techniques have been used.

The circuit is shown in Fig. 7.12. The fast scales have a resolving time of about 4 $\mu$sec when unaided, and less than 1.5 $\mu$sec with grid-catching diodes. Plate current in the conducting tubes is only 2.5 ma. RC-diode coupling is used between

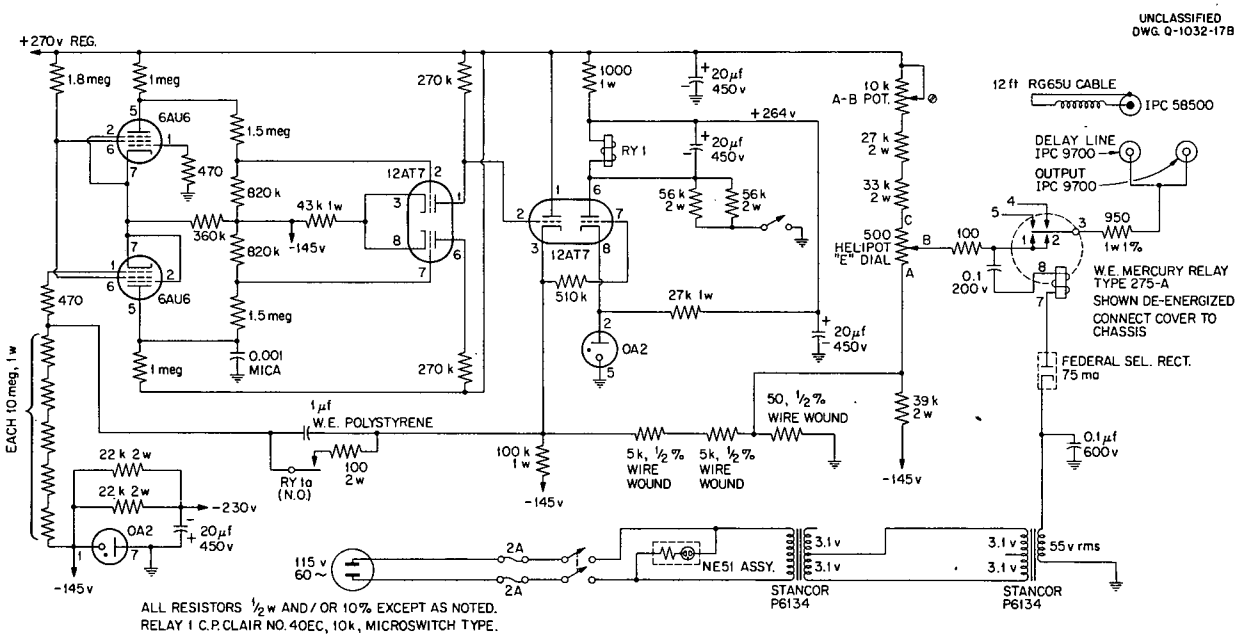


**Fig. 7.8. Multichannel-Analyzer Test-Pulse Generator Circuit.**

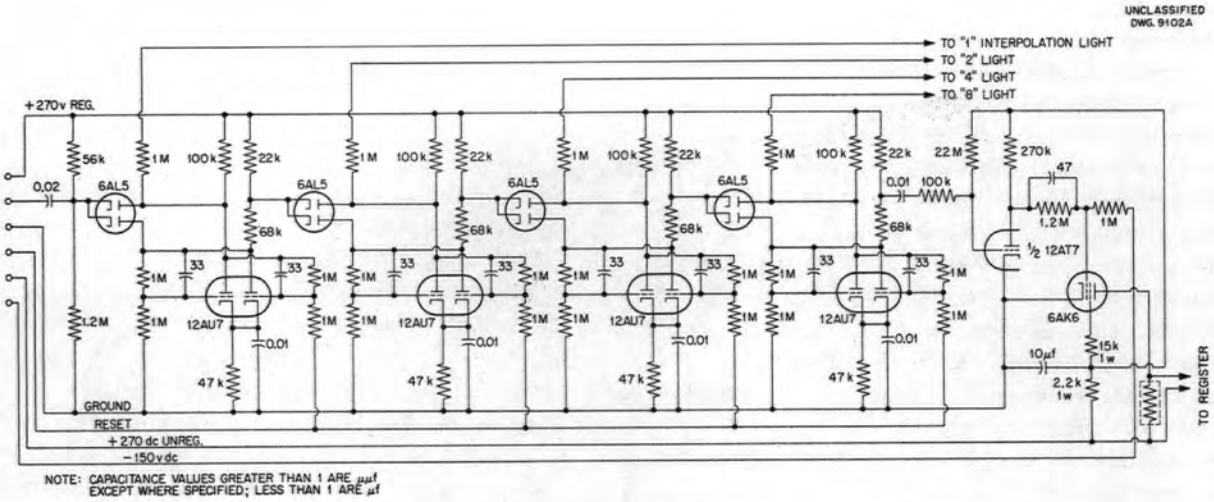


**Fig. 7.9. Basic Scale of 16.** Miniature Higinbotham Scaler.

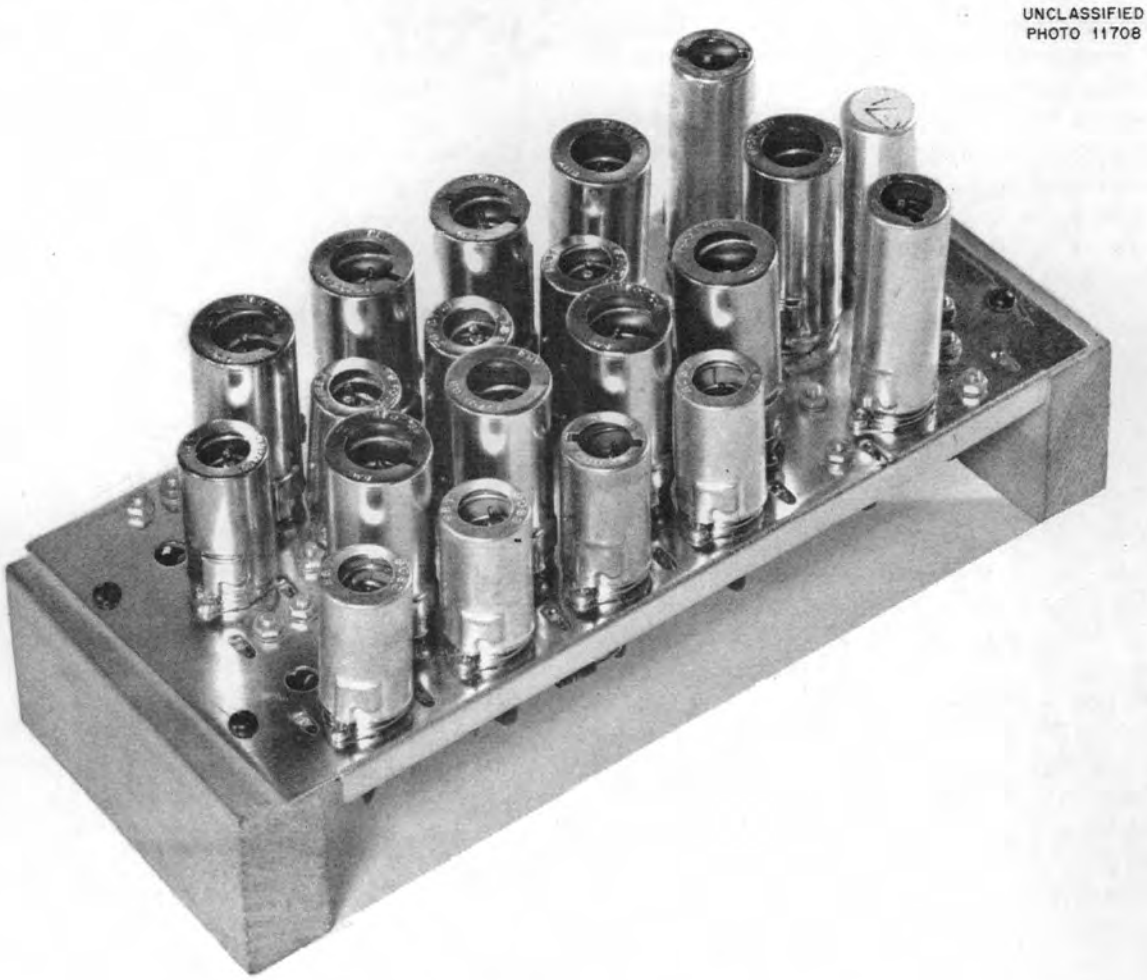


**Fig. 7.10. Double Scale of 16 (Top View).**

UNCLASSIFIED
PHOTO 11709

**Fig. 7.11. Double Scale of 16 (Bottom View).**

UNCLASSIFIED
DWG. 21502

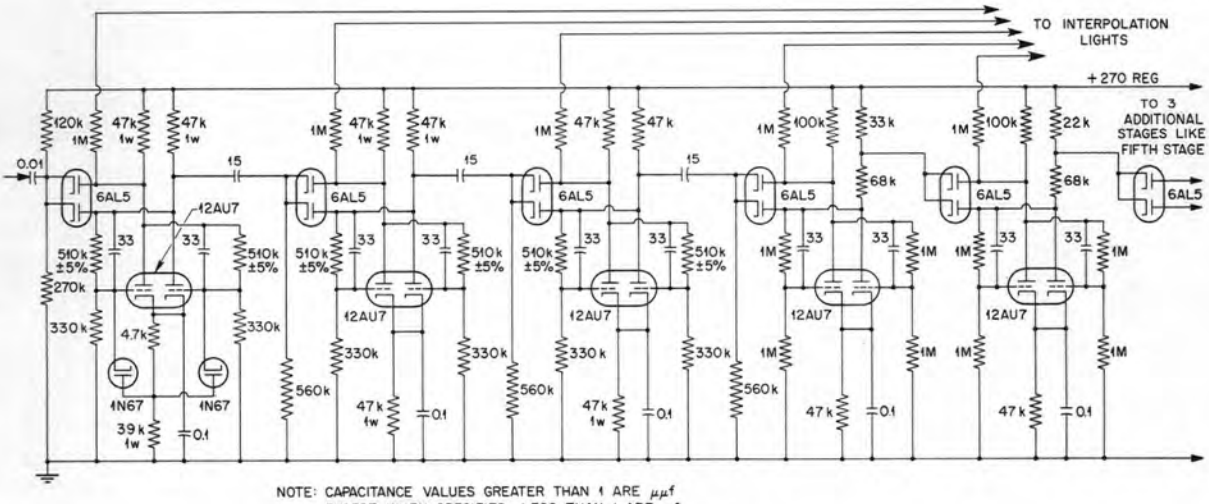


NOTE: CAPACITANCE VALUES GREATER THAN 1 ARE $\mu\mu$f
EXCEPT WHEN SPECIFIED; LESS THAN 1 ARE $\mu$f.
ALL RESISTANCES 10 % ½w AB EXCEPT WHERE SPECIFIED.

**Fig. 7.12. Scale of 256 for Multichannel Analyzer.**

fast scales and at the junction between the last fast scale and the first slow scale. This, together with the use of low $\mu$ tubes, helps to eliminate scale-through failure.

The circuit was designed to operate properly on tubes of almost any condition. The first tests were made with tubes that had previously failed in scaler service in the double scales of 16, and the circuit operated reliably with these tubes even when filament voltage was reduced. Failure occurred at 90% nominal filament voltage, but failure was complete, with no scale-through. With new tubes inserted and plate supply at nominal value, the circuit operated reliably down to 55% nominal filament voltage. The circuit operated reliably over very wide variations of plate supply voltage.

It is believed that the speed and reliability of these units and the reliability of the double scales of 16 will result in considerably improved scaling operation in the present multichannel analyzers.

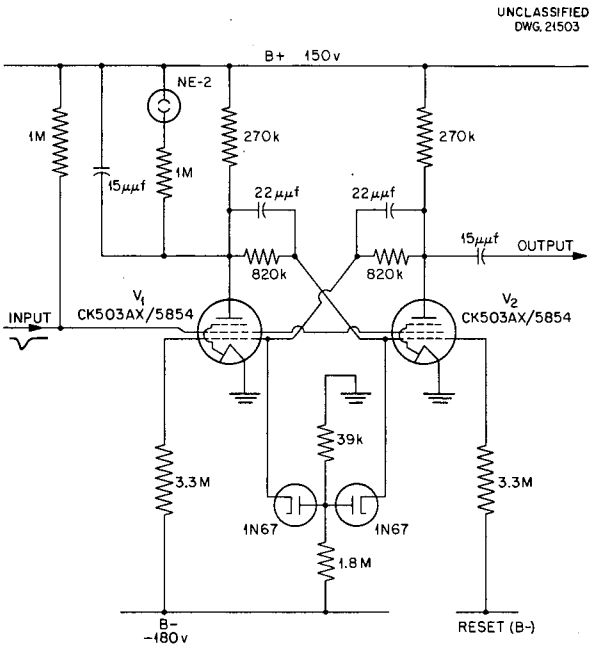


**Fig. 7.13. Subminiature Scaling Stage.**

## SUBMINIATURE SCALING UNITS

C. C. Harris P. R. Bell
G. G. Kelley

### Basic Unit

A subminiature scale-of-two unit has been developed and tested. The circuit uses screen-grid-triggered pentodes, and the total power consumption is less than the plate power consumption of previously existing scales-of-two. Although testing for reliability is not complete, the new units show promise of performing reliably over long periods of time. Resolving time is about 4 $\mu$sec with grid catching diodes and is approximately 25 $\mu$sec for the unaided circuit.

In the design and construction of multichannel pulse-height analyzers, the need for a small, low power drain, reliable scaling unit has arisen. In an attempt to meet this need, the circuit of Fig. 7.13 has been developed.

The tubes, $V_1$ and $V_2$, are of the type CK503AX or 5854. Triggering is accomplished by means of a negative pulse applied to the common screen-grid connection. The minimum pulse size for reliable operation is about 8 to 10 volts. Satisfactory operation is achieved with a trigger pulse that has a rise time of from 0.4 to 1 $\mu$sec and a decay time constant from 2 to 8 $\mu$sec. Since this circuit is not of the Higinbotham type, it is more critical of input waveforms than the Higinbotham circuit, but is tolerant enough to permit reliability under the conditions encountered in present analyzer circuits. The lack of germanium diodes of sufficient quality prevents development of this circuit into a Higinbotham type; however, the circuit seems to be greatly superior to ordinary capacitance-coupled scales, and it is hoped that it will prove reliable. Two factors that indicate reliability are the very good stability of these tubes and the stability inherent in hard "bottoming" of pentodes. Resolving time measured in response to a signal similar to that provided in the present multichannel analyzers varies with signal amplitude and supply voltage. With a trigger of 15 volts amplitude, 0.5-$\mu$sec rise time, and 6-$\mu$sec decay time, the resolving time of the unaided circuit of Fig. 7.13 is about 25 $\mu$sec. This time may be lowered to 4 $\mu$sec by catching the grid waveforms with diodes.

The nominal currents are: plate, 0.5 ma; screen grid, 0.14 ma; and grid, 0.09 ma. Plate and screen voltages of the conducting tube are nominally 14 and 10 volts, respectively. The grid voltage for 0.09-ma grid current is approximately +0.75 volt.

The two 1.25-volt, 30-ma filaments consume 75 milliwatts. All other consumption is approximately 145 milliwatts, making a total power drain for one scale-of-two about 220 milliwatts. A scale of 16

that uses these units therefore consumes approximately 0.880 watt. The power consumption of the low current scales of 16, used as channel scalers in the present multichannel analyzers, is approximately 16.5 watts.

The component parts of the subminiature scale-of-two are inserted in a Lucite base plate which serves as a construction jig as well as a mounting plate for the finished unit. A Lucite box of outer dimensions $\frac{5}{8} \times 1\frac{3}{4} \times 1\frac{3}{8}$ in. slips over the wired scale. Mounting ears on the box hold the unit to its mounting, which is a chassis plate with a $1\frac{3}{8}$-in. slot to accept the box. Power connections are made by means of short leads which attach to small tinned-copper buses running the length of the assembled unit. Cascading connections are made directly from unit to unit. Since the width of the unit is only $\frac{5}{8}$ in., a scale of 4096 requires but $7\frac{1}{2}$ in. of mounting space. Figure 7.14 shows the layout of these units.

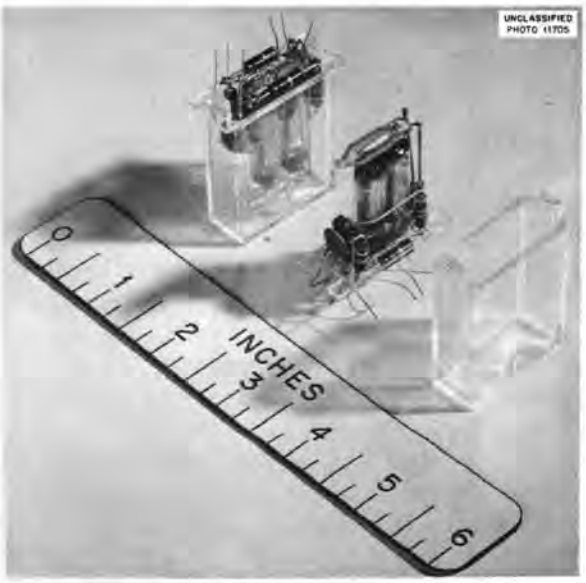


**Fig. 7.14. Subminiature Scale of Two.**

It is hoped that this unit, with its low power drain, low cost, and small size, will prove sufficiently reliable to allow its use in multichannel pulse-height analyzer applications, as well as in general scaler use.

### Automatic Preset-Count Scale of 4096

An automatic preset-count scale of 4096 has been built to demonstrate the advantages of the subminiature scale-of-two and to provide a means of obtaining some measure of reliability of these units.

The circuit (see Fig. 7.15) is composed of a pulse-height discriminator, 12 scaling stages, a start-stop gate scale, and a precision electronic clock with mechanical register indication. The discriminator will deliver suitable output with pulses of 1 volt in amplitude and 0.3 $\mu$sec in length. It utilizes two of the three miniature tubes in the circuit. Twelve scales-of-two provide a scale of 4096, and scaling factors from 32 to 4096 may be selected. In addition, continuous scaling is allowed upon selection. A thirteenth scale provides a "count" pilot light and serves as the start-stop relay. The electronic clock is comprised of a precision, free-running multivibrator, an amplifier, a register driver tube, and a Veeder-Root register which has been modified for quiet operation. The clock circuit is in operation whenever the instrument is turned on; however, until desired, no indication other than a flashing neon light in the clock box is given. Selection of one of the two rates provided (0.10 sec of 1.0 sec) is accomplished by means of a switch. Adjustment is provided for both rates.

The operation of the instrument is as follows. After the "start" button is depressed, the first clock signal to occur triggers the gate scale which allows pulses from the discriminator to enter the scalers and which starts the removal of a disabling lock on the clock indicator circuit. The next clock signal is recorded. (This prevents recording a clock signal for the "zeroth" time interval.) Scaling now takes place and the clock register is recording time.

When the desired count has been reached, a signal from the selected scale triggers the gate scale, closing the gate between discriminator and scalers, and disables the clock indicator circuit. The elapsed time is read on the clock register. Manual stopping is provided for by a simple reset on the gate scale.

The circuit operates as designed with an apparent stopping time of 50 $\mu$sec. Resolving time for random pulses is about 5 $\mu$sec. The clock circuit performs very stably and accurately, and the error of the clock is less than 0.2%.

The unit is housed, with its power supply, in a cabinet $6\frac{1}{2} \times 7 \times 11$ inches. The weight is about $11\frac{1}{2}$ lb, and the total power consumption is approximately 12 watts. Figures 7.16 and 7.17 show the

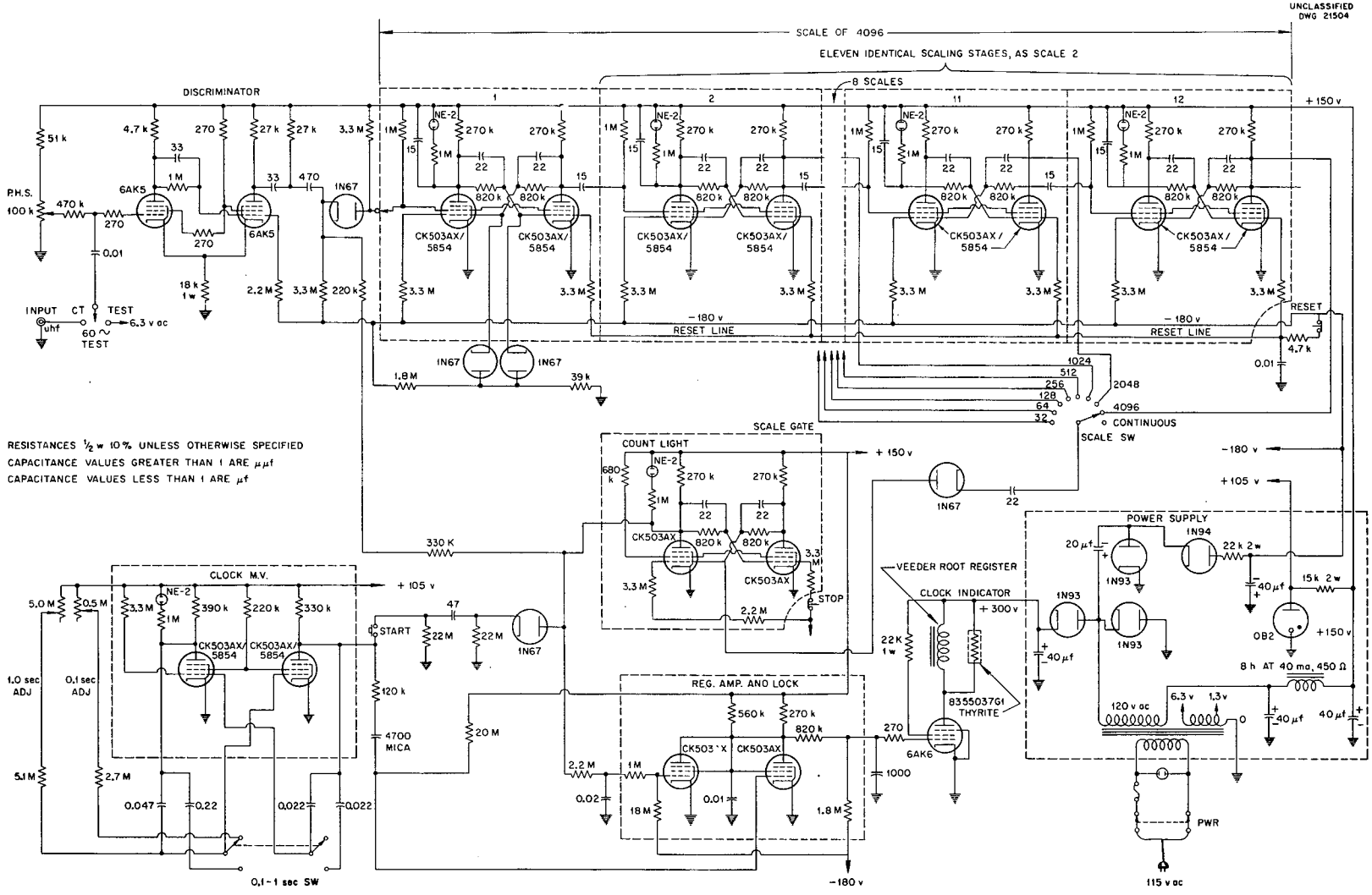


**Fig. 7.15. Automatic Scale of 4096.**

UNCLASSIFIED
PHOTO 11782

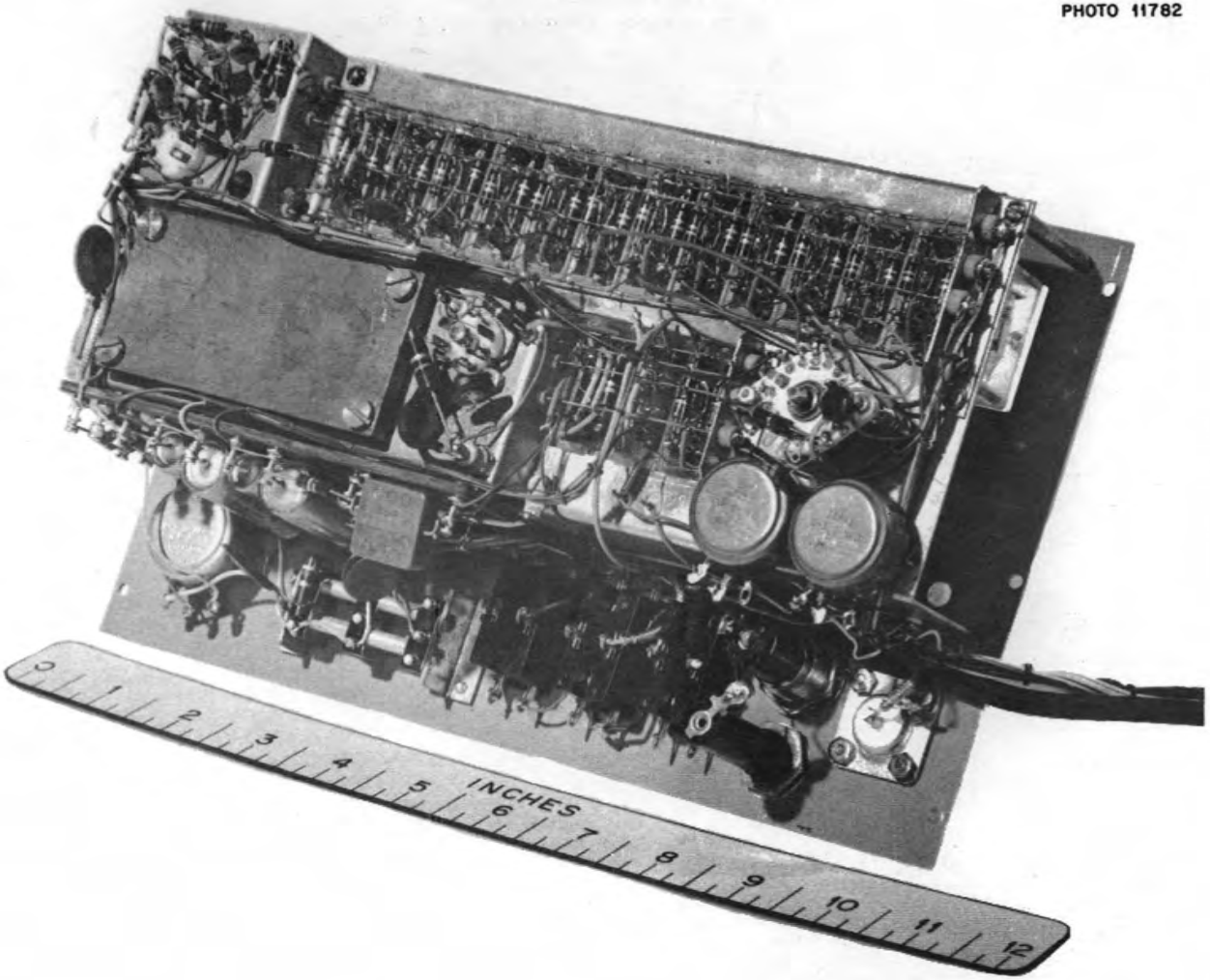


Fig. 7.16. Automatic Scale of 4096 (Back View).

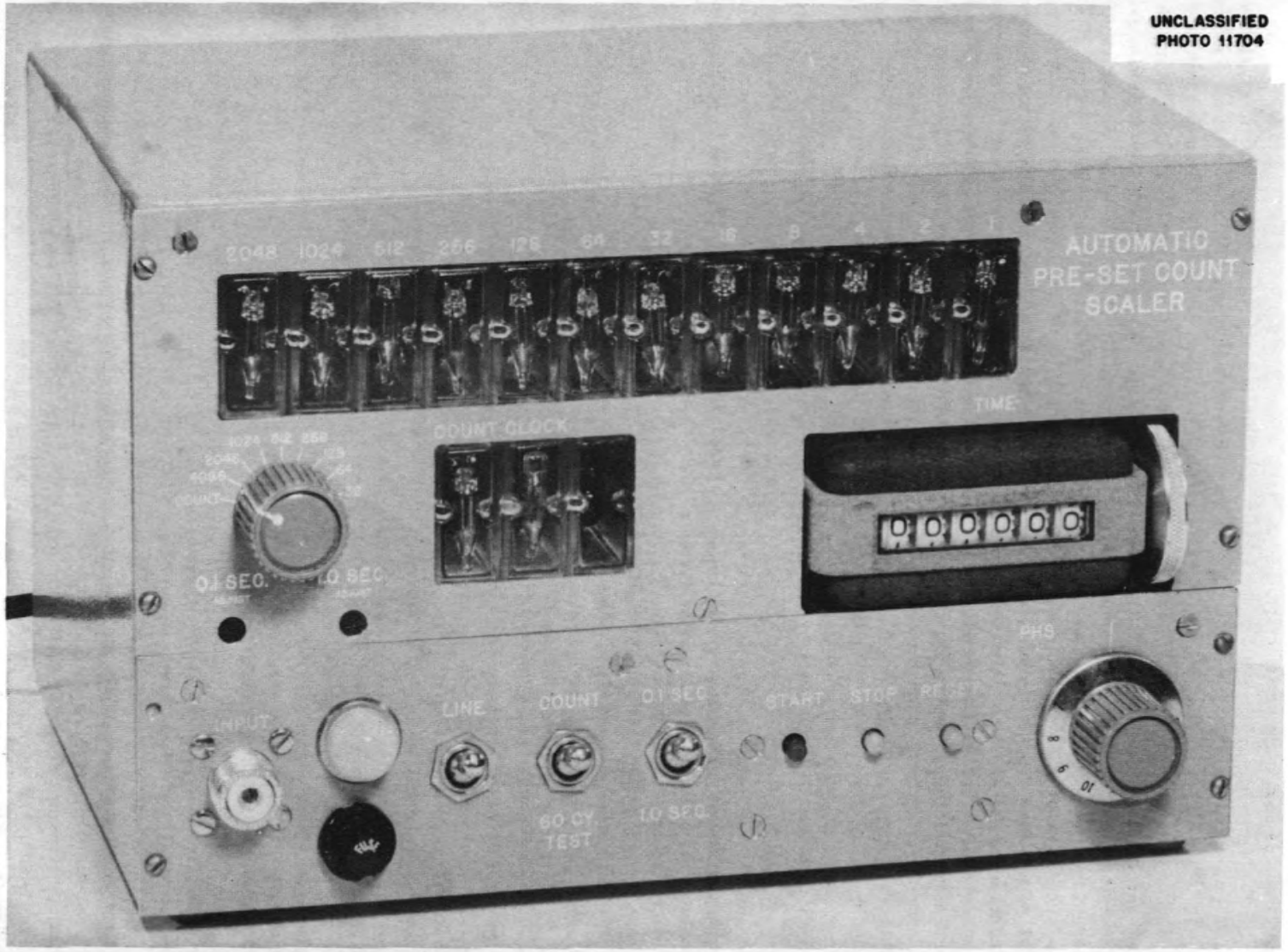


Fig. 7.17. Automatic Scale of 4096 (Front View).

physical layout of the unit. This instrument has been in continuous operation since its completion, and the operation has been quite satisfactory.

### NEUTRON PHOSPHORS

J. Schenck

Studies of the europium-activated lithium iodide phosphor, previously reported, are continuing. It has been found that the europium activator produces a broad optical absorption with a cut-off below about 4500 Å, the same type of absorption which has been observed in solutions containing the divalent europium ion. The wave length of the luminescent radiation of europium-activated lithium iodide is only slightly shorter than the absorption cut-off that is due to the europium ion; consequently, there is an appreciable amount of self-absorption of scintillations which depends upon the concentration of the europium activator.

The concentration of europium also has a strong effect upon the gamma-ray equivalent pulse height for thermal neutrons and probably for higher energy neutron-induced scintillations. Lithium iodide crystals containing 0.05, 0.035, and 0.01 mole % of europium give gamma-ray equivalent energies of 4.55, 3.90, and 2.97 Mev, respectively, for thermal neutrons. In other words, the scintillator becomes increasingly inefficient for the alpha and triton particles relative to gamma rays as the europium concentration is lowered. Since the luminescent efficiency of the europium-activated lithium iodide phosphor may be considered as an independent function of activator concentration, the optimum europium content will depend on the crystal size, the effect of gamma-ray response, and the scintillator application. Measurements are being made to obtain more quantitative data to serve as a basis for determining this optimum concentration.

Further work has been done with fast monoenergetic neutrons. Pulse-height spectra have been obtained for neutron energies from 2.5 to 4.4 Mev, crystal sizes from 15 × 7 to 39 × 25 mm, and europium concentrations from 0.01 to 0.05 mole %. The pulse-height spectra show a broad band containing definite structure instead of a single line corresponding to a fast neutron of a given energy. More experiments need to be made before these spectra can be completely analyzed.

### TOTAL-ABSORPTION SPECTROMETER

P. R. Bell R. C. Davis

A thallium-activated sodium iodide crystal with an effective diameter of 5 in. was obtained from Harshaw Chemical Company. By using this crystal with an RCA type H-5037 photomultiplier tube which has a $3\frac{1}{2}$-in.-dia photo surface (Fig. 7.18), a resolution of 10.4% full width at half counting rate was obtained for the 661-kev gamma line in $Cs^{137}$.

In the testing of various energy single gamma-ray emitters, it was found that there was a great reduction in Compton pulses, especially the higher energy ones, because the remaining energy of the initial photon was too small to allow it to escape from the crystal. Consequently there was an increase in pulses in the full energy peak (Figs. 7.19 and 7.20).

Since this detector has $4\pi$ geometry, it is possible to use it for self-coincidence measurements. Copper-64, with a positron to the ground state and weak electron capture followed by a 1.35-Mev gamma ray, shows in its spectrum (Fig. 7.21) a

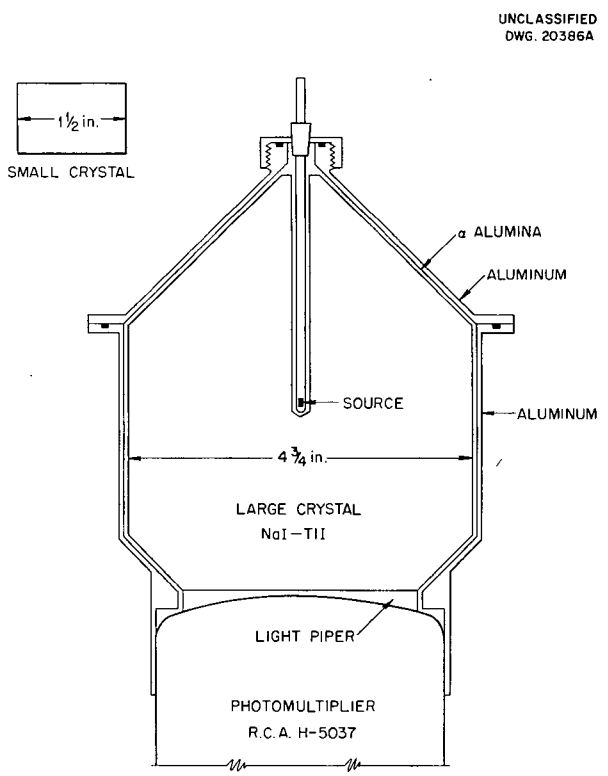


**Fig. 7.18. Arrangement of Source and Detector.**

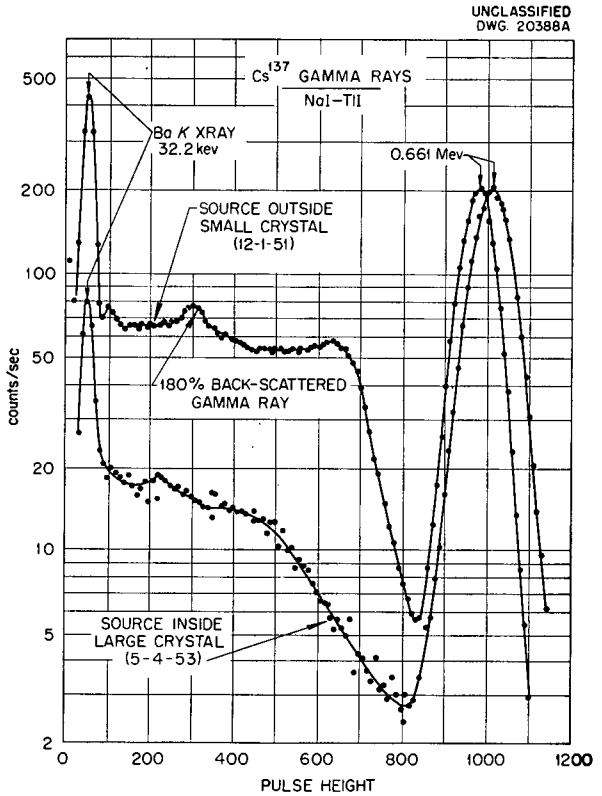


**Fig. 7.19. $Cs^{137}$ Spectrum with Total-Absorption Spectrometer.**

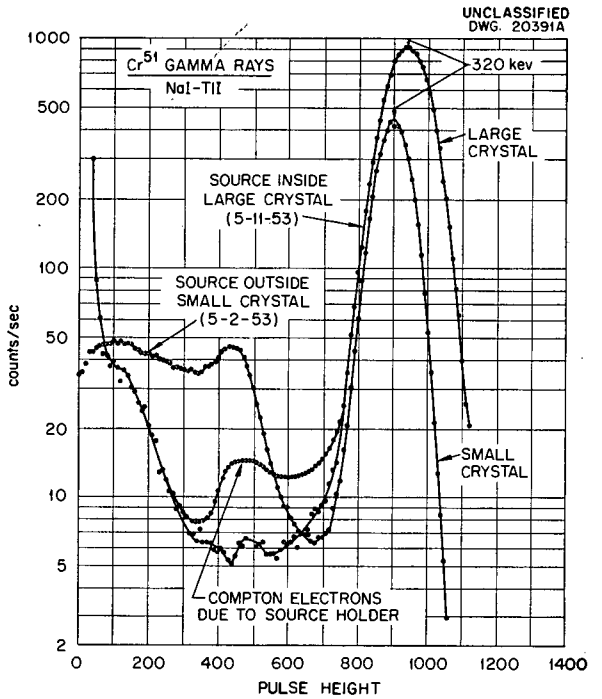


**Fig. 7.20. $Cr^{51}$ Spectrum with Total-Absorption Spectrometer.**

peak at 0.511 Mev where one annihilation quantum is absorbed completely and one escapes the crystal, a second peak at 1.022 Mev where both annihilation quanta are absorbed completely, and a third peak at 1 35 Mev which is the full energy peak for the gamma ray. Sodium-24, which has two gamma rays in cascade, shows in its spectrum (Fig. 7.22) the two gamma rays plus the sum peak. Sodium-22, which has a positron followed by a 1.277-Mev gamma ray plus a weak electron capture to the ground state, shows five peaks in its spectrum (Fig. 7.23). The first peak is at 511 kev, the second at 1.022 Mev, and the third at 1.277 Mev for the full energy peak. Since the positron, hence the annihilation radiation, is in coincidence with the gamma ray, there are peaks at 1.277 plus 0.511, or 1.79 Mev, and at 1.277 plus 1.022, or 2.30 Mev.

The decay scheme for $Mg^{28}$ (Fig. 7.24) was determined by using both a $1\frac{1}{2} \times 1$ in. sodium iodide crystal and an RCA type 5819 tube and the 5-in. sodium iodide crystal on an RCA type H-5037 tube. Figure 7.25 shows the spectrum on both

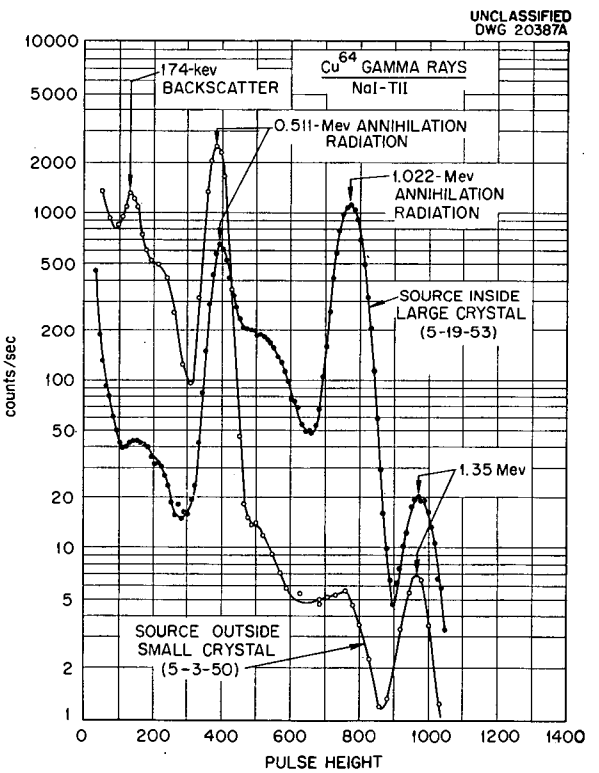


**Fig. 7.21. $Cu^{64}$ Spectrum with Total-Absorption Spectrometer.**

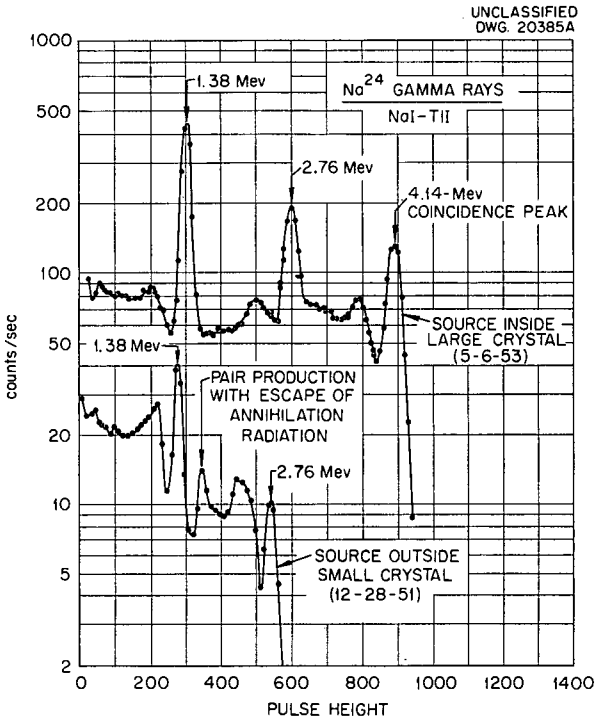


**Fig. 7.22. $Na^{24}$ Spectrum with Total-Absorption Spectrometer.**

large and small crystals. In this curve, by using the large crystal, the 400-kev gamma and the 1.35-Mev gamma are shifted to 430 kev and 1.38 Mev, since they are in coincidence with the 30-kev gamma. The 400- and 958-kev gammas are equally intense, but the chance of the 958-kev gamma being detected while the 400-kev ray completely escapes the crystal is very small. Also, the 958-kev peak is smeared slightly by the Comptons of the two higher energy radiations. For these reasons, the 958-kev peak is not very prominent and it is hard to determine its exact energy; however, it is assumed that the 958-kev peak is increased by 30 kev, as are the other two.

Figure 7.26 shows the $Mg^{28}$ spectrum with the source inside the large crystal. In one case an aluminum absorber is used for betas, and in the other case a brass absorber sufficiently thick to stop the 30-kev gamma is employed. There is a definite shift of 30 kev in the 400-kev and 1.35-Mev gammas. When these curves were run, the sample had decayed enough to show a manganese impurity, hence the 800-kev line.

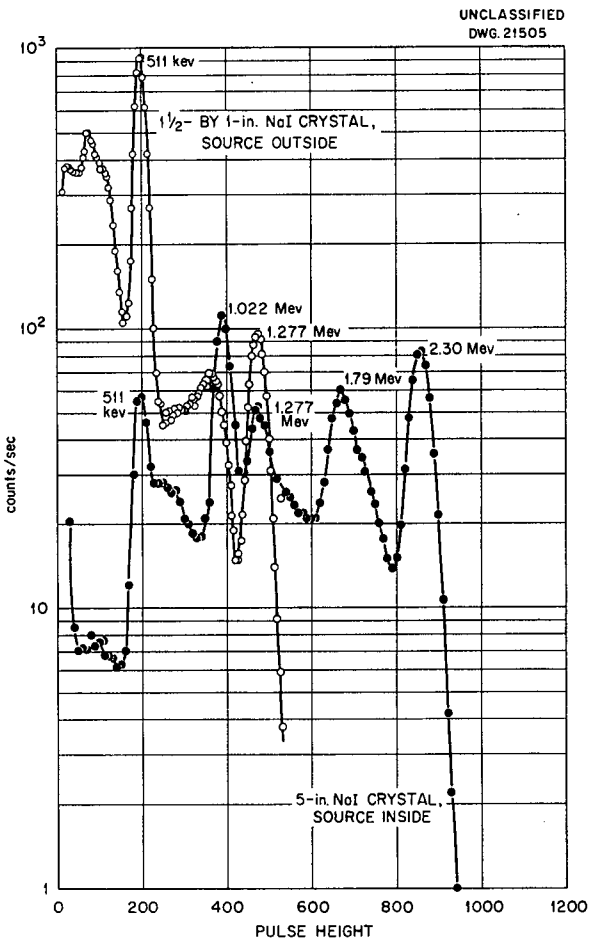


**Fig. 7.23. $Na^{22}$ Spectrum with Total-Absorption Spectrometer.**

## OPERATION OF PROTON RECOIL TELESCOPE

C. C. Trail C. H. Johnson

A neutron telescope consisting of a polyethylene radiator, a proportional counter, and a scintillation counter is shown in Fig. 7.27. Radiators of variable thickness were mounted upon a wheel which permitted the radiator thickness to be varied without having to open the telescope. Proton recoils were analyzed by gating a multichannel analyzer with the coincidence pulse from the proportional counter and scintillation counter. The analyzer measured the distribution of the proton-recoil scintillation pulses.

A 3-mm thallium-activated sodium iodide crystal and a 6292 photomultiplier formed the scintillation counter. The proportional counter had a 15-mil

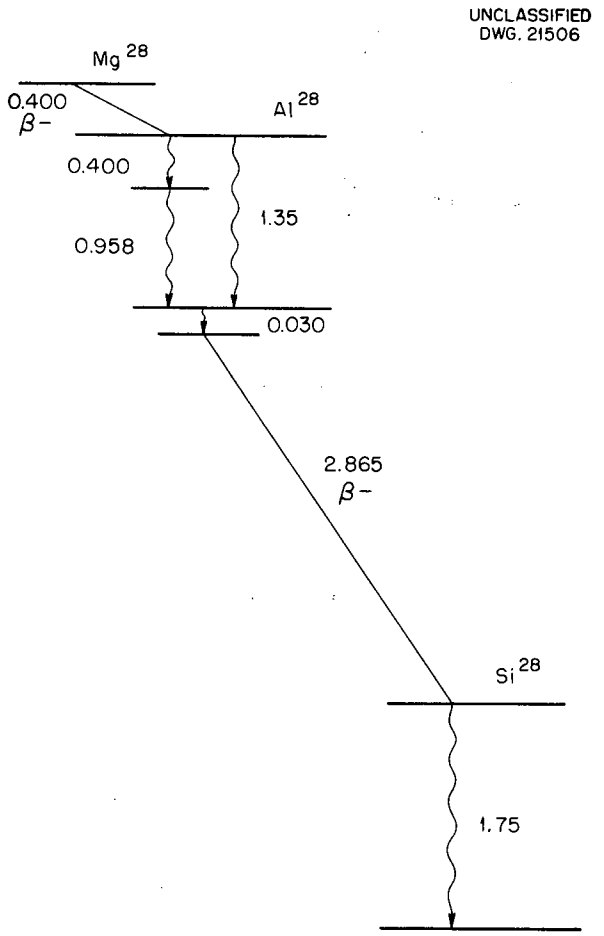


Fig. 7.24. Decay Scheme of $Mg^{28}$.

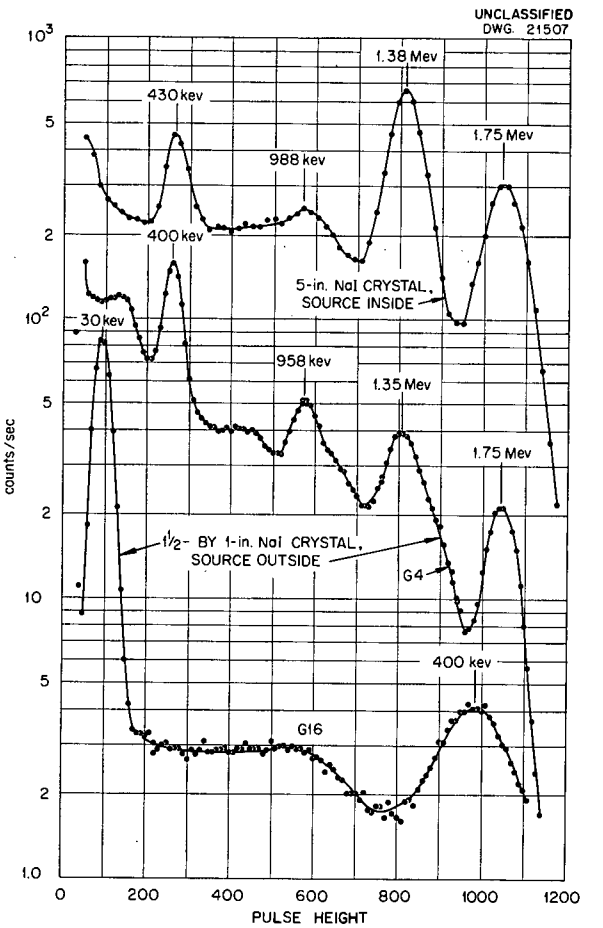


Fig. 7.25. $Mg^{28}$ Spectra Used to Determine Decay Scheme.

wire and was filled to a pressure of 6 in. of argon (3% $CO_2$) gas.

Figure 7.28 is a neutron spectrum at 0 deg of the $D(d,n)He^3$ reaction obtained on the 2.5-Mev Van de Graaff with a bombarding energy of 1.8 Mev. As counting rates were small, good resolution was sacrificed by using a thick radiator and by permitting the radiator to subtend a half-angle of 15 deg to the neutron source. (The radiator and geometry contributed a spread of 14% to the recoil proton spectrum.) Poor statistics with a thin radiator subtending a half-angle of 5 deg indicated a resolution of 7%. The neutrons were monitored with a current integrator.

Since the geometry of the telescope and the radiator thicknesses are known, absolute neutron fluxes may be determined.

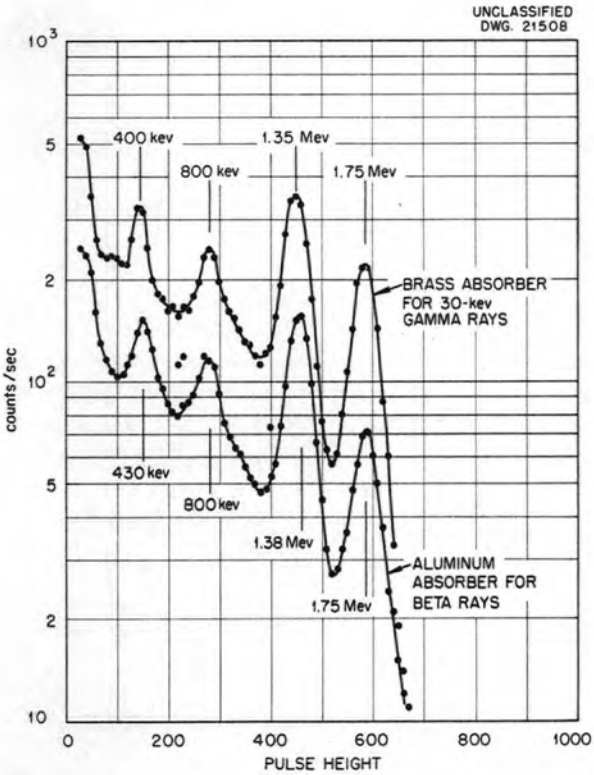


**Fig. 7.26. $Mg^{28}$ Spectra with Absorbers.**

**Fig. 7.27. Proton Recoil Telescope.**

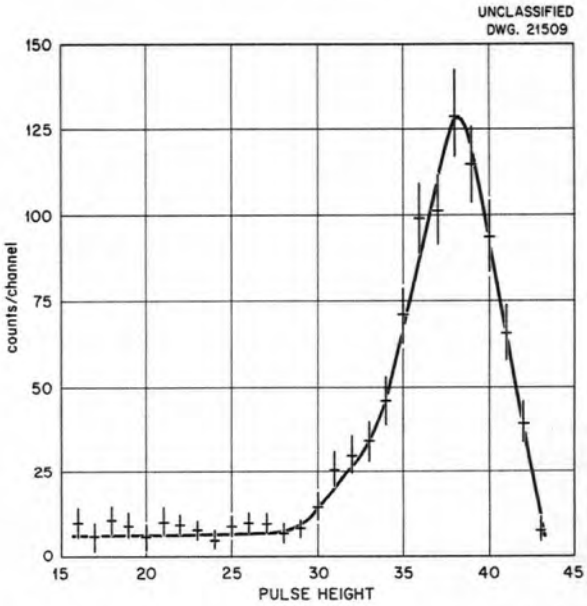


**Fig. 7.28. Neutron Spectrum at 0 deg of $D(d,n)He^3$ Reaction.**

# 8. PHYSICS OF REACTORS

## VISIBLE LIGHT FROM NUCLEAR RADIATION

F. C. Maienschein R. G. Cochran
T. Love

Recently, a preliminary experiment was performed at the Bulk Shielding Facility in an attempt to determine the conditions under which visible light can be seen in air close to a reactor shield. The experimental setup consisted of a 12-in.-dia iron pipe (sealed off at the bottom) that was submerged vertically in the pool to a depth of approximately 20 feet. The BSF reactor was then positioned so that there was approximately 40 cm of water between the pipe and the north face of the reactor. A camera containing color film was attached to the top of the pipe and a 1/2-hr exposure was made with the reactor operating at 50 kw. Upon development, the film showed that a faint spot of light was present in the pipe. This spot was not due to gamma radiation streaming up the pipe because the lens would not focus other than visible light, and, furthermore, a background film which was treated identically, except that it was not exposed to the light, did not show a spot. It is planned to extend this investigation in order to obtain quantitative results.

## MEASUREMENT OF THE ENERGY RELEASED PER FISSION

J. L. Meem L. B. Holland
G. M. McCammon

For the power calibration of the Bulk Shielding Reactor by means of neutron-flux measurements,[1,2] gold foils were exposed in various positions throughout the reactor, thus providing the necessary data to map the thermal flux. The fission rate was then calculated from the uranium fission cross section and the known amount of uranium throughout the reactor. One of the largest uncertainties in this method is the value chosen for the energy released per fission. As was reported in the last quarterly report,[3] an experiment designed for the measurement of this quantity has been performed. The results have since been analyzed and have been reported in detail in a separate report.[4] A summary is given as follows.

The energy released per fission, $E_t$, is given by

$$E_t = E_K + E_\beta + E_\gamma + E_n + E_\gamma^* ,$$

where $E_K$ is the kinetic energy of the fission fragments, $E_\beta + E_\gamma$ is their decay energy (not including neutrino energy), $E_n$ is the kinetic energy of the fission neutrons, and $E_\gamma^*$ is the prompt gamma-ray energy. In the past, the most reliable value for $E_t$ has been obtained by adding the experimentally determined values of the various components.

The energy released per fission in a reactor also includes an additional component, $E_c$, which is the energy liberated in capture processes that do not lead to fission, namely, nonproductive capture in $U^{235}$, capture in moderator, capture in reactor structure, etc.

Accordingly, a measurement in a reactor gives $E_t'$, where

$$E_t' = E_t + E_c .$$

Since the parasitic capture term, $E_c$, can be calculated easily in a thermal reactor, a measurement of $E_t'$ would give the value of $E_t$, the energy released per fission.

For the experiment, the BSF reactor[5] was loaded as shown in Fig. 8.1. A special fuel element was constructed and placed in position 37. In that position the net flow of heat and radiation into and out of the special element was found to be minimized.

The special element, which is shown in Fig. 8.2, had a removable center fuel plate from which 1¼-in.-dia disks were punched to facilitate measurement of their activation by exposure in the reactor. A similar uranium-bearing disk was activated by exposure in a known neutron flux. By comparison, the actual fission rate in the special fuel element could thus be determined.

The special element was equipped with water tubes at top and bottom through which water was pumped at a known rate. Thermocouples were used

[1] J. L. Meem and E. B. Johnson, ORNL-1027 (Aug. 13, 1951) (classified).

[2] E. B. Johnson and J. L. Meem, ORNL-1438 (April 21, 1953) (classified).

[3] J. L. Meem *et al.*, *Phys. Quar. Prog. Rep. Dec. 20, 1952*, ORNL-1477, p. 1.

[4] J. L. Meem, L. B. Holland, and G. M. McCammon, ORNL-1537 (Oct. 7, 1953) (classified).

[5] W. M. Breazeale, ORNL-991 (May 8, 1951) (classified).

DECLASSIFIED
DWG. 17499

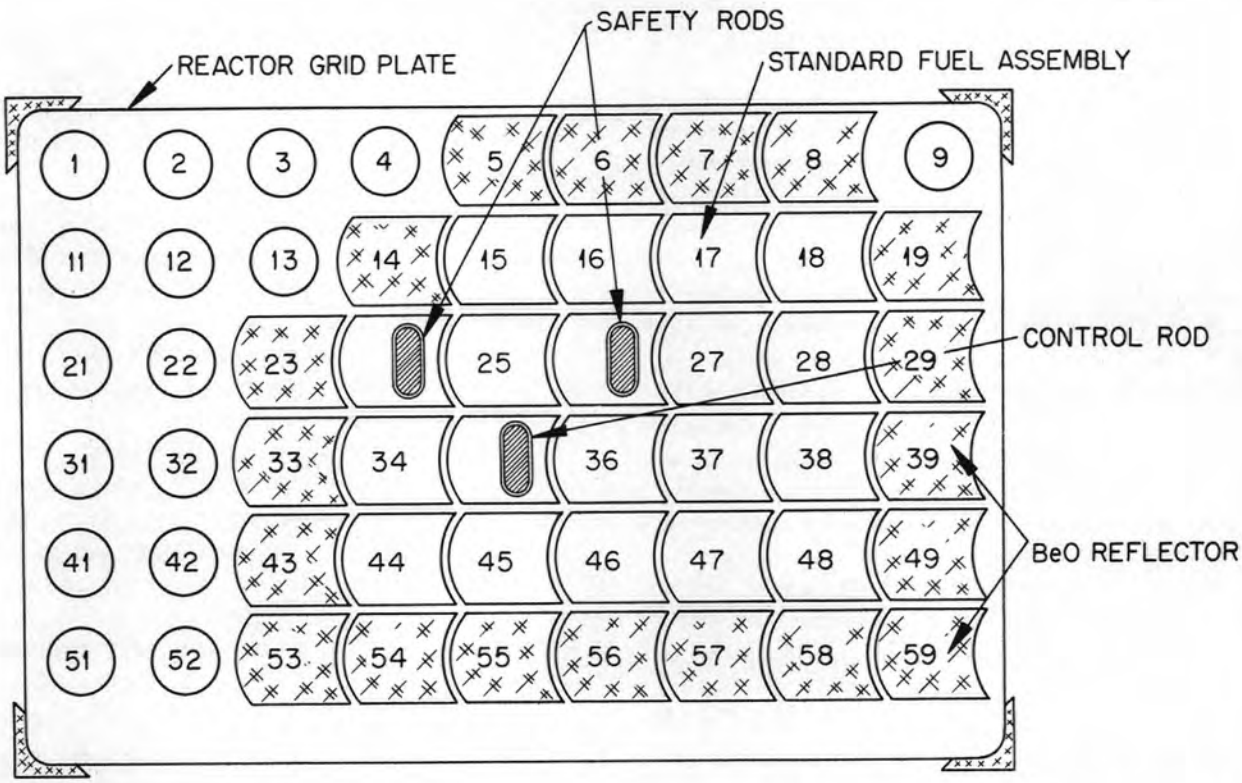


**Fig. 8.1. Reactor Loading for Measurement of Energy per Fission; Special Fuel Element in Position 37.**

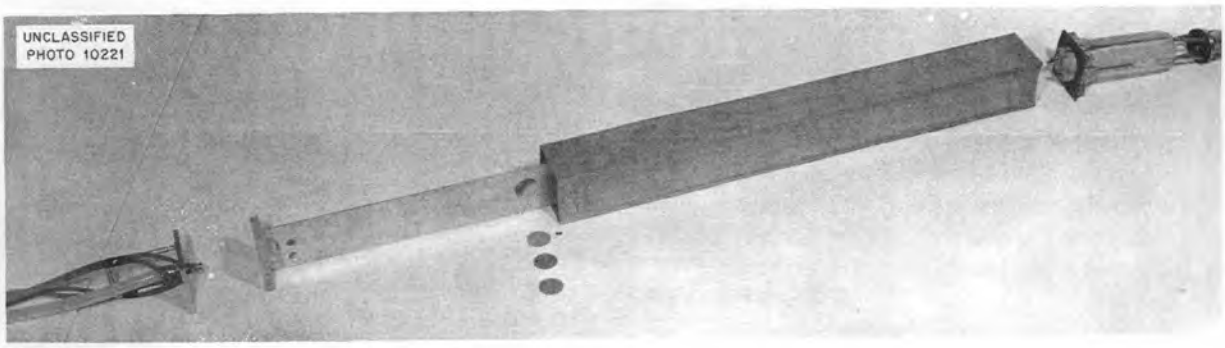


**Fig. 8.2. Special Fuel Element.**

to measure the temperature rise across the fuel element, special precautions being taken to prevent heat leakage. The power, or rate of energy production, was determined from the water flow and temperature rise, and a comparison with the fission rate gave the heat released per fission in the special fuel element. The net amount of radiation leaking out of the fuel element (less than 0.2%) was calculated as a correction to this figure.

The energy per fission in the reactor, $E_t'$, was 193 ± 5 Mev. The parasitic capture, $E_c'$, in the Bulk Shielding Reactor is calculated to be 2.7 Mev. Accordingly, the energy released per fission (exclusive of neutrino energy) is 190 ± 5 Mev. This result is based on a gold cross section of 95 barns and a fission cross section of 549 barns for 2200-meter-per-second neutrons. If these values are revised, the effect can be calculated from:

$$E = 190 \times \frac{\sigma_{Au}}{95} \times \frac{549}{\sigma_f}.$$

# 9. THEORETICAL PHYSICS

## PSEUDOSCALAR INTERACTION IN BETA DECAY

M. E. Rose R. K. Osborn

The theory of forbidden beta transitions, as hitherto used, does not provide a correct treatment of the pseudoscalar interaction. This is demonstrated by the application of a canonical transformation to the Hamiltonian of interacting nucleons and leptons whereby all odd nuclear Dirac operators are eliminated from the theory. When this transformation is properly applied, it is seen that the pseudoscalar interaction makes a contribution to the beta-decay process only because the lepton covariants are not constant. Examination of the corresponding additional operators introduced in the other three interactions ($S$ is pure even) shows that, except in one case, these make trivial corrections which would not be observed in practice. The exception occurs in second and higher forbidden transitions wherein the spin change (tensor rank, strictly speaking) is lower than the forbiddenness order. Because of present knowledge of the beta interaction, these must be regarded as small correction terms. It is possible that all nuclear matrix elements have been calculated, using nonrelativistic wave functions based on the J-J coupling model. The results also show that in some cases (very probably $RaE$) it will be possible to obtain the ratio of coupling coefficients ($g_P/g_T$, for example) by comparison with the observed spectral shapes. A method of reduction of the beta-decay operators has been developed and the same procedure is very convenient for obtaining the nuclear matrix elements. In this method, the irreducible tensors are obtained automatically, and the retardation expansion is a trivial operation performed at the end of the calculation rather than at the beginning. The correction factors for pseudoscalar ($P$) as well as $P$-$T$ and $P$-$A$ mixtures are obtained, and it is observed that the shape of the correction factor is strongly modified as compared with the customary result. The correction factor is now more strongly $Z$-dependent and this would perhaps account for the appearance of the $P$ interaction only for heavy elements. Also, if the $P$ interaction can effectively mix with others, an abnormally large $ft$ value must be expected for first forbidden (and higher) transitions. It must also be expected that $g_P \gg g_T$ or $g_A$.

This work opens up the possibility of an extensive investigation into many aspects of beta decay which have not been adequately understood up to now. At present the problem of nuclear-matrix elements is being investigated, and the problem of $l$-forbiddenness can now be approached in a much more rational way than was hitherto possible.

## MAGNETIC SCATTERING OF NEUTRONS

G. T. Trammell

In order to study the magnetic properties of the rare earths by neutron-diffraction techniques, it is necessary to obtain expressions which give the neutron-scattering cross section of atoms whose orbital moments are not quenched. In a paper submitted for publication in the *Physical Review*, it is shown that the Born approximation for the

scattered neutron wave may be written,

$$\Psi_{\text{scatt.}} \sim \frac{Meg_N}{mch^2} \sum_f \left\{ \chi_f \psi_f | \mathbf{S}_N \cdot [\mathbf{P} - \mathbf{e}(\mathbf{P}\cdot\mathbf{e})] | \chi_0 \psi_0 \right\} \chi_f \psi_f \frac{e^{i\mathbf{p}_f \mathbf{r}_N}}{r_N} ,$$

which is identical with the expression given by Halpern and Johnson,[1] Eq. 4.1, except that with the inclusion of orbital current effect, **P** becomes

$$\mathbf{P} = \sum_i \tfrac{1}{2}[\mathbf{L}_i f(\mathbf{k}\cdot\mathbf{r}_i) + f(\mathbf{k}\cdot\mathbf{r}_i)\mathbf{L}_i] + 2\mathbf{S}_i e^{i\mathbf{k}\cdot\mathbf{r}_i} ,$$

with

$$f(x) = \frac{2}{x^2} \int_0^x y e^y dy .$$

Here $\chi$ is the neutron spin function; $\psi$ is the atomic wave function; $\hbar\mathbf{p}$ is the neutron momentum; $\mathbf{k} = \mathbf{p}_f - \mathbf{p}_0$; **L** is the orbital angular momentum operator; **S** is the spin angular momentum operator; subscripts $f$ and 0 refer to after and before the collision, respectively; subscript $N$ refers to the neutron; and subscript $i$ refers to the $i$th electron in the atom.

The technique of evaluating $(\psi_f|\mathbf{P}|\psi_0)$ for the Russell-Saunders coupling scheme is illustrated by the detailed calculation of these matrix elements for $Er^{+++}$ and $Nd^{+++}$, which are assumed to be in the configurations $^4I_{15/2}$ and $^4I_{9/2}$, respectively.

Finally, a comparison of the theoretical differential scattering cross section, derived with the assumption of hydrogen-like radial wave functions, with the observed scattering from $Er_2O_3$ and $Nd_2O_3$ gives satisfactory agreement if $Z - S$, "the effective nuclear charge," is taken to be 23 and 20 for $Er^{+++}$ and $Nd^{+++}$, respectively.

## THEORY OF POLARIZED PARTICLES AND GAMMA RAYS IN NUCLEAR REACTIONS

A. Simon T. A. Welton

Previous calculations[2] of the polarization resulting from a nuclear reaction initiated by unpolarized particles have been generalized.[3] If an arbitrarily polarized initial beam is characterized by its initial spin tensor moments $T_K^{(q)}$, an expression can be written for the expectation value in the final state of any spin tensor $T_{K'}^{(q')}$ resulting from any initial tensor $T_K^{(q)}$. All sums over magnetic quantum numbers are performed by the use of the $S$-matrix and Racah formalisms. The results are expressed in terms of the $G$-function, which is related to the Fano $X$-function.

The $S$-matrix formalism was also extended to include the possibility of gamma rays in nuclear reactions. Analogous formulas to those of Blatt and Biedenharn are given in reference 3.

## TABULATION OF ANGULAR MOMENTUM FUNCTIONS

A. Simon

Previous tables of the Racah functions,[4] $w(abcd:ef)$, have not included functions of four, odd, half-integral arguments. These tables are now being extended and revised. The computations will be done on the UNIVAC and will be presented in decimal form.

Computation of the $X$-function[3] is also being considered. This would be a relatively simple problem to code, since the Racah function calculation could be used as a subroutine. Tabulation of the $G$-function[3] would require, in addition, numerical values of the Clebsch-Gordan coefficients. There may be some intrinsic value in preparing such a table as well.

## RELATIONS BETWEEN THE GENERALIZED HYPERGEOMETRIC SERIES AND THE ANGULAR MOMENTUM FUNCTIONS OF PHYSICS

A. Simon

The well-known Racah functions, $w(abcd:ef)$, which appear in almost all problems involving angular momenta can be shown to be a particular

[1] O. Halpern and M. H. Johnson, *Phys. Rev.* 55, 898 (1939).

[2] A. Simon and T. A. Welton, *Phys. Rev.* 90, 1036 (1953).

[3] A. Simon, "Theory of Polarized Particles and Gamma-Rays in Nuclear Reactions," *Phys. Rev.* (in press).

[4] L. C. Biedenharn, *Tables of the Racah Coefficients*, ORNL-1098 (April 8, 1952).

value of a *Saalschutzian* hypergeometric series

$$\dot{w}(abcd{:}ef) \sim {}_4F_3\left[\begin{matrix} e-a-b,\ e-c-d,\ f-a-c,\ f-b-d\ ; \\ -a-b-c-d-1,\ e+f-a-d+1,\ e+f-b-c+1 \end{matrix}\right] .$$

Similarly, the Clebsch-Gordan coefficients may be written in terms of the series ${}_3F_2$. More complex angular functions, such as the $X$-function and the $G$-function,[2,3] are related to higher hypergeometric series.

The theory of hypergeometric series of the type ${}_pF_q$, where $p = q + 1$, has been highly developed in the mathematical literature. In particular, all independent recurrence relations have been written. By expressing these relations in the Racah form, it may be possible to obtain some useful recurrence relations. Similar possibilities exist for the Clebsch-Gordan coefficient, $X$- and $G$-function, etc. Other products of this identification are expressions for the angular momentum functions in the form of contour integrals, as well as a derivation of the differential equations giving rise to them.

This investigation was done in collaboration with R. R. Coveyou, W. Sangren, and R. A. Charpie.

## SCATTERING MATRIX FORMALISM FOR NUCLEAR REACTIONS INVOLVING GAMMA RAYS

T. A. Welton

The standard scattering matrix formalism for the description of nuclear reactions involving only particles has apparently never been given a rigorous extension to the case of reactions in which a gamma ray enters and/or leaves. The formal basis for such interesting fields as the angular correlation of gamma rays is thereby rendered uncertain. The difficulty is that for the particle case the usual definition and properties of the $S$-matrix embody those properties of the asymptotic wave-function of the system which are independent of the details of the nuclear forces (probability conservation, invariance under time reversal, angular momentum, and parity conservation). Classically, analogous properties can be proved for an $S$-matrix defined from the asymptotic vector potential (at least in those simple cases where the radiation is scattered without absorption or change in frequency). Here, probability conservation is replaced by energy conservation. It has been customary to attempt to define a quantum mechanical $S$-matrix for radiation by thinking of the vector potential (actually a quantum mechanical *operator* in the Hamiltonian) as a sort of "wave function" for the photon. This hybrid point of view presumably does not falsify the major results (angular distribution) of the theory, but it may lead to error on more subtle points (magnitudes of cross sections).

A consistent viewpoint has been achieved by recasting the general nuclear reaction problem in momentum space and by making use of the properties of the $S$-matrix previously defined in quantum electrodynamics. Define the $S$-matrix element for the particle in – particle out case:

$$(1) \qquad (\Omega', a', I', \mathcal{I}', i', \dot{\imath}'|S|\Omega, a, I, \mathcal{I}, i, \dot{\imath}) ,$$

where $\Omega'$, $a'$, $I'$, $\mathcal{I}'$, $i'$, and $\dot{\imath}'$ are initial direction, channel, target spin and $z$-component thereof, and projectile spin and $z$-component thereof (unprimed quantities refer to the final state). The above matrix is reciprocal (implies reciprocity) and unitary when a complete summation and integration is performed over the matrix indices. The matrix is further invariant under space rotations, which is sufficient to limit its angular dependence as much as possible from general considerations only. The cross section for the above transition is given by

$$(2) \qquad \frac{d\sigma}{d\Omega} = \frac{4\pi^2}{k^2}|S - 1|^2 ,$$

where $k$ is the incident wave-number and $S$ is an abbreviation for Eq. 1. As an illustration of the new formalism, consider a reaction with gamma rays in *and* out. The corresponding $S$-matrix element is written as

$$(3) \qquad (\Omega', a', I', \mathcal{I}', p'|S|\Omega, a, I, \mathcal{I}, p) .$$

The indices $p'$ and $p$ now cover the range 1, 2, 3, and give $S$ essentially a vector character. The matrix is transverse in that it vanishes if $p$ refers to the direction $\Omega$ or if $p'$ refers to $\Omega'$. Reciprocity and unitarity again hold, and rotational invariance

yields all possible angular dependences, which emerge in terms of the usual multipole vector potentials, although Eq. 2 refers not to the true vector potential but to a probability amplitude, as in Eq. 1.

Further results have been deduced by consideration of possible energy dependences of Eq. 3. In particular, a valid theorem on the interference of mixed multipoles has been given. This replaces Lloyd's theorem but gives the same results in practice.

### CALCULATION OF LEVEL SHIFT IN HYDROGEN

T. A. Welton

The calculation of the level shift in hydrogen described in the last quarterly report is essentially complete. The general procedure is very similar to two computations already given in the literature, but special attention is being given to improving the treatment of two items. One item is the effect of binding on the sum over intermediate states which constitutes the so-called "second-order level shift." The other item is the alteration of the main term (position fluctuation) of the level shift because of the singularity at the nucleus of the $S$ wave functions. No quantitative conclusion is yet possible.